SYNCHROTRON RADIATION BASED VUV SPECTROSCOPY OF SOME POLYATOMIC MOLECULES OF ENVIRONMENTAL INTEREST

By

Param Jeet Singh

Enrolment No. PHYS01201004011

Bhabha Atomic Research Centre
Trombay, Mumbai - 400085, India

A thesis submitted to the

Board of Studies in Physical Sciences

In partial fulfillment of requirements

for the Degree of

DOCTOR OF PHILOSOPHY IN PHYSICS

of

HOMI BHABHA NATIONAL INSTITUTE

May, 2014

Homi Bhabha National Institute

Recommendations of the Viva Voce Committee

As members of the Viva Voce committee, we certify that we have read the dissertation prepared by Mr. Param Jeet Singh entitled “Synchrotron Radiation Based VUV Spectroscopy of Some Polyatomic Molecules of Environmental Interest” and recommend that it may be accepted as fulfilling the thesis requirement for award of Degree of Doctor of Philosophy.

Sandip Kumar Deb 5-12-2014.
Chairman - Prof. S.K. Deb **Date:**

Guide / Convener – Prof. B.N. Jagatap **Date:** 05/12/2014

05/12/2014
Member – Prof. A.P. Mishra **Date:**

Member – Prof. K. Sundararajan **Date:** 5/12/2014

Final approval and acceptance of this thesis is contingent upon the candidate’s submission of the final copies of the thesis to HBNI.

I hereby certify that I have read this thesis prepared under my direction and recommend that it may be accepted as fulfilling the thesis requirement.

Date: December 05, 2014

Place: Mumbai

Prof. B. N. Jagatap

STATEMENT BY AUTHOR

This dissertation is submitted in partial fulfillment of requirements for an advanced degree at Homi Bhabha National Institute (HBNI) and is deposited in the Library to be made available to borrowers under rules of the HBNI.

Brief quotations from this dissertation are allowable without special permission, provided that accurate acknowledgement of source is made. Requests for permission for extended quotation from or reproduction of this manuscript in whole or in part may be granted by the Competent Authority of HBNI when in his or her judgment the proposed use of the material is in the interests of scholarship. In all other instances, however, permission must be obtained from the author.

05/12/2014

Param Jeet Singh

DECLARATION

I, hereby declare that the investigation presented in the thesis has been carried out by me. The work is original and has not been submitted earlier as a whole or in part for a degree / diploma at this or any other Institution / University.

05/12/2014

Param Jeet Singh

List of publications arising from the thesis

Journal

1. "First commissioning results from high resolution vacuum ultraviolet beamline at indus-1 synchrotron source", Param Jeet Singh, Aparna Shastri, R. Sampath Kumar, S.N. Jha, S.V.N. B. Rao, R. D'Souza and B.N. Jagatap, Nuclear Instruments and Methods in Physics Research-A, **2011**, 634 113 – 119.
2. "VUV photoabsorption spectroscopy of Sulphur dioxide in the 1400 -1600 Å region: vibronic analysis of the $\tilde{E}-\tilde{X}$ system", Param Jeet Singh, Aparna Shastri, R. D'Souza, S.V.N. B. Rao and B.N. Jagatap, J. Quant. Spectrosc. Radiat. Transf., **2012**, 113, 267 – 278.
3. "The role of torsional modes in the electronic absorption spectrum of acetone", Aparna Shastri, Param Jeet Singh, B.N. Raja Sekhar, R. D'Souza and B.N. Jagatap, J. Quant. Spectrosc. Radiat. Transf., **2012**, 113, 1553 – 1565.
4. "Excited state vibrational modes of a few triatomic molecules of environmental interest", Aparna Shastri, Sunanda K., Param Jeet Singh, B.N. Raja Sekhar, S.V.N. Bhaskar Rao, R. D'Souza and B.N. Jagatap, Asian Journal of spectroscopy, **2012**, special issue, 107 – 119.
5. "Effect of isotopic substitution in the electronic absorption spectrum of acetone: VUV photoabsorption studies of acetone-d_6", Param Jeet Singh, Aparna Shastri, B.N. Raja Sekhar, R. D'Souza, B.N. Jagatap, J. Quant. Spectrosc. Radiat. Transf., **2012**, 114, 20 – 28.
6. "Rydberg states of chloroform studied by VUV photoabsorption spectroscopy", Param Jeet Singh, Aparna Shastri, R. D'Souza and B.N. Jagatap, J. Quant. Spectrosc. Radiat. Transf. **2013**, 129 204 – 213.
7. "Development of an experimental set-up for low temperature spectroscopic studies of matrix isolated molecules and molecular ices", Param Jeet Singh, B.N. Raja Sekhar, K. Sundararajan, Aparna Shastri, Vijay Kumar, Anuvab Mandal, A.K. Sagar, M.S. Ansari, P.K. Kush, B.N. Jagatap, Nuclear Instruments and Methods in Physics Research-A, communicated.
8. "VUV photoabsorption spectrum of acetone isolated in argon matrix", Param Jeet Singh, Aparna Shastri, B.N. Raja Sekhar, K. Sundararajan, Vijay Kumar, B. N. Jagatap, Chemical physics, Communicated.

Conference

1. "Preliminary results of VUV photoabsorption studies on the HRVUV beamline at Indus-1" Param Jeet Singh, S.N. Jha, R.D'Souza, D.V. Udupa, Aparna Shastri, Sampath Kumar, SVNB Rao, A. Sinha, S. Bhatt, Topical Conference on Interaction of EM Radiation with Atoms, Molecules & Clusters, RRCAT, Indore, **2010**.
2. "VUV Photoabsorption Studies of CHCl3 and CDCl3 Using photophysics Beamline at Indus-1" Aparna Shastri, Param Jeet Singh, B.N. Raja Sekhar and R. D'Souza, National symposium on radiation & Photochaemistry, JNV, Jodhpur, **2011**.
3. "VUV Absorption Spectrum of the E-X System of SO2" Param Jeet Singh, Aparna Shastri, S.V.N. Bhaskara Rao and R. D'Souza, DAE-BRNS Symposium on Atomic, Molecular and Optics physics, Karnataka University, Dharwad, **2011**.
4. "The role of torsional vibrations in the electronic absorption spectrum of acetone", Aparna Shastri, B.N. Raja Sekhar, Param Jeet Singh, 99th Indian Science Congress, KIIT University, Bhubaneswar, **2012**.
5. "VUV spectroscopy of SO2 isolated in argon matrix using synchrotron radiation", Param Jeet Singh, B.N. Raja Sekhar, V. Kumar, A. Mandal, Aparna Shastri and B.N. Jagatap. DAE-BRNS Symposium on Atomic, Molecular & Optical Physics-AMOP-2012, IISER, Kolkata, **2012**.
6. "Synchrotron based VUV spectroscopy in gas and matrix isolated phase" Param Jeet Singh, Anuvab Mandal, Vijay Kumar, A. Shastri, B.N. Raja Sekhar, B.N. Jagatap, The 7th Asia Oceania Forum for Synchrotron Radiation Research, Egret, Himeji, Japan, **2013**.

Others (Invited Talk)

1. "VUV Spectroscopy of Environmentally Important Molecules in Gas Phase and Matrix Isolated Phase Using Synchrotron Radiation" Param Jeet Singh, Anuvab Mandal, Vijay Kumar, Aparna Shastri, K. Sundararajan, B.N. Raja Sekhar and B.N. Jagatap, National Symposium on Radiation and Photochemistry, North East Hill University, Shillong, **2013**.

Publications during the course of the work not included in the thesis

1. “Photostimulated phosphor based image plate detection system for HRVUV beamline at Indus-1 synchrotron radiation source”, K. Haris, Param Jeet Singh, Aparna Shastri, Sunanda K., Babita K., S.V.N. Bhaskara Rao, Shabbir Ahmad and A. Tauheed, Nuclear Instruments and Methods in Physics Research-A **2014**, 767, 199-205.

2. “Vacuum ultraviolet photoabsorption spectroscopy of CH2Cl2 and CD2Cl2 in the energy region 50,000–95,000 cm^{-1}”, Anuvab Mandal, Param Jeet Singh, Aparna Shastri and B. N. Jagatap, J. Quant. Spectrosc. Radiat. Transf., **2014**, 149, 291-302.

3. “Vibronic and Rydberg series assignments in the vacuum ultraviolet absorption spectrum of nitrous oxide”, Aparna Shastri, Param Jeet Singh, Sunanda Krishnakumar, Anuvab Mendal, B.N. Raja Sekhar, R. D'Souza and B.N. Jagatap, J. Quant. Spectrosc. Radiat. Transf., **2014**, 147, 121-133.

4. “Electronic State Spectroscopy of Diiodomethane (CH2I2): Experimental and computational studies in the 30,000 to 95,000 cm^{-1} region”, Anuvab Mandal, Param Jeet Singh, Aparna Shastri, and B. N. Jagatap, J. Chem. Phys. **2014**, 140, 194312-1-11.

5. “Rydberg and valence excited states of dibromomethane in 35,000 – 95,000 cm^{-1} region studied using synchrotron radiation”, Anuvab Mandal, Param Jeet Singh, Aparna Shastri, Vijay Kumar, B.N. Raja Sekhar and B.N. Jagatap, J. Quant. Spectrosc. Radiat. Transf., **2014**, 144, 164-173.

05/12/2014

Param Jeet Singh

ACKNOWLEDGEMENTS

It is my great pleasure to acknowledge the many people for their direct or indirect help during the course of this work.

First and foremost I offer my most profound and sincere gratitude to my supervisor Prof. B.N. Jagatap for his valuable guidance, support, motivation, and enthusiasm, during the entire period of my research. He has supported me throughout my thesis work with constant encouragement, inspiration and knowledge whilst allowing me the room to work in my own way. My discussions with him have helped me not only to understand the subject but also to gain enough confidence and inspiration to look deeper into details of the problems. I consider myself very fortunate in having been associated with such as enthusiastic scientist. One simply could not wish for a better or friendlier supervisor.

I learnt the subject of VUV spectroscopy from Dr. Aparna Shastri and Dr. Richard D'Souza. They provided all possible help, advice and support for the experimental and theoretical work and offered several critical comments on the thesis. Molecular spectroscopy is indeed a painstaking exercise, which was however made enjoyable by their involvement in the work. I am indebted to them for all what they have done for me.

I express my gratitude to Dr. N.K. Sahoo for all his encouragement and support. I thank Dr. S.N. Jha for fruitful discussions and active involvement during development and commissioning of HRVUV beamline. Thanks are due to Dr. B.N. Raja Sekhar for his support and encouragement during development of MIS set-up and experiments on photophysics beamline and to Dr. S.V.N. Bhaskar Rao and Dr. Sunanda K. for help during experiments on HRVUV beamline. I thank Dr. K. Sundararajan and his colleagues at IGCAR, Kalpakkam for active collaboration for MIS.

I am thankful to Dr. P.D. Gupta for his encouragement for setting up MIS facility on Indus beamline. I extend many thanks to my doctoral committee members, Dr. S. K. Deb, Dr. A. P. Mishra and Dr. K. Sundararajan for their encouragement, keen assessment and vital suggestions.

Dr. S.V.G. Ravindranath and his electronics group provided all support in the electronic maintenance and data acquisition systems on the beamlines. Shri. K. Thankarajan and his team members of divisional workshop and also the members of the RRCAT workshop provided the necessary assistance during development and regular maintenance of beamlines. Indus synchrotron radiation source facility provided beamtime and required help during course of the work. Shri P. K. Kush and his colleagues in cryogenic section, RRCAT developed the cryostat for MIS system. I thank them all for facilitating the experimental program undertaken in this thesis.

I express my thanks and good wishes to my young colleagues, Anuvab, Vijay, Asim and Babita for help rendered during various stages of the work. Thanks are due to Akashdeep and Pankaj for their moral support during thesis work.

I owe a lot to my wife Sarabjeet Kaur, my parents, my brother Kamaljeet Singh and my relatives for their understanding and patience which enabled me to complete this work. They were perhaps ignored a lot due to my preoccupation with research work far away from home. Without their encouragement and understanding it would have been impossible for me to complete this work. Thanks to my daughters Eveleen and Amritleen for provided loving relief on many instant during this work.

Last but not least, my heartfelt gratitude to my school teacher Shri Surender Sundaram and my mentor at Panjab University Chandigarh Prof. Devender Mehta who instilled in me a fascination for research.

TABLE OF CONTENTS

Homi Bhabha National Institute
Ph. D. PROGRAMME

Name of the Student:	Param Jeet Singh
Name of the Constituent Institution:	Bhabha Atomic Research Centre Trombay, Mumbai - 400085, India
Enrolment No.:	PHYS01201004011
Title of the Thesis:	Synchrotron Radiation based VUV Spectroscopy of some Polyatomic Molecules of Environmental Interest
Board of Studies:	Physical Sciences

SYNOPSIS

Spectroscopy of atoms, molecules and clusters in the vacuum ultraviolet (VUV) region (6-25 eV) is of vital importance for understanding of their electronic structure and various photo-induced processes, principally, photoionization and photodissociation. At the basic level these studies help to validate and improve the predictions of the *ab-initio* quantum mechanical calculations, while at the applied level they find use in the understanding of photophysics and photochemistry pertaining to atmosphere, biological processes and astrophysical objects. The first ionization potential of most molecules lies typically in ~ 9-12 eV region. Spectroscopic studies in this region are therefore important for probing the excited state structure of molecules and understanding of phenomena occurring near and above the first ionization limit. These investigations cover a wide spectrum of issues relating to structure, electron correlations, and dynamics of photo-ionization, photo-dissociation and photo-fragmentation etc. Spectroscopy in the VUV region requires special sources and equipment. Synchrotron radiation (SR) is an intense and continuous source of radiation, which is ideally suited for this purpose. Spectroscopy of atoms and molecules using SR sources has been a subject of immense interest in recent years, having implications in diverse fields such as basic atomic and molecular physics, environmental science, astrophysics, astrochemistry, combustion dynamics, etc. [1-6].

Among the various spectroscopic techniques adopted in the VUV region, high resolution gas phase photoabsorption spectroscopy is a well-established technique which is ideally suited for studies involving the electronic structure, geometry, vibrational modes and vibronic interactions of excited states; both valence and Rydberg type. The high brilliance and continuous tunablity of SR sources have been exploited in gas phase VUV photoabsorption studies since the early days of storage rings and SR sources thereby providing exceedingly rich and crucial information on spectroscopy and structure of a large number of molecules. Much of this work is intimately connected with the molecules and molecular processes of importance in atmosphere and astrophysical objects. In addition to the gas phase studies, there has been a considerable interest in the spectroscopic studies of molecules trapped in inert gas matrices under cryogenic temperature. The matrix isolation spectroscopy (MIS) technique in conjunction with a SR source provides an ideal platform for studies of molecule-molecule and photon-molecule interactions in the crystalline and amorphous states of the matrix. Such studies are of significant importance in the understanding of spectroscopy and molecular processes in astrophysical ices, which is intimately connected to the emerging field of astrochemistry [7].

The present thesis deals with VUV photoabsorption spectroscopy of polyatomic molecules in gas and matrix isolated states using Indus-1 SR source, which is a 450 MeV storage ring with critical wavelength of 61 Å. Molecules investigated in this work are sulphur dioxide, acetone and chloroform; spectroscopy of which is of significant importance in atmospheric sciences. The work reported here consists of two broad objectives: First one is concerned with the design and development of high resolution vacuum ultraviolet (HRVUV) beamline and experimental stations for photoabsorption spectroscopy in gas and matrix isolated phases. The second one is related to the detailed investigations of VUV spectroscopy of the selected polyatomic molecules and their interpretations in the light of *ab initio* quantum chemical calculations. The thesis is organized in seven chapters and the details of the work included therein are as follows:

Chapter-1 presents a brief introduction to the subject of VUV spectroscopy of polyatomic molecules with a focus on the current developments in the field. Discussed here briefly are the important aspects of molecular physics including the Rydberg and valance states, molecular symmetry and group theoretical formalism, *ab initio* quantum chemical calculations and the importance of VUV spectroscopy in basic and applied sciences. The contents of this chapter, thus, provide both the motivation and the basis for the work presented in subsequent chapters.

Chapter-2 is devoted to the design and development of experimental systems for VUV spectroscopy, which includes the HRVUV beamline and experimental stations for photoabsorption spectroscopy and matrix isolation spectroscopy. HRVUV beamline is designed and developed to provide high resolution (resolving power $\geq 10^4$) in the VUV region 1050 – 3000 Å. The beamline consists of a pre-focusing optical system, a gas phase absorption set-up and a high resolution VUV spectrometer. The pre-focusing optical system, which consists of three cylindrical mirrors, serves the purpose of maximizing the throughput in the VUV region and matching the source aperture to the spectrometer aperture within the constraints of the SR source. The spectrometer is based on the off-plane Eagle mounting utilizing a concave spherical grating of radius of curvature 6.65 m. The central wavelength of interest is selected by appropriate rotation and translation of the grating. The spectrum is scanned by moving the exit slit-cum-photomultiplier (PMT) assembly vertically along the focal plane over a bandwidth of 160 mm about the central wavelength. The linear and rotational motion of the grating and the linear motion of the PMT are controlled by a 3-axis stepper motor controller and driver system. The beamline is interfaced with a PC for control and data acquisition. The beamline and spectrometer are maintained at 10^{-9} and 10^{-6} mbar vacuum respectively. The experimental station for gas phase absorption consists of an absorption cell and sample filling system. Performance of the beamline is evaluated by recording VUV photoabsorption spectra of Xe and O_2 and further compared with other high resolution (resolving power $\geq 10^4$) VUV beamlines (5-25eV) based on bending magnet as well as undulators installed on synchrotron sources around the world. Details of the optical and mechanical designs of various sub-systems of the beamline together with the optical alignment and performance evaluation of the beamline are discussed. In addition to the HRVUV beamline, a medium resolution (resolving power $\sim 10^3$) beamline, i.e., Photophysics beamline, on Indus-I synchrotron source is also used for the gas phase absorption studies. In order to study VUV spectroscopy of molecules trapped in inert gas matrices at cryogenic temperatures, a matrix isolation spectroscopy set-up is designed, developed and demonstrated by recording VUV absorption spectra of CO in Argon matrix. This set-up consists of a gas mixing chamber with deposition line, sample holder and an experimental chamber connected to a liquid He cryostat for matrix deposition. Design of the MIS set-up, its integration with the Photophysics beamline and its performance evaluation are reported in this chapter. The design and development of experimental systems discussed in this chapter thus form the main experimental part of the thesis, and the results obtained with them are presented in the chapters which follow.

Chapter-3 deals with the gas phase photoabsorption studies of sulphur dioxide (SO_2) in the VUV region using HRVUV beamline. Specific aim of these studies is to understand the nature of the

$\tilde{E}-\tilde{X}$ system lying in the region 7.5 – 9.0 eV (60500 – 72600 cm^{-1}). The electronic states and their symmetries involved in this system have been debated extensively in the literature. Owing to the high resolution afforded by the present experimental system, rich spectral features are obtained compared to the earlier reported studies. Vibronic analysis of the observed VUV spectra is carried out to show that most of the observed bands in the $\tilde{E}-\tilde{X}$ system can be arranged into four series with successive band spacing of 500 – 620 cm^{-1}. In addition two additional series are observed with average separation of ~ 1750 and ~1000 cm^{-1}. These vibronic intervals are significantly different from the frequencies of the ground state vibrational modes, i.e., ν_1 (symmetric stretch), ν_2 (bending) and the ν_3 (asymmetric stretch). In order to aid vibronic analysis, *ab initio* calculations using the GAMESS (USA) suite of programs are performed. Geometry optimization and vibrational frequencies of ground state are carried out using DFT and CIS methods. Vertical excitation energies are calculated at the ground state optimized geometry using TDDFT. Equilibrium geometry, vibrational frequencies and adiabatic excitation energies are also calculated for first few excited singlet and triplet states. Based on the *ab initio* calculations it is concluded that at least three dominant excitations involved in the $\tilde{E}-\tilde{X}$ system are $\tilde{X}\,{}^1\mathrm{A}_1 \rightarrow 3\,{}^1\mathrm{A}_1, \tilde{X}\,{}^1\mathrm{A}_1 \rightarrow 2\,{}^1\mathrm{A}_1$ and $\tilde{X}\,{}^1\mathrm{A}_1 \rightarrow 2\,{}^1\mathrm{B}_1$. The observed vibrational features are found to be mainly due to excitation of the combination modes (ν_1 + ν_2) and (ν_2 + ν_3) with some contributions from ν_1 and ν_3. Geometry optimization calculations indicate that the molecule maintains C_{2V} symmetry in these excited states although the bond lengths and bond angle do differ from their ground state values. This work in totality provided a consolidated picture of the $\tilde{E}-\tilde{X}$ system for the first time.

Chapter-4 presents a detailed work on VUV spectroscopy of acetone-h_6 (CH_3COCH_3) and its deuterated counterpart acetone-d_6 (CD_3COCD_3). The UV-VUV photoabsorption spectra of these molecules are recorded in the region 3.5 – 11.8 eV (28000 – 95000 cm^{-1}). The VUV spectrum of acetone shows extensive Rydberg series (ns, np and nd) converging to its first ionization potential at 9.708 eV. Vibronic assignments are carried out by taking into account the symmetry selection rules and contributions of hot bands from low lying torsional modes. These two considerations provide significantly improved vibronic assignments compared to earlier reported works [8] where these issues are not taken into account. Revised quantum defect values for some of the Rydberg transitions and a few new assignments are also proposed in this work. Several non-totally symmetric modes are observed arising due to the Herzberg-Teller effect. Some of the unresolved questions in the VUV spectrum of acetone-h_6 are the existence of transitions with multiple assignments, difficulty in unambiguous location of the ν_{00} origins of some of the excited states, and the observation of anomalous quantum defects in nd_{xy} series. These issues are sorted out by the study of VUV photoabsorption spectrum of acetone-d_6, which is reported for the first time. A comparative study of the Rydberg series and accompanying vibronic structure observed in acetone-h_6 and acetone-d_6 has clarified and consolidated many of the vibronic assignments. Attribution of the anomalous intensity pattern observed in acetone-h_6 to vibronic coupling with nearby valence states of the same symmetry is confirmed on the basis of observation of the same effect in acetone-d_6. The frequency of the ν_{19}' mode of the $3p_y$ state is obtained as 340 ± 5 cm^{-1} for acetone-d_6 on the basis of observation of an extensive progression of this mode. This chapter describes a complete quantum defect analysis and vibronic analysis of Rydberg series observed in acetone-h_6 and acetone-d_6, thus providing a unified picture of the VUV spectroscopy of acetone and its deuterated derivative.

Chapter-5 presents a detailed investigation of the electronic spectra of chloroform ($CHCl_3$) and its deuterated counterpart ($CDCl_3$) in the energy region 6.2 – 11.8 eV (50,000 – 95000 cm^{-1}) using Photophysics beamline. Rydberg series converging to the first four ionization limits at 11.48, 11.91, 12.01 and 12.85 eV corresponding to excitation from the $1a_2$, $4a_1$, 4e, 3e orbitals of $CHCl_3$ respectively are identified and analyzed. Quantum defect values are observed to be consistent with excitation from the chlorine lone pair orbitals. Analysis of Rydberg series and vibronic features observed in the electronic absorption spectra is greatly aided by quantum chemical computations. The ground state geometry optimization and vibrational frequency calculations for neutral and ionized $CHCl_3$ and $CDCl_3$ are performed using DFT. The vertical excited state energies are calculated at the optimized ground state geometries using the TDDFT method. The experimental spectrum is found to be in good agreement with that predicted by TDDFT calculations. Comparison of the experimental and theoretical data is carried out by establishing a correspondence between the Rydberg series members originating from a given MO, i.e. $1a_2$, $4a_1$, 3e or 4e (based on quantum defect analysis) with the theoretically calculated energies for excitation from that particular MO. Vibrational progressions observed in the region of 72,500 – 76,500 cm^{-1} have been reassigned to ν_3 (CCl_3 s-deform) mode and combination modes of ν_3 and ν_6 (CCl_3 d-deform) belonging to $1a_2 \rightarrow 4p$ transition in contrast to earlier studies [8] where they were assigned to a ν_3 progression superimposed on the $3e \rightarrow 4p$ Rydberg transition. The assignments are further confirmed based on study of vibronic spectrum of $CDCl_3$ whose VUV photoabsorption spectrum is reported here for the first time. The frequencies of the ν_3 and ν_6 modes in the 4p Rydberg state of $CHCl_3$ ($CDCl_3$) are proposed to be ~ 450 (407) cm^{-1} and 105 (137) cm^{-1} respectively based on the vibronic analysis. This chapter presents a consolidated analysis of the VUV photoabsorption spectrum of chloroform.

Chapter-6 is devoted to the study of VUV spectroscopy of molecules isolated in inert gas matrices at cryogenic temperatures. These studies are a prelude to the understanding of VUV photo-induced processes in these systems and assume importance in investigation of molecule-matrix interactions. In order to understand the differences in the spectra in gas phase and matrix isolated phase, VUV spectra of SO_2 and acetone are studied in some detail. The gas phase spectroscopy of these molecules is reported in Chapter-3 and -4 of this thesis. Experiments are performed by isolating SO_2 and acetone in Argon matrices at 10 K, at different ratios ranging from 0.2:1000 to 5:1000. It is quite well established that in condensed phase, electronic states having a Rydberg character are either shifted considerably to higher energies or simply obliterated from the spectrum. In contrast valence transitions show small shifts in condensed phase compared to the gas phase [9]. Electronic transitions observed in matrix isolated acetone show blue shifts of ~ 3000 – 6000 cm^{-1}, as expected in view of the Rydberg nature of these transitions. In the case of SO_2, the first three absorption bands are not shifted much in the matrix phase as compared to the gas phase, whereas the higher excited states show larger shifts. This is in line with the assignment of the first three gas phase absorption systems to valence transitions, and higher bands to transitions of valence-Rydberg mixed or Rydberg character. This chapter thus presents the investigations of VUV absorption processes in matrix isolated molecules.

Finally the important conclusions of the present study and scope for future work are discussed in Chapter-7.

REFERENCES

[1]. Y. Hatano, Rad. Phys. Chem.67 (2003) 187 – 198.

[2]. P. Limão-Vieira, D. Duflot, E. Vasekova, J.M. Lourenco, P.M. Santos, S.V. Hoffmann, N.J. Mason, J. Delwiche, M.J. Hubin-Franskin, J. Phys. Chem. A 112 (2008) 2782 – 93.

[3]. N.J. Mason , A. Dawes, R. Mukerji, E.A. Drage, E. Vasekova, S.M. Webb, P. Limão-Vieira, J. Phys. B: At. Mol. Opt. Phys. 38 (2005) S893 – 911.

[4]. F. Ferreira da Silva, D. Almeida, G. Martins, A.R. Milosavljević, B.P. Marinković, S.V. Hoffmann, N.J. Mason, Y. Nunes, G. Garcia, P. Limão-Vieira, Phys. Chem. Chem. Phys.12 (2010) 6717 – 31.

[5]. Y-J Wu, H-F Chen, C. Camacho, H. A. Witek, S-C Hsu, M-Y Lin, S-L Chou, J. F. Ogilvie, and B-M Cheng, Astrophy. J.701 (2009) 8 – 11.

[6]. J.P. Connerade and M.A. Baig in: G.V. Marr (Ed.), Handbook on Synchrotron Radiation, North Holland, Amsterdam, (1987) 175 – 240.

[7]. G. Monninger, M. Förderer, P. Gürtler, S. Kalhofer, S. Petersen, L. Nemes, P. G. Szalay, W. Krätschmer, J. Phys. Chem. A 106 (2002) 5779 – 5788.

[8]. M. Nobre, A. Fernandes, F. Ferreira da Silva, R. Antunes, D. Almeida, V. Kokhan, S.V. Hoffmann, N.J. Mason, S. Eden. P. Limão-Vieira. Phys. Chem. Chem. Phys. 10 (2008) 550 – 60.

[9]. M.B. Robin, Higher Excited States of Polyatomic Molecules Vol. I, Academic press, New York and London (1974).

Publications:

1. First commissioning results from high resolution vacuum ultraviolet beamline at indus-1 synchrotron source.

   Param Jeet, Singh, Aparna Shastri, R. Sampath Kumar, S.N. Jha, S.V.N. B. Rao, R. D’Souza and B.N. Jagatap

   Nuclear Instruments and Methods in Physics Research-A, 634 (2011) 113 – 119.

2. VUV photoabsorption spectroscopy of Sulphur dioxide in the 1400 -1600 Å region: vibronic analysis of the $\tilde{E}-\tilde{X}$ system

   Param Jeet, Singh, Aparna Shastri, R. D’Souza, S.V.N. B. Rao and B.N. Jagatap

   J. Quant. Spectrosc.Radiat.Transf.113 (2012) 267 – 278.

3. The role of torsional modes in the electronic absorption spectrum of acetone.

   Aparna Shastri, Param Jeet Singh, B.N. Raja Sekhar, R. D'Souza and B.N. Jagatap

   J. Quant. Spectrosc.Radiat.Transf.113 (2012) 1553-1565.

4. Excited state vibrational modes of a few triatomic molecules of environmental interest.

   Aparna Shastri, Sunanda K., Param Jeet Singh, B.N. Raja Sekhar, S.V.N. Bhaskar Rao, R. D’Souza and B.N. Jagatap

   Asian Journal of spectroscopy- special issue (2012) 107-119.

5. Effect of isotopic substitution in the electronic absorption spectrum of acetone: VUV photoabsorption studies of acetone-d_6.

   Param Jeet Singh, Aparna Shastri, B.N. Raja Sekhar, R. D’Souza, B.N. Jagatap

   J. Quant. Spectrosc.Radiat.Transf.114 (2013) 20-28.

6. Rydberg states of chloroform studied by VUV photoabsorption spectroscopy.

   Param Jeet Singh, Aparna Shastri, R. D'Souza and B.N. Jagatap

   J. Quant. Spectrosc.Radiat.Transf.129 (2013) 204-213.

Signature of the Student:

Date: 09.11.2013

Doctoral Committee:

S. No.	Name	Designation	Signature	Date
1.	Dr. S. K. Deb	Chairman	Sudip Kumar Deb	9/11/2013
2.	Dr. B. N. Jagatap	Convener		09.11.2013
3.	Dr. K. Sundararajan	Member		9.11.2013
4.	Dr. A. P. Mishra	Member	Adya Prasad Mishra	9/11/13

List of Figures

List of Tables

Chapter-1

Introduction

Vacuum ultraviolet (VUV) generally refers to the 6-25 eV energy region of the electromagnetic spectrum. The first ionization potential (*IP*) of most molecules generally lies in the region ~9–12 eV. Spectroscopic studies in the VUV are therefore important for probing the excited state structure of molecules and understanding of phenomena occurring near and above the first *IP*, i.e., various photo-induced processes, like photoionization, photodissociation and photofragmentation [1-5] in molecules and clusters. At the basic level these studies help to validate the predictions of the *ab-initio* quantum mechanical calculations [6], while at the applied level they find use in understanding of photophysics and photochemistry of the atmosphere [7], biological processes [8] and astrophysical objects [9].

Synchrotron radiation (SR) is an intense and continuously tunable source of radiation, which is ideally suited for VUV spectroscopy [1-9]. The high brilliance and continuous tunablity of SR sources have been exploited in gas phase VUV photoabsorption studies since the early days of storage rings and SR sources, thereby providing exceedingly rich and crucial information on spectroscopy and structure of a large number of molecules. Among the various spectroscopic techniques adopted in the VUV region, high resolution gas phase photoabsorption spectroscopy is a well-established technique which is well suited for studies involving the electronic structure, geometry, vibrational modes and vibronic interactions of excited states; both valence and Rydberg type. The scope of these studies is further broadened by employing the technique of matrix isolation spectroscopy (MIS), wherein gas molecules are trapped in inert gas matrices under cryogenic temperature and studied with suitable spectroscopic technique [10]. MIS has widely been used in the study of stable molecules [11], transient species, i.e., radicals and ions generated by photolysis or discharge [12], weak molecular interactions [13-15], reaction intermediates and mechanisms [12, 16-18], and also in the investigations relating to atmospheric chemistry [19] and astrochemistry [7, 9, 20, 21].

The present thesis deals with VUV photoabsorption spectroscopy of polyatomic molecules in gas phase and matrix isolated phase using Indus-1 SR source. The total scope of the work includes development of beamline and experimental stations, generation of photoabsorption spectra and their interpretation with help of *ab initio* quantum chemical calculations. The molecules chosen for these investigations are: sulphur dioxide (SO_2), acetone [$(CH_3)_2CO$, acetone-h_6], deuterated acetone [$(CD_3)_2CO$, acetone-d_6], chloroform ($CHCl_3$) and deuterated chloroform ($CDCl_3$), which are of significant atmospheric importance. This chapter provides a brief overview of the experimental and theoretical issues involved in the VUV molecular spectroscopy.

1.1. Synchrotron radiation source

SR is produced when a relativistic charge particle (typically electron) is accelerated radially in a magnetic field. It has many unique properties like broad continuum energy spectrum from infrared to X-ray region, high flux, high brilliance, high collimation, pulsed time structure and polarization (linear in plane of orbit and elliptical above and below) which make it a very powerful tool in scientific research, particularly in the VUV region. Moreover SR is produced in ultra-high vacuum, thus, providing a spectroscopically pure source which is an added advantage over traditional laboratory sources. Over the past few decades, rapid scientific and technological advances have resulted in a large number of dedicated SR facilities the world over. In India, two storage rings *viz*. Indus-1 and Indus-2 of electron energies 450 eV and 2.5 GeV are in operation at Raja Ramanna Center for Advanced Technology (RRCAT), Indore [22, 23]. With a critical wavelength (λ_c) of 61Å, Indus-1 SRS is ideally suited for VUV studies. A schematic layout of the major components of the injection system and Indus-1 is shown in Fig. 1.1.

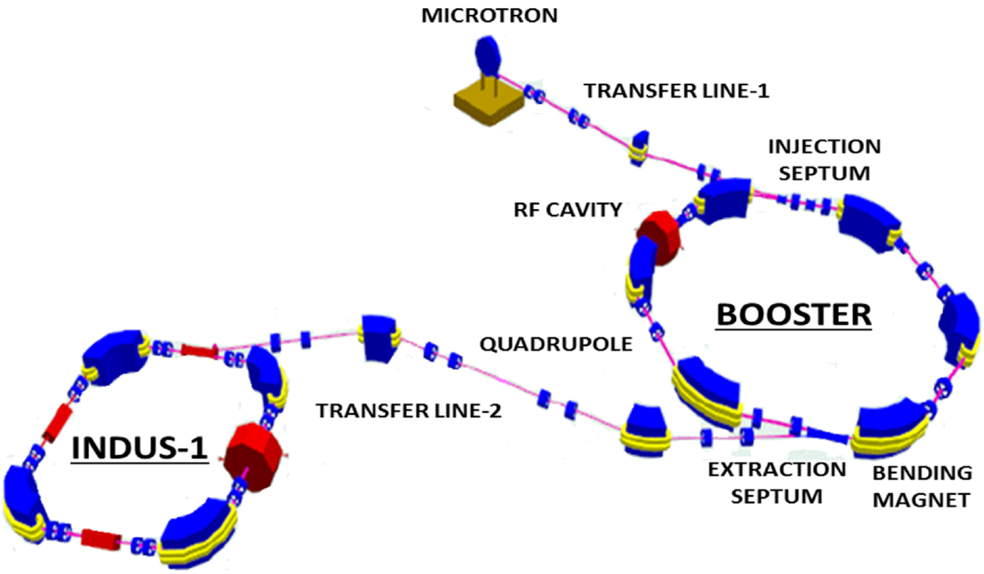

Figure 1.1: Schematic layout of Indus-1 synchrotron facility.

Briefly, electrons produced by an electron gun are accelerated to 20 MeV in microtron and injected into a booster synchrotron where their energy is further increased to 450 MeV. The microtron and booster synchrotron form the injection system for both Indus-1 and Indus-2. The 450 MeV electrons are extracted from the booster through a transport line and stored in the Indus-1 storage ring at 100 mA. Some important parameters of Indus-1 source are given in Table 1.1. Two beamlines for VUV spectroscopy are currently in operation at Indus-1 *viz.* the medium resolution photophysics (PPS) beamline and high resolution VUV (HRVUV) beamline. The photoabsorption studies presented in this thesis are carried out using these two beamlines. Development of the HRVUV also forms a part of this thesis work.

Table 1.1: Parameters of the Indus-1 storage ring

Energy	450 MeV
Current	100 mA
Critical wavelength	61 Å
Spectral flux (at λ_c)	7.2×10^{11} photons/ sec/mrad/0.1% BW
Circumference	18.96 m
Dipole field	1.5 T
Energy loss per turn	3.6 keV
Revolution frequency	15.82 MHz
Harmonic number	2

1.2. Electronic states: Rydberg and valence

The electronic levels in a molecule may be designated based on their energies as represented in Fig.1.1 for the case of $CHCl_3$. The levels arising from the closed inner shells of the atoms are the core levels and they are localized near the nuclei. The valence levels are above the core levels; the highest occupied and the lowest unoccupied molecular orbitals (MOs) are HOMO and LUMO respectively.

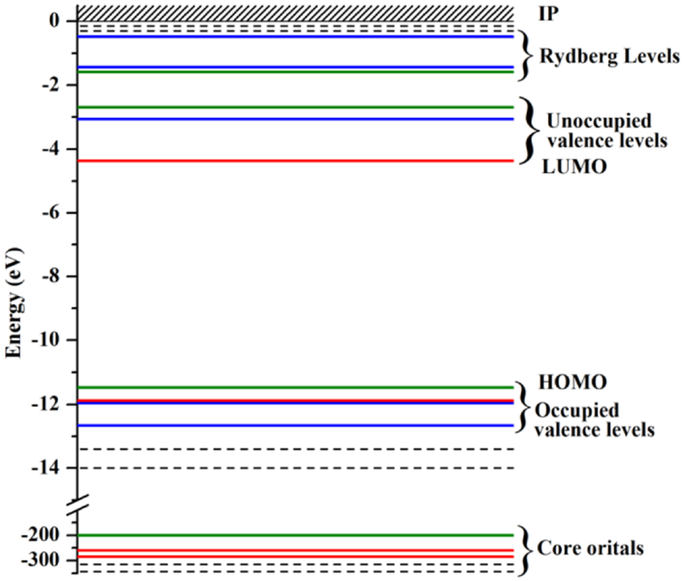

Figure 1.2: Energy level diagram of $CHCl_3$ showing core, valence and Rydberg levels.

Excited states of molecules are usually classified into valence and Rydberg type depending on the nature of the excited MO. For valence states, the principal quantum number (n) of the atomic orbitals giving rise to the excited MO are same as that in the ground state. In case of Rydberg states, the value of n is at least one more in the excited MO than in the ground state and the molecule resembles a hydrogenic system. Molecular Rydberg states can be described as an ionized core with a weakly bound electron, dominated by configurations in which electrons are excited to diffuse orbitals. Although the ion core is not spherically symmetric, the molecular Rydberg series, similar to the atomic case, can be fitted to the well-known Rydberg formula,

$$E_n = IP - \frac{R}{(n-\delta_l)^2}, \tag{1.1}$$

where E_n is the energy of the transition, IP is the ionization potential, R is the Rydberg constant, n is the principal quantum number and δ_l is the quantum defect that depends on the angular momentum l. The quantum defect value reflects interactions of molecular ion core with the Rydberg orbitals and depends on the size and shape of the ion core. If the HOMO is approximated by a lone pair (nonbonding) on a particular atom in the molecule, quite often the observed molecular quantum defects closely follow the corresponding atomic quantum defects. For example the HOMOs of acetone and chloroform (*cf.* Chapter-4 and -5) are approximated to lone pairs of O and Cl atoms respectively. The δ_l values obtained for Rydberg series of these molecules are consistent with the atomic quantum defect values of O and Cl. Usually the value of δ_l is almost constant throughout a series converging to a particular IP. Large deviations of δ_l from the characteristic values indicate interaction with nearby valence states and/or strong perturbations by the core. It may also be mentioned here that for the low-lying Rydberg states there is also a possibility of mixing between Rydberg and valence states [24].

The electronic transitions are often accompanied by vibrational excitations, i.e., vibronic transitions. The geometry of polyatomic molecules in excited states is often different from the ground state which leads to the observation of vibrational progression with relative intensities governed by the Franck-Condon overlap. Usually, long progressions are observed when there is a considerable change in geometry upon electronic excitation. The expected position of the vibronic band origin ν_{00} for an electronic transition of a polyatomic molecule within the harmonic oscillator approximation is given by

$$\nu_{00} = \left(E_e^{'} - E_e^{''}\right) + \left(\sum_{i=1}^{3N-6} \frac{\omega_i^{'}}{2} - \sum_{i=1}^{3N-6} \frac{\omega_i^{''}}{2}\right), \tag{1.2}$$

where single and double prime correspond to upper and lower state. Note that the difference in the zero point energy of the ground and excited state has an important contribution in assignment of the transitions, and must be taken into account during analysis and interpretation of the observed spectrum [25].

1.3. Molecular symmetry

Group theory is a useful tool in molecular spectroscopy, which is widely used to classify and label molecular energy levels. Using the concepts of molecular symmetry and group theory one can formulate MOs and obtain qualitative information on the possibility of transitions between energy levels without the need for detailed quantum mechanical calculations.

There exists five types of basic symmetry operations and associated symmetry elements for specifying molecular symmetry *viz.* a) n-fold rotation about an axis (C_n: rotation by an angle $2\pi/n$), b) reflection about a plane (vertical plane σ_v, horizontal plane σ_h and dihedral plane σ_d), c) inversion about a center of symmetry (i), d) n-fold improper rotation about an axis, also called rotation-reflection (S_n) and e) identity (E). Once the symmetry operations are known, one can classify all molecules into point groups, which are mathematically represented using matrices.

The character table of a point group is essentially a collection of the traces of the irreducible matrix representations of the symmetry operations arranged in a standard way [26, 27] and is very useful in deducing molecular properties and selection rules. Character tables for the point groups used in the present work, *viz.* C_{2v} (SO_2 and acetone) and C_{3v} ($CHCl_3$) are given in Tables 1.2 and 1.3 [27].

Table 1.2: Character table for C_{2v} point group

	E	C_2 (z)	σ_v(xz)	σ_v(yz)	linear, rotations	quadratic
A_1	1	1	1	1	z	x^2, y^2, z^2
A_2	1	1	-1	-1	R_z	xy
B_1	1	-1	1	-1	x, R_y	xz
B_2	1	-1	-1	1	y, R_x	yz

Table 1.3: Character table for C_{3v} point group

	E	$2C_3$ (z)	$3\sigma_v$	linear, rotations	quadratic
A_1	1	1	1	z	x^2+y^2, z^2
A_2	1	1	-1	R_z	
E	2	-1	0	(x, y) (R_x, R_y)	(x^2-y^2, xy) (xz, yz)

For the vibronic transitions of interest in this thesis, the group theoretical form of the dipole selection rules [25, 28] can be written as,

$$\Gamma(\psi_{ev}^{'}) \times \Gamma(\mu) \times \Gamma(\psi_{ev}^{''}) \supset A, \tag{1.3}$$

where Γ is the irreducible representation, ψ_{ev} and μ are vibronic wave function and dipole moment operator respectively and A stands for totally symmetric species of the concerned point group. In Eq. (1.3), the subscripts e and v denote respectively the electronic and vibrational coordinates, and the upper and lower states are denoted by single and double primes respectively. Under the Born-

Oppenheimer (B.O.) approximation, the vibronic wave function can be written as $\psi_{ev} = \psi_e \psi_v$. The selection rule for vibronic transitions then becomes

$$\Gamma(\psi_e^{'}) \times \Gamma(\psi_v^{'}) \times \Gamma(\psi_e^{''}) \times \Gamma(\psi_v^{''}) = \Gamma(\mathrm{T_x}) \text{ and/or } \Gamma(\mathrm{T}_y) \text{ and/or } \Gamma(\mathrm{T}_z) , \tag{1.4}$$

where T_x, T_y and T_z represent translation along x, y and z axes respectively.

1.4. Computation of molecular electronic structure

Ab initio molecular structure calculations provide considerable insight in analysis and interpretation of experimentally observed spectra. Advent of high-speed computers has made electronic structure calculation an important component of theoretical and experimental molecular physics research [29]. In this section, the computational techniques used in the calculation of geometries, vibrational frequencies and energies of the ground and excited states of molecules are discussed briefly. These techniques are extensively used in the subsequent chapters.

The non-relativistic Hamiltonian of an *n*-electrons molecule under the B.O. approximation is given as

$$H = -\frac{\hbar^2}{2m}\sum_{i=1}^{n}\nabla_i^2 - \sum_{i,I}^{n,N}\frac{Z_I e^2}{r_{iI}} + \frac{1}{2}\sum_{i\neq j}^{n}\frac{1}{r_{ij}} + \frac{1}{2}\sum_{I\neq J}^{N}\frac{Z_I Z_J e^2}{r_{IJ}}, \tag{1.5}$$

where (i , j) and (I, J) run over electrons (n) and nuclei (N) respectively, m and e denote the mass and charge of electron, Z_I is the atomic number of I^{th} nucleus and r_{ab} is the distance between particles a and b. In Eq. (1.5), the last term is nuclear repulsion which is constant. The second and third terms in Eq. (1.5) are pair wise attraction and repulsion terms, implying that no particle is moving independently of all of the others i.e., the motion of the electrons is correlated. This problem is tackled using Hartree-Fock (HF) method under independent particle approximation. Here each electron is considered to be moving in the electrostatic field of nuclei and the average field of other (n-1) electrons. Denoting the spin orbital (SO) of i^{th} electron by $\chi_\alpha(x_i)$, where x_i and α are respectively the coordinates (including spin) and the quantum number, the wave function of the molecular system is written as the standard Slater determinant,

$$|\psi_0\rangle = (n!)^{-1/2} \sum_{P=1}^{n!} (-1)^p \, P\{\chi_\alpha(x_1)\,\chi_\beta(x_2)\ldots\chi_\gamma(x_n)\}, \tag{1.6}$$

where p is the parity of the permutation P. Now using the variational principle, the best SOs that minimize the electronic energy, $\mathrm{E}_0 = \langle \psi_0 | \mathrm{H} | \psi_0 \rangle$, are obtained. The essence of HF method is to replace the many-electron problem by a one-electron problem in which electron-electron repulsion is treated in an average manner; the treatment therefore ignores the electron correlation.

Electron correlation can be treated conveniently using configuration interaction (CI) and Møller–Plesset (MP) many-body perturbation theory techniques. In the CI method, the electron correlation is considered by taking a linear combination of the HF wave functions with a large number of excited configurations. The expansion coefficients are then varied using the variational approach until a minimum energy is achieved. Since excited configurations have a large percentage of their probability density far away from the nuclei, convergence is slow and large numbers of configurations need to be included, making this method computationally demanding. Electron correlation can also be estimated using Møller-Plesset (MP) method which is based on many body perturbation theory rather than variational calculations. While in general the perturbation calculations may be worked out to n^{th} order (MPn), in the present work MP2 level computations are used.

Another useful approach for computation of molecular structure is given by the density functional theory (DFT), which is based on the electron density $\rho(\vec{r})$. DFT rests on two theorems by Hohenberg and Kohn [30], namely, (a) The ground-state energy E is a unique functional of $\rho(\vec{r})$:

$E = E[\rho(\vec{r})]$ and (b) $\rho(\vec{r})$ that minimizes the energy of the overall functional is the true electron density corresponding to the full solution of the Schrödinger equation.

Consider for example a molecule in which paired electrons are described by the same spatial one-electron orbitals. The exact ground-state electronic energy E may be written as [31],

$$\begin{aligned} E[\rho] = &-\frac{\hbar^2}{2m}\sum_{i=1}^{n}\int \psi_i^*(\vec{r}_1)\nabla_1^2\psi_i(\vec{r}_1)d\vec{r}_1 - \frac{e^2}{4\pi\varepsilon_0}\sum_{I=1}^{N}\int \frac{Z_I}{r_{I1}}\rho(\vec{r}_1)d\vec{r}_1 \\ &+\frac{1}{2}\frac{e^2}{4\pi\varepsilon_0}\iint \frac{\rho(\vec{r}_1)\rho(\vec{r}_2)}{r_{12}}d\vec{r}_1 d\vec{r}_2 + E_{XC}[\rho], \end{aligned} \tag{1.7}$$

where the one-electron SOs $\psi_i\ (i = 1, 2, ..., n)$ are the Kohn-Sham (KS) orbitals. The first three terms represent the kinetic energy of the electrons, the electron-nucleus attraction and the Coulomb interaction between the total charge distribution at $\vec{r}_1$ and $\vec{r}_2$. The last term, the exchange-correlation energy (E_{XC}), which takes into account all non-classical electron-electron interactions is a functional of the density. Since the true functional form of E_{XC} is not known, in practice approximate forms of the functional are used in the variational method to minimize the energy. The KS equations for the one-electron orbitals $\psi_i(\vec{r}_1)$ have the form

$$\left\{-\frac{\hbar^2}{2m}\nabla_1^2 - \frac{e^2}{4\pi\varepsilon_0}\sum_{I=1}^{N}\frac{Z_I}{r_{I1}} + \frac{e^2}{4\pi\varepsilon_0}\int \frac{\rho(\vec{r}_2)}{r_{12}}d\vec{r}_2 + V_{XC}(\vec{r}_1)\right\}\psi_i(\vec{r}_1) = \varepsilon_i\psi_i(\vec{r}_1), \tag{1.8}$$

where ε_i are the KS orbital energies and the exchange-correlation potential, V_{XC}, is the functional derivative of the exchange-correlation energy, $V_{XC}[\rho] = \delta E_{XC} / \delta\rho$. If E_{XC} is known, then V_{XC} can be obtained. The significance of the KS orbitals is that they allow the density ρ to be computed from Eq. (1.7). The KS equations are solved in an iterative and self-consistent fashion till a convergence criterion is satisfied [32]. The exchange correlation functional is often separated into an exchange functional and a correlation functional.

A variety of exchange correlation functionals have been developed for DFT calculations and these include Becke-3-Lee-Yang-Parr (B3LYP) [33, 34], Perdew-Burke-Ernzerhof (PBE0) [35] etc. The DFT method is computationally less demanding than *ab initio* methods like CI and MP2 while taking into account electron correlation quite satisfactorily. Geometry optimization, i.e., finding the minimum energy configuration in terms of bond lengths and bond angles of a molecule, assumes considerable importance in molecular physics [25, 36]. The mass weighted Hessian or force constant matrix which consists of the second derivatives of the energy with respect to the normal coordinates is used to calculate the vibrational frequencies. For a true minimum, all the second derivatives must be positive.

For calculation of excited state energies the time-dependent density functional theory (TDDFT) is used. The time-dependent KS equations are given by [31],

$$\left\{-\frac{\hbar^2}{2m}\nabla_1^2-\frac{e^2}{4\pi\varepsilon_0}\sum_{I=1}^{N}\frac{Z_I}{r_{I1}}+\frac{e^2}{4\pi\varepsilon_0}\int\frac{\rho(\vec{r}_2,t)}{r_{12}}d\vec{r}_2+V_{ext}(t)+V_{XC}(\vec{r}_1,t)\right\}\psi_i(\vec{r}_1)=i\hbar\frac{\partial}{\partial t}\psi_i(\vec{r}_1,t)\,, \qquad (1.9)$$

$$\rho(r,t)=\sum_{i=1}^{n}\left|\psi(\vec{r},t)\right|^2\,, \qquad (1.10)$$

where the external potential V_{ext}, the exchange–correlation potential, the KS orbitals and the density are all time-dependent. The goal of TDDFT is to find how the density changes in response to the varying external potential. The nature of the excited states calculated using TDDFT can be grossly determined by means of the Λ-diagnostic, where Λ is a measure of the spatial overlap in a given excitation [37]. As a thumb rule the transition with low Λ values (≤ 0.3) is interpreted as predominantly Rydberg in nature while high Λ value (≥ 0.5) signifies largely the valence nature. Intermediate values of Λ may suggest mixed valence-Rydberg character.

For the molecules investigated in this thesis, all computations are carried out using the GAMESS (USA) suite of programs [38]. Parallel mode of computation is used when necessary. Geometry optimization and vibrational frequencies are first computed for the ground state using DFT or MP2 methods. Vertical excited states up to the first *IP* are then calculated at the optimized geometry of the ground state using TDDFT or configuration interaction singles (CIS). The vibrational frequencies in the Rydberg states are assumed to follow the ionic frequencies closely since the structure of highly excited states is expected to be closer to that of the ion. In order to estimate the vibrational frequencies in excited state, the ground states of the ions are also optimized and their vibrational frequencies are calculated. Analysis of vibronic features in the present experimental electronic absorption spectra is aided by these computed values.

1.5. Construction of molecular orbital energy level diagram

In this section group theoretical principles as applied to construct MOs are developed. Using the concept of ligand group orbitals (LGOs), it is possible to decipher the symmetry and energy ordering of the MOs [39]. Note here that the orbitals of ligands cannot be treated independently since they transform under symmetry operations of the concerned molecular point group.

An MO is constructed from the linear combination of atomic orbitals of the same symmetry and close in energy [29]. In case of a polyatomic molecule, it is instructive to identify the central atom and the ligand groups attached to it. Symmetry species of *s* orbitals are always given by the totally symmetric irreducible representation of the point group. Symmetry species of *p* and *d* orbitals are identified from the columns of the character table that specify the transformation of (x, y, z) and $(z^2, yz, x^2\text{-}y^2$ etc.). The decomposition of the reducible representation of LGOs is found using well known group theoretical reduction formula,

$$n_{a_i} = \frac{1}{h}\sum_R g\chi_{a_i}(R)\chi_{red}(R), \tag{1.11}$$

where n_{a_i} is the frequency of the a_i^{th} irreducible representation in the reducible representation, h (g) is order of the group (class), R represents the symmetry operation, and $\chi_{a_i}(R)$ and $\chi_{red}(R)$ are the characters of the irreducible and reducible representation respectively. MOs are formed by combining orbitals of the central atom and LGOs corresponding to the same symmetry, thereby giving rise to bonding and anti-bonding orbitals. The residual orbitals of the central atom and LGOs for which there exist no corresponding orbitals of the same symmetry give rise to non-bonding MOs. In what follows, the construction of MOs for sulphur dioxide, acetone and chloroform is discussed.

1.5.1. Sulphur dioxide (SO_2)

SO_2 is a bent molecule belonging to C_{2v} point group with S as the central atom. Following the character table of C_{2v} group (Table 1.2), it is clear that the 3*s* valence orbital has a_1 symmetry, while the 3*p* valence orbitals are of a_1, b_1 and b_2 symmetry. Symmetries of LGOs may be identified by considering the internal coordinates (σ bonds) as shown in Fig. 1.3. The reducible representations for bonding LGOs are obtained from the number of unmoved internal coordinates (σ) during each symmetry operation as given in Table 1.4.

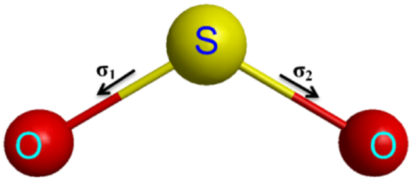

Figure 1.3: SO_2 molecule showing internal coordinate

Table 1.4: Reducible representation of internal coordinates of SO_2

C_{2v}	E	C_2 (z)	σ_v(xz)	σ_v(yz)
Γ_{red} (bonding)	2	0	0	2

This reducible representation can be decomposed into irreducible representations using Eq. (1.11) as $n_{a_1} = 1, n_{a_2} = 0, n_{b_1} = 0, n_{b_2} = 1$. Thus the symmetries of LGOs for SO_2 are a_1+b_2. The 2s orbitals of the O atoms have not been considered in this diagram as they lie lower in energy. The orbital energy level diagram of SO_2 generated using above symmetries is shown in Fig. 1.4.

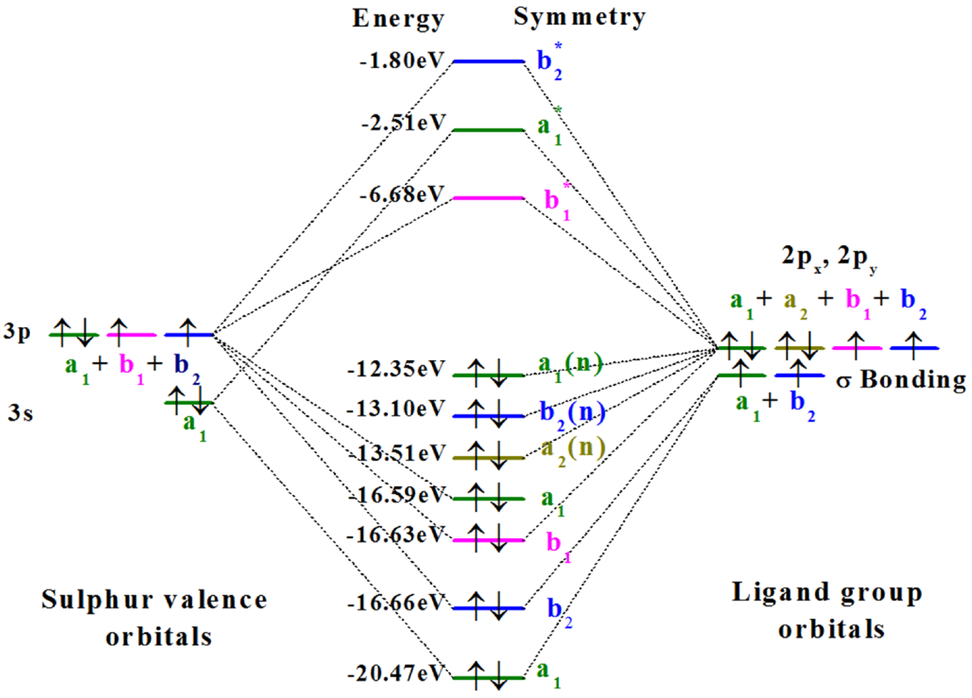

Figure 1.4: Molecular orbital energy diagram of SO_2. Energy of the orbitals are from the calculation using RHF taking *IP* (12.346 eV) value as zero.

1.5.2. Chloroform ($CHCl_3$)

$CHCl_3$ belongs to C_{3v} point group with central atom C. From the C_{3v} character table (Table 1.3), the 2*s* valence orbital of central atom has a_1 symmetry, while the symmetries of 2*p* valence orbitals are a_1 and *e*. Symmetries of LGOs for three Cl atoms and one H atom are identified from the internal coordinates for four σ bonds as shown in Fig. 1.5.

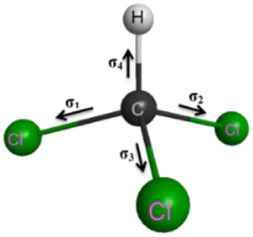

Figure 1.5: Internal coordinate of chloroform

The reducible representations for bonding LGOs are found from the number of unmoved internal coordinated (σ) during each symmetry operation as given in Table 1.5. It is decompose into irreducible representations using Eq. (1.11) as $n_{a_1} = 2, n_{a_2} = 0, n_e = 1$. Thus the symmetries of LGOs are 2a_1 + e. The symmetries of lone pairs of LGOs are identified by constructing reducible representations of all six lone pairs from 3p orbitals belonging to the three Cl atoms as shown in Table 1.6, which gives symmetries of lone pairs as $a_1 + a_2 + 2e$. It is important to note here that the electron density of the lone pairs is not localized in a specific direction. As in the case of SO_2, 3s orbitals of Cl atoms have not been considered as these are lower in energy. Energy level diagram generated using above symmetries of central atom and LGOs are shown in Fig. 1.6.

Table 1.5: Reducible representation of internal coordinates of $CHCl_3$

C_{3v}	E	$2C_3$ (z)	$3\sigma_v$
Γ_{red} (bonding)	4	1	2

Table 1.6: Reducible representation of lone pairs of $CHCl_3$

C_{3v}	E	$2C_3$ (z)	$3\sigma_v$
Γ_{red} (lone pair)	6	0	0

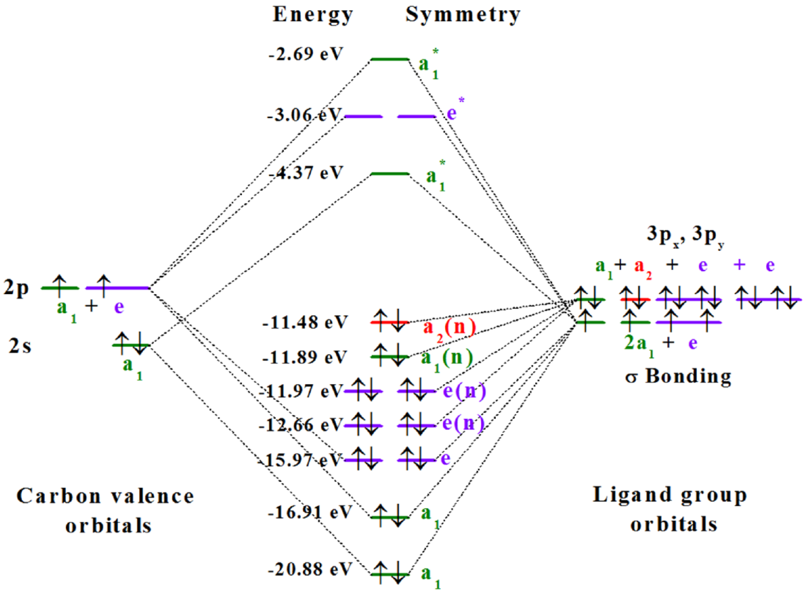

Figure 1.6: Molecular orbital energy diagram of $CHCl_3$. Energy of the orbitals are from the calculation using B3LYP/6-31 G (df)+ taking *IP* (11.48 eV) as zero.

1.5.3. Acetone [$(CH_3)_2CO$]

Acetone contains ten atoms and with appropriate choice for orientation of the two methyl groups, it can be approximated to C_{2v} symmetry (*cf.* Fig. 1.7). First consider the $-CH_3$ group (*cf.* Fig. 1.7a) and construct its MOs under C_{3v} point group as shown in Fig. 1.8.

Figure 1.7: Internal coordinate of a) $-CH_3$ group and b) acetone considering $-CH_3$ as ligand groups.

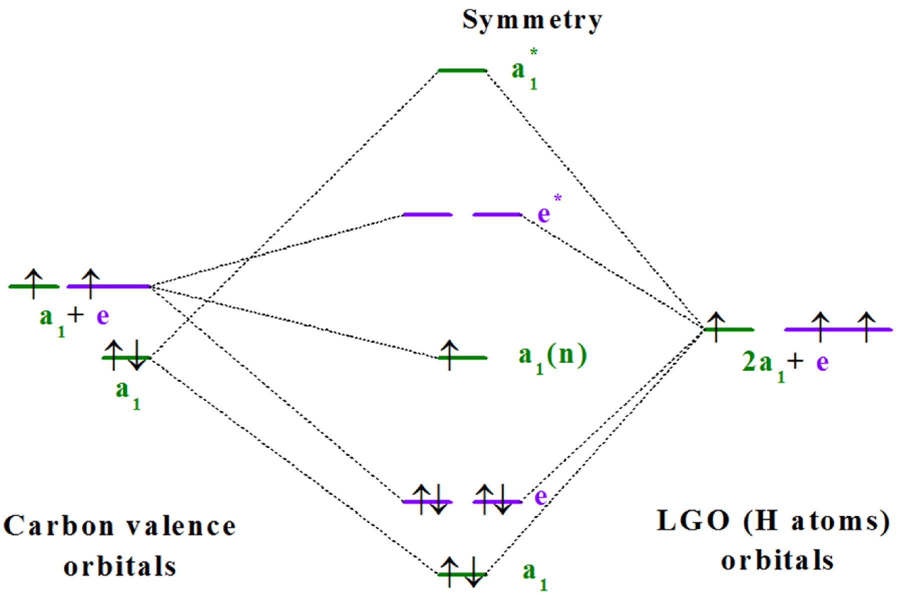

Figure 1.8: molecular orbital diagram of $-CH_3$ subgroup of acetone.

The last unpaired electron occupies a_1 symmetry orbital of $-CH_3$ subgroup. While constructing MOs of acetone, the $-CH_3$ fragments are considered as LGOs (*cf.* Fig. 1.7b) to central carbon atom of acetone. The resultant MOs of acetone are shown in Fig. 1.9.

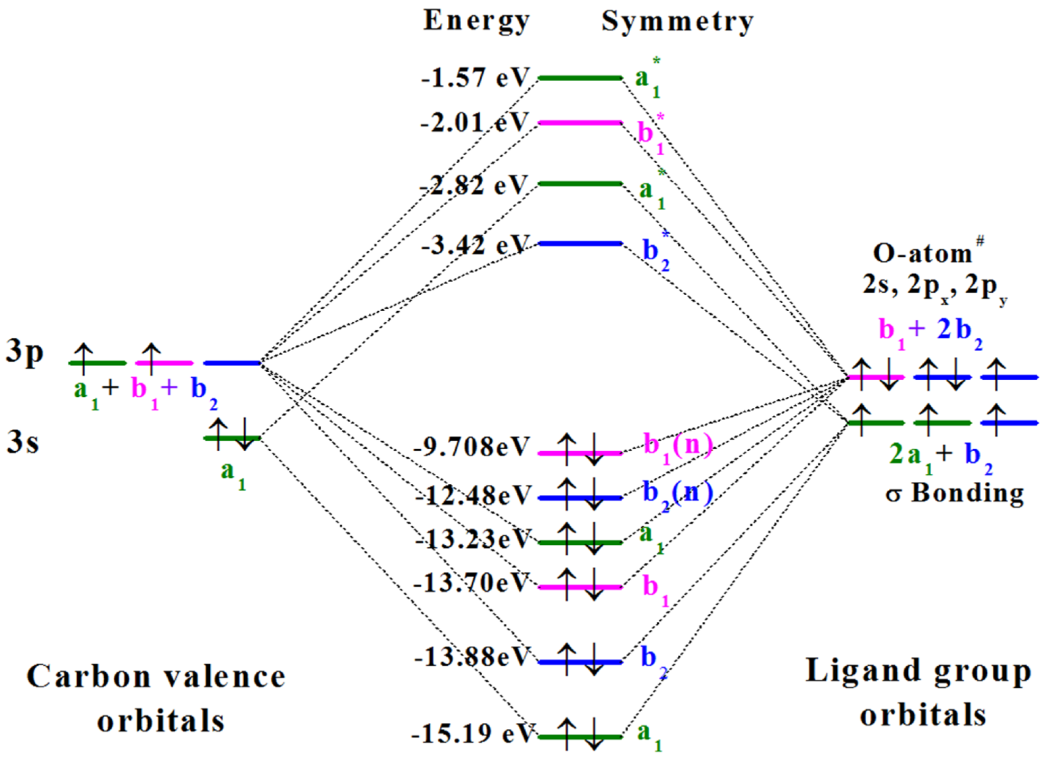

Figure 1.9: Molecular orbital energy diagram of acetone. Energy of the orbitals are from the calculation using B3LYP/6-31 G (2p,2d)+ taking *IP* (9.708 eV) as zero. #include π -electron.

1.6. Plan of the thesis

The studies presented in this thesis are concerned with VUV spectroscopic investigations of electronic states of molecules in gas-phase and in rare gas matrices in the wavelength range 1050–2500 Å (5–11.8 eV, 40,000–95,240 cm^{-1}). Chapter-2 forms the main experimental part of the thesis and is devoted to the design and development of experimental systems for VUV spectroscopy, which includes the HRVUV beamline and experimental stations for photoabsorption and matrix isolation spectroscopy.

In chapter-3, gas phase photoabsorption studies of the $\tilde{E}-\tilde{X}$ system of SO_2 in the 1400–1600 Å (7.7–8.6 eV, 62,500–71,500 cm^{-1}) region using HRVUV beamline is presented. Even though this system is rather well studied in the literature, its vibronic analysis is rather incomplete. The lack of concrete spectroscopic assignments and knowledge of the symmetries of the excited states has motivated detailed investigation of this system. In this chapter, the electronic states involved in the $\tilde{\mathrm{E}}-\tilde{\mathrm{X}}$ system and their symmetries are discussed with the help of vertical excited state calculations. Further, vibronic analysis is carried out with the help of geometry optimization calculations on excited electronic states and possible vibrational modes that are excited are identified. It is concluded that at least three excited electronic states are involved in the $\tilde{\mathrm{E}}-\tilde{\mathrm{X}}$ system viz. $\tilde{X}\,^1\mathrm{A}_1 \rightarrow 3\,^1\mathrm{A}_1, \tilde{X}\,^1\mathrm{A}_1 \rightarrow 2\,^1\mathrm{A}_1$ and $\tilde{X}\,^1\mathrm{A}_1 \rightarrow 2\,^1\mathrm{B}_1$. Out of three vibrational modes of SO_2 *viz.* ν_1' (symmetric stretch), ν_2' (bent) and ν_3' (Asymmetric stretch), the observed vibrational features are mainly due to excitation of the combination modes ($\nu_1' + \nu_2'$) and ($\nu_2' + \nu_3'$) with some contributions from ν_1' and ν_3'. Here ν_1', ν_2' and ν_3' denote the frequencies of symmetric stretch, bending and Asymmetric stretch modes respectively in the excited state.

Chapter-4 presents a detailed work on VUV spectroscopy of acetone-h_6 (CH_3COCH_3) and its deuterated counterpart acetone-d_6 (CD_3COCD_3). Extensive Rydberg series and vibronic features are assigned by taking into account the symmetry selection rules and contributions of hot bands from low lying torsional modes. Assignments are confirmed and consolidated by comparative study of the absorption spectra of acetone-h_6 and acetone-d_6. Revised quantum defect values for the Rydberg transitions and a few new assignments are proposed. The anomalous intensity pattern in the Rydberg transitions observed in acetone-h_6 is attributed to vibronic coupling with nearby valence states of the same symmetry, which is further confirmed using VUV spectrum of acetone-d_6. Issues such as observation of several non-totally symmetric modes, transitions with multiple assignments and location of the ν_{00} origins of the excited states are discussed. This chapter thus provides a unified picture of the VUV spectroscopy of acetone and its deuterated derivative.

Chapter-5 is devoted to the investigation of the electronic spectra of chloroform ($CHCl_3$) and its deuterated counterpart ($CDCl_3$) in the energy region 6.2–11.8 eV (50,000–95,000 cm^{-1}, 1050–2000Å). Identification and analysis of Rydberg series converging to the first four *IP*s at 11.48, 11.91, 12.01 and 12.85 eV corresponding to excitation from the $1a_2$, $4a_1$, $4e$, $3e$ orbitals of $CHCl_3$ respectively are presented. Analysis is aided by quantum chemical computations of excited states. Assignment of vibrational progressions to ν_3' (CCl_3 s–deform) mode and combination modes of ν_3' and ν_6' (CCl_3 d–deform) belonging to $1a_2 \rightarrow 4p$ transition is confirmed based on study of vibronic spectrum of $CDCl_3$. This chapter thus presents a consolidated analysis of the VUV photoabsorption spectrum of chloroform.

In Chapter-6, VUV spectroscopy of molecules isolated in inert gas matrices at cryogenic temperatures is presented. In order to highlight the differences in the spectra in gas phase and matrix isolated phase, VUV spectra of SO_2 and acetone are discussed. Electronic transitions observed in matrix isolated acetone show blue shifts of ~3000–6000 cm^{-1}, as expected for the Rydberg transitions. In the case of SO_2, the first three absorption bands are not shifted much in the matrix phase as compared to the gas phase, whereas the higher excited states show larger shifts. This is in line with the assignment of the first three gas phase absorption systems to valence transitions, and higher bands to transitions of valence-Rydberg mixed or Rydberg character.

Finally the important conclusions of the present studies and future directions of work are discussed in Chapter-7.

Chapter-2

Experimental

Indus-1 synchrotron [22, 23] at Raja Ramanna Centre for Advanced Technology, Indore, India provides a useful platform for studies in VUV spectroscopy of molecules in gas phase as well as in the matrix isolated phase. Indus-1 is a 450 MeV storage ring with a typical photon flux of 7.2 x 10^{11} photons/sec/mrad/0.1% bandwidth at critical wavelength of 61 Å. Two beamlines, namely the photophysics (PPS) beamline and high resolution ultraviolet (HRVUV) beamline, are extensively used for the VUV spectroscopy work reported here. Of these, the HRVUV beamline is designed and developed as a part of the work related to the present thesis. For VUV spectroscopy of molecules in gas phase and matrix isolated phase, dedicated workstations are developed. The experimental set-ups are optimized and calibrated. This chapter discusses the design, development and optimization of the HRVUV beamline and other experimental workstations, and the protocols developed for their effective use. This chapter thus forms the main stay of the experimental work reported in the subsequent chapters.

2.1 Design and development of HRVUV beamline

HRVUV beamline is developed using a 6.65 meter off-plane Eagle spectrometer and installed at the bending magnet port, BL-1 of Indus-1.This beamline is useful for photo absorption studies of atoms and molecules in the wavelength range of 1150–3000 Å. at an average resolution of 0.1 Å. The performance of the beamline is found to be comparable with beamlines operational at several storage rings around the world [40, 41].

2.1.1 Beam line description

The complete mechanical layout of the HRVUV beamline consisting of the front end, the focusing system, the absorption cell and the VUV spectrometer is shown in Fig. 2.1. The beamline essentially consists of three parts; i) focusing optics, ii) 6.65 m Spectrometer and iii) photoabsorption setup.

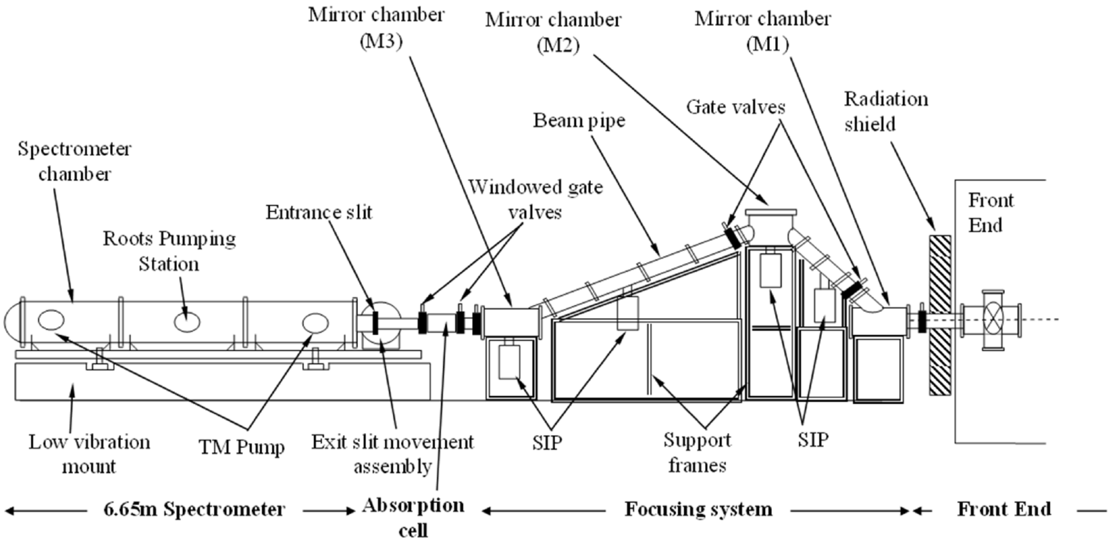

Figure 2.1: Mechanical layout of HRVUV beamline

2.1.1.1 Optical layout

The optical layout of the beamline is illustrated in Fig. 2.2. Here the SR, emanating from the tangent point (S1) and focused by a three mirror system M1, M2 and M3 (*cf.* Fig. 2.2), passes through a sample cell and falls on the entrance slit (S2) of a 6.65 m off plane Eagle mount spectrometer. This spectrometer is widely used in VUV beamlines due to its proven high resolution capability in this wavelength region [42]. The choice of the pre-dispersing optical system is such that it maximizes the throughput in the VUV region, and effectively matches the source aperture to the spectrometer aperture within the constraints imposed by the source, space availability and cost. Various types of pre-optics have been used in similar beamlines around the world. The optical layout chosen for the present beamline is very similar to that used in the high resolution beamline at SURF II [43].

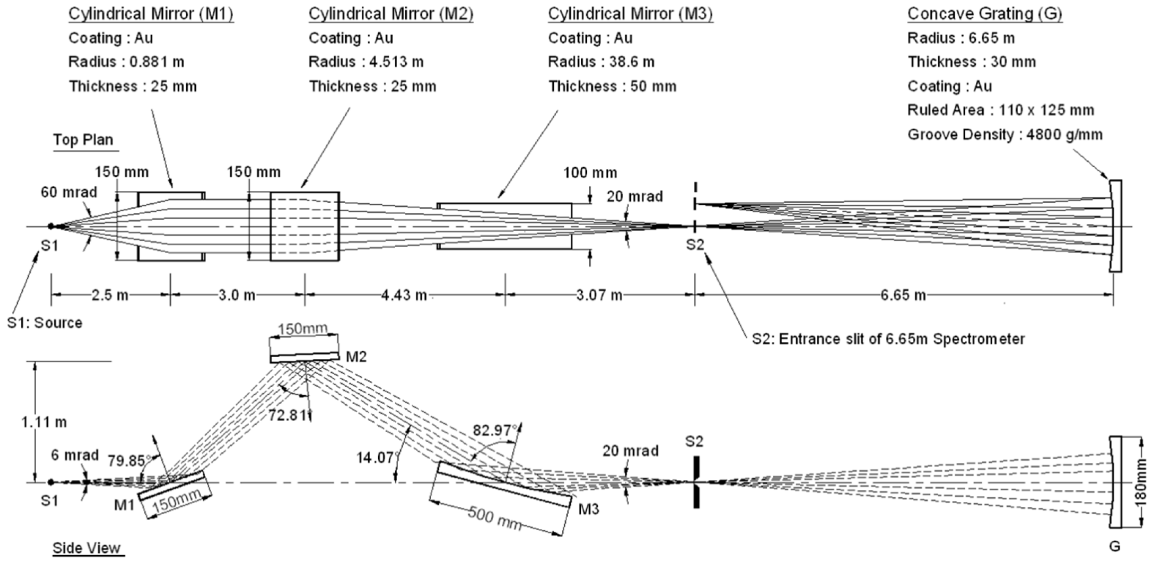

Figure 2.2: optical layout of the HRVUV beamline

The vertical and horizontal acceptance angles of the beamline are 6 and 60 mrad respectively. The designed acceptance angles of the spectrometer for the entrance beam are 20 mrad × 20 mrad. It is therefore necessary to expand the SR beam by a factor ~3.3 in the vertical direction and compress by a factor 3 in the horizontal direction to ensure full illumination of the grating. This is achieved by the focusing system consisting of three concave cylindrical mirrors (M1, M2 and M3) as shown in Fig. 2.2. The cylindrical axes of M1 and M2 lie in the vertical plane, whereas the axis of M3 lies in the horizontal plane. M1 collimates the SR beam in the horizontal direction and acts as a plane mirror in the vertical direction. M2 focuses the collimated beam in the horizontal direction onto the entrance slit S2 and acts as a plane mirror in the vertical plane. M3 focuses the vertical component of SR and acts as a plane mirror in the horizontal plane. The focal length (*f*) of M1 and M2 in the sagittal plane are calculated using the relation,

$$f = \frac{r}{2\cos\theta}, \tag{2.1}$$

where r is the radius of curvature and θ is the angle of incidence. For θ=79.85° in the vertical plane f= 2.7 m for M1, which is the distance from S1 to the midpoint of M1. Eq.(2.1) also gives the focal length of M2 as 7.6 m. If the object distance from S1 to the center of M3 is l_1 and image distance in the tangential plane (the distance of the slit S2 from the mirror M3) is l_2, then the radius of curvature r and the angle of incidence θ are related by

$$\frac{1}{l_1}+\frac{1}{l_2}=\frac{2}{r\cos\theta}, \tag{2.2}$$

which gives r = 38.6 m for θ = 82.97°. The optimized values of radii of curvature and angles of incidence for all three mirrors are given in Table 2.1.

Table 2.1: Parameters of the mirrors Parameters of the mirrors

Cylindrical mirror	Dimensions (mm x mm x mm)	Radius of curvature (m)	Focal length f (m)	Angle of incidence θ (°)	Reflective Coating
M1	150 × 150 × 25	0.881	2.7	79.85	Gold
M2	150 × 150 × 25	4.513	7.6	72.81	Gold
M3	100 × 500 × 50	38.6	3.07	82.97	Gold

The three mirror system thus transforms the SR beam of 60 mrad (H) × 6 mrad (V) to a focused beam of 20 mrad × 20 mrad. The final image on S2 is 10 mm (H) × 1.0 mm (V), in agreement with the results of ray tracing calculations [44, 45]. Note here that M1, M2, M3 along with their mounts, which provide six degrees of freedom for alignment, are placed in separate mirror chambers, maintained at ~10^{-9} mbar vacuum (*cf.* Fig. 2.1). This optical system, consisting of three cylindrical mirrors with their axes orthogonal to each other, gives the desired horizontal and vertical magnifications with relatively simple and inexpensive optical elements. The rather high angles of incidence (~72°–82°) are chosen to obtain a high reflectivity in VUV region. Further, this configuration enhances the degree of polarization of SR perpendicular to the plane of incidence. The efficiency of gold coated mirrors in achieving a good combination of polarization enhancement and high throughput in the wavelength region 500–2000 Å has been demonstrated by the comparative study by Ginter and Brown [41].

2.1.1.2 6.65 m spectrometer

A schematic diagram of the optical arrangement of the spectrometer is shown in Fig. 2.3. The spectrometer is based on off-plane Eagle mounting utilizing a concave spherical grating of radius of curvature 6.65 m. Depending on the desired wavelength region and resolution, two gratings can be interchangeably mounted. The major parameters of the two gratings are given in Table 2.2.

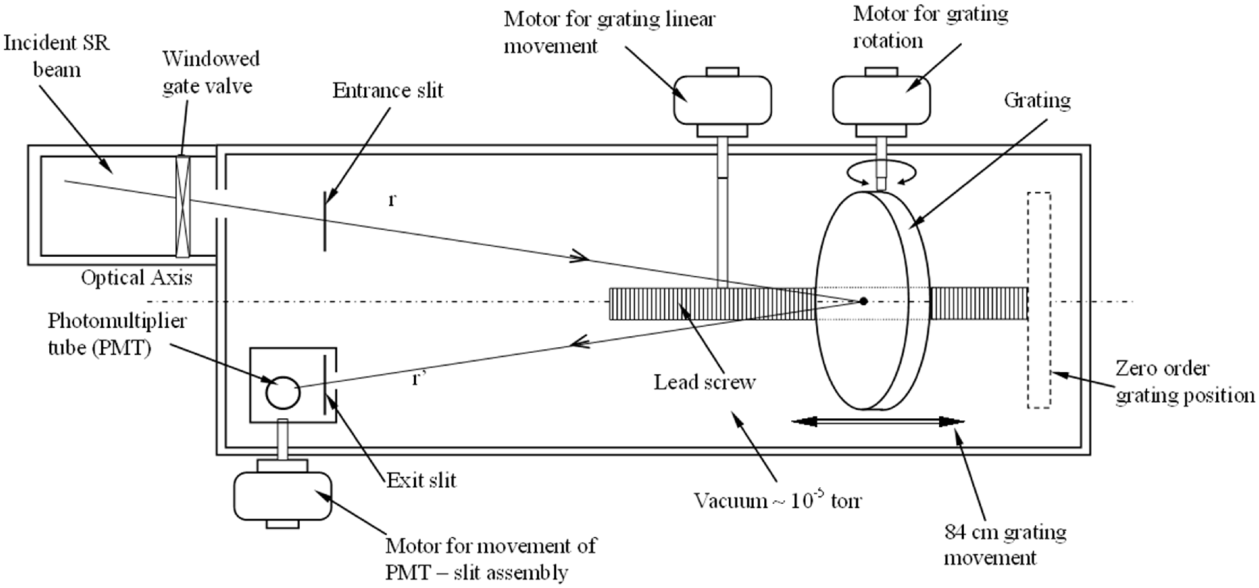

Figure 2.3: Schematic diagram showing of the 6.65m off-plane spectrometer

Table 2.2: Parameters of the gratings

Ruling	4800 l/mm	1200 l/mm
Coating	Gold	Al + MgF_2
Diameter of blank	180 mm	210 mm
Ruled area	125 mm x 110 mm	125 mm x 110
Blaze angle	13º 52'	5º 10'
Blaze wavelength	1000 Å	1500 Å
Linear dispersion	0.3 Å/mm	1.24 Å/mm
Wavelength coverage	500-2000 Å (6-25 eV)	1200-6000 Å (2-10 eV)
PMT Scanning Range	50 Å	200 Å

For zero wavelength setting i.e. zeroth order diffraction of the grating, the distance between the entrance slit and the concave grating is 6.65 m, whereas that between the entrance and exit slits is 16.8 cm in the horizontal plane. The grating equation for selecting a particular central wavelength is

$$\sin\alpha_0 + \sin\beta_0 = \frac{\lambda_0}{d}, \tag{2.3}$$

where $1/d$ is line density of the grating, α_0 is the incident angle and β_0 is the angle of diffraction corresponding to central wavelength λ_0. These angles are defined in the plane containing the entrance slit and the centre of curvature of the grating at zero order. The angle α_0 and grating translation (X, measured from the zero wavelength position) along the axis of grating are related by

$$\cos\alpha_0 = 1 - \frac{X}{R}, \tag{2.4}$$

where R is radius of curvature of the concave grating. Since $\alpha_0=\beta_0$ for the central wavelength λ_0, Eq. (2.3) takes a simplified form,

$$2\sin\alpha_0 = \frac{\lambda_0}{d}. \tag{2.5}$$

The reciprocal linear dispersion is given by

$$\frac{d\lambda}{dl} = \frac{d\cos\beta_0}{R} \times 10^4 \text{ Å/mm}, \tag{2.6}$$

where R is expressed in meter and $1/d$ is the number of lines per millimeter. For selecting a particular wavelength, the grating is rotated about the horizontal axis that passes through its pole and is parallel to the entrance and exit slits. It is then translated along the axis of the spectrometer in order to focus the dispersed wavelength on the Rowland circle. The values of grating rotation and displacement for wavelength λ_0 are calculated from Eq. (2.5) and (2.4) respectively.

The spectrum is scanned by moving the exit slit and photomultiplier (PMT) assembly vertically along the focal plane. The maximum displacement of the exit slit and PMT assembly along the vertical focal plane is 160 mm thereby giving a scanning range of 200 Å for the 1200 l/mm grating and 50 Å for the 4800 l/mm grating. The linear and rotational motion of the grating and the linear motion of PMT are controlled by a 3-axis stepper motor controller and driver system. A sodium salicylate coated quartz window mounted at the exit slit of the spectrometer converts the VUV radiation into visible radiation [46], which is then detected by a PMT (R 300, Hamamatsu make). A microcontroller based data acquisition system comprising of two channels of current to frequency converters digitizes the PMT signal and the synchrotron beam current signal. A Visual BASIC programme on a host computer acts as the interface between the user and data acquisition system. The programme obtains and updates the accurate position of the PMT by reading the digital readout coupled to a linear scale. This scale is driven by the linear actuator which governs the PMT movement. Counts corresponding to the PMT signal and the SR beam current signal are acquired at every step of PMT movement for a set integration time and sent to the host program for online plotting.

2.1.1.3 Experimental setup

Fig. 2.4 shows the schematic diagram of an absorption cell and sample filling system designed for gas phase photoabsorption studies. The cell is a cylindrical stainless steel chamber of 60 mm diameter and 830 mm length and is provided with ports for the purpose of sample introduction and pressure measurement. Provision is kept for introducing up to three gaseous samples at different pressures. Here one gas, typically Xe or O_2, is used for calibration of the VUV spectrum. The cell is evacuated to a base pressure of 10^{-6} mbar using turbo molecular pump (TMP) and filled with the gas sample under investigation. The gas flow is controlled with a needle valve and the pressure is measured with the help of a capacitance gauge. Liquid samples are introduced by the usual freeze-pump thaw technique.

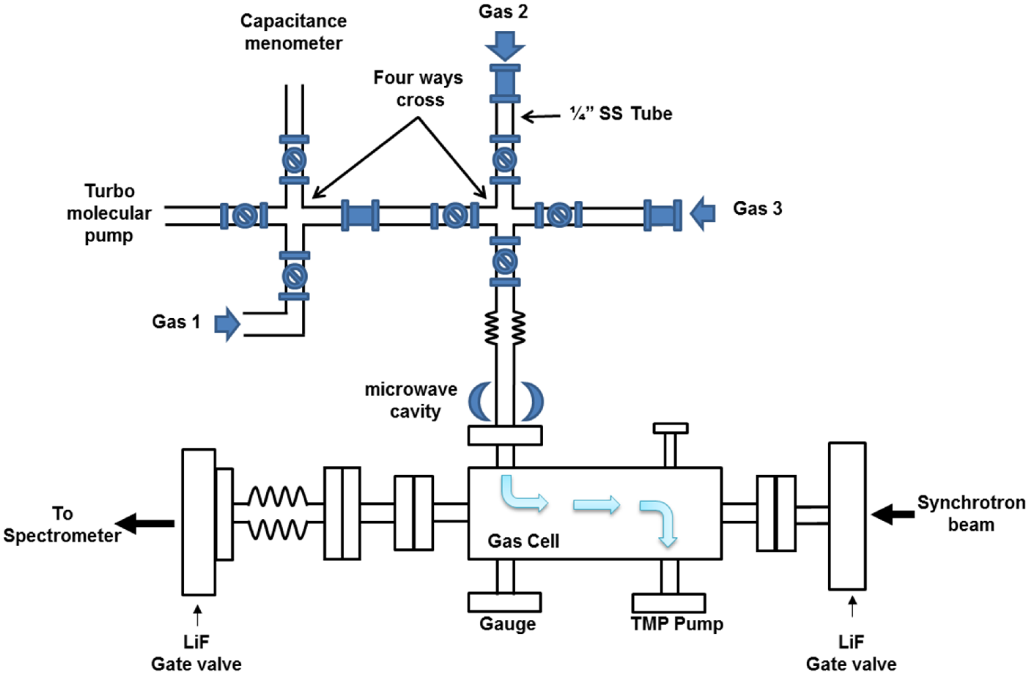

Figure 2.4: Schematic diagram showing the mechanical arrangement of the gas absorption cell and sample filling system

2.1.2 Optical alignment

2.1.2.1 Beamline

The alignment of the beamline starts with the determination of the optical axis of the SR coming out from the windowed exit-port of the front-end. The collimating mirror chamber, horizontal focusing mirror chamber and vertical focusing mirror chamber are then placed at their respective pre-determined positions (*cf.* Fig. 2.1). All mirrors are then aligned with respect to the visible SR to get the best focused image on a screen placed at the position of the entrance slit (S2). The observed spot size is found to be 10 mm (H) x 1 mm(V), which matches closely with the targeted design value. A second screen is placed at the zero order position of the 6.65 m spectrometer to optimize the filling area of the grating.

2.1.2.2 Spectrometer

Initial alignment of the spectrometer is carried out using a green He-Ne laser (5435 Å). The spectrometer is calibrated with respect to the 1200 l/mm grating using standard emission lines from a Hg discharge lamp. The performance of the spectrometer in VUV region is tested and calibrated using the fourth positive band system of CO from an electrodeless discharge tube. Atomic emission lines, e.g. 1930 Å of atomic carbon, are used to check the reproducibility of the system. The pre-focusing optics, the absorption cell and the spectrometer are then integrated with the SR source. Windowed gate valves are used to isolate the cell from the third mirror chamber as well as from the spectrometer.

2.1.3 Performance testing

Photoabsorption studies using the HRVUV beamline are carried out with the 1200 l/mm grating. The Al coating of this grating together with its blaze at 1500 Å gives a much better signal intensity at the exit slit in the 1150–3000 Å region as compared to the high density gold coated grating blazed at 1000 Å. The spectra are normalized at each data point with respect to the beam current.

2.1.3.1 Resolution and reproducibility

The atomic absorption line of xenon at 1469.61 Å (68,045 cm^{-1}) corresponding to the transition $5p^6$ (^1S)–$5p^5$ ($^2P^o_{3/2}$) 6s $^2[3/2]^o_1$ is used to ascertain the resolution and reproducibility of the spectrometer. To this end, the grating is set at α_0=5.0587° and X=25.903 mm to get a sharp focus at the exit slit (*cf.* Eqs. (2.4) and (2.5)). The VUV absorption spectrum of xenon is recorded at several pressures and slit widths by scanning the PMT–cum–exit slit assembly along the Rowland circle. Parameters like motor speed and acquisition time are adjusted to optimize the quality of the spectra. A typical recorded spectrum is shown in Fig. 2.5. The wavelength reproducibility is found to be within ±

0.01Å and the full width at half maximum (FWHM) of the line is observed 0.116 Å; the later demonstrates the resolution of the instrument. The Xe line at 1469.61 Å is also used for calibration of the PMT position. The beamline performance is further corroborated by recording VUV absorption spectra of O_2 and SO_2.

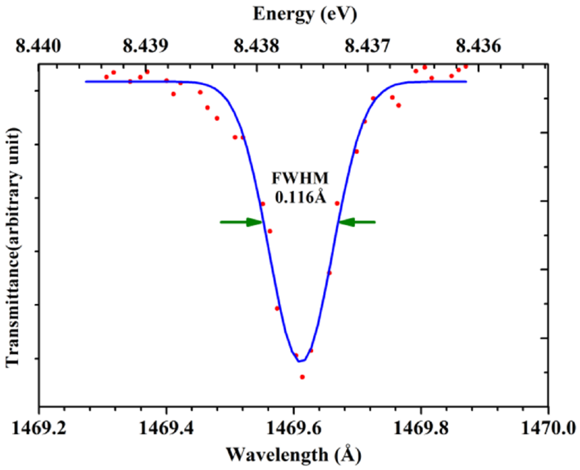

Figure 2.5: Absorption spectrum of 1469.61Å line of xenon recorded on HRVUV beamline using Indus-1 synchrotron radiation source.

2.1.3.2 Absorption spectrum of O_2

The Schumann-Rungé system ($X\,^3\Sigma_g^- \rightarrow \tilde{B}\,^3\Sigma_u^-$) is the most extensive band system of O_2 spanning a range right from the VUV region (~1250 Å) to the visible (~5800 Å) and has been studied thoroughly in emission and absorption [47, 48]. In the VUV region, the absorption spectrum consists of a continuous absorption in the 1250–1750 Å region followed by a band system in the 1750–2000 Å region. This well-studied system is often used as a benchmark to test the performance of VUV spectrometers. In the present work, the Schumann Rungé system of O_2 is recorded at several pressures in the wavelength region 1780–1880 Å. A typical spectrum obtained using the 1200 l/mm grating is shown in Fig. 2.6. The observed bands are single headed and strongly degraded to the red in agreement with previous studies [49]. The vibrational numbers corresponding to the upper and lower electronic states are marked in parenthesis in the figure. Assignment of vibronic transitions is carried out on the basis of the available literature on the Schumann-Rungé system of oxygen [49].

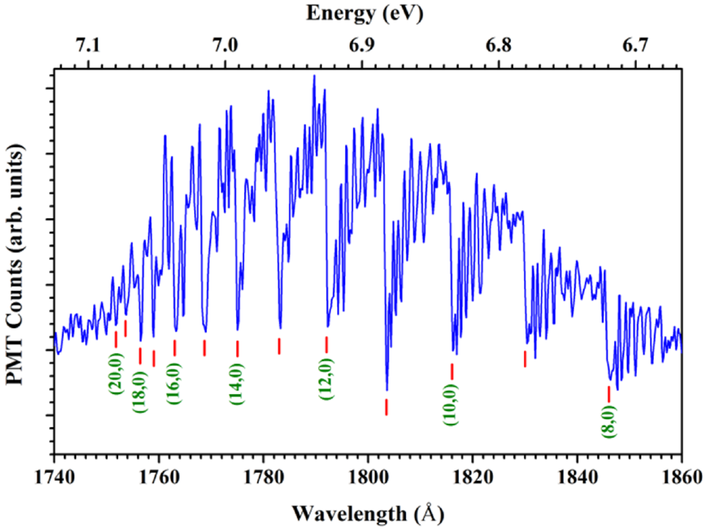

Figure 2.6: Absorption spectrum of oxygen showing Schumann-Rungé system in the wavelength range of 1740-1860 Å. Sample pressure 1.0 mbar. The bracketed entries are upper and lower vibrational numbers.

2.1.3.3 Absorption spectrum of SO_2

VUV absorption spectrum of SO_2 is recorded in the region 1700–2350 Å (5.3–7.3 eV), corresponding to $\tilde{X}^1A_1 \rightarrow \tilde{C}^1B_2$ band system which has been studied by several workers [25, 50-53]. A part of this system in the region from 2160-2340 Å is shown in Fig. 2.7. Observed absorption features are assigned on the basis of earlier reported work [52, 53]. The convention followed is (aν_1, bν_1, cν_1); where a, b and c are the number of quanta of vibrational energy in the excited electronic state. The observed spectrum compares very well with previously published literature.

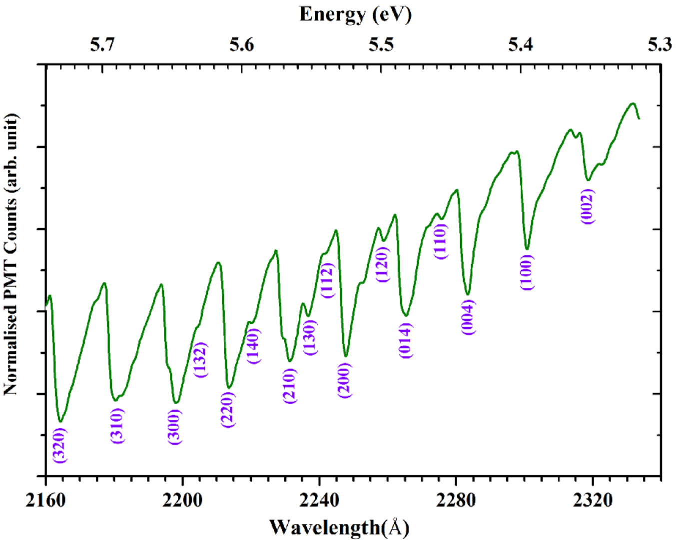

Figure 2.7: Absorption spectra of $\tilde{X}^1A_1 \rightarrow \tilde{C}^1B_2$ system of SO_2 in the wavelength range of 2160 Å–2340 Å. The bracketed entries are vibrational quantum numbers of upper electronic states.

2.1.4 Comparison with beamlines around the world

It is worthwhile to compare here the HRVUV beamline on INDUS-1 with high resolution (resolving power $\geq 10^4$) VUV beamlines (5–25 eV) on the other synchrotron sources. The SURF II facility at NIST [41] and the VOPE facility at photon factory [43] are very similar to the HRVUV beamline in terms of design and applications. However, both these facilities have been decommissioned. More recently, several new high resolution VUV beamlines with novel designs, installed on bending magnets or undulators have come up. Beamlines based on bending magnet include the DISCO beamline on SOLEIL [54], Dragon-like beamline at NSRRC [55], and normal incidence beamline at the Pohang light source [56]. The DISCO beamline uses a multi-mirror pre-focusing system to transport the beam to three different end stations and uses commercially available monochromators. The beamline at NSRRC employs a unique 6 m cylindrical grating monochromator with four interchangeable gratings to cover the 5–40 eV energy range.

VUV beamlines exploiting the extraordinary properties of undulators include, the SU5 beamline at the super-ACO ring [57], DESIRS high resolution and variable polarization beamline at SOLEIL with VUV FTS and an electron/ion imaging coincidence spectrometer [58], the chemical dynamics beamline at the ALS [59], the SAMRAI beamline at UVSOR-II [60], beamline with circularly polarized VUV light at the HiSOR storage ring [61] and the U9-CGM beamline at NSRRC [62]. Among these SU5 and the chemical dynamics beamline use 6.65 m off-plane Eagle monochromator, SAMRAI employs 10 m Wadsworth monochromator and provides a beam with variable polarization, the beamline on HiSOR uses 3 m off-plane Eagle monochromator and U9-CGM utilizes 6 m cylindrical grating monochromator.

Best resolving power reported so far in 5–25 eV region is 2.5×10^5, achieved with a 6.65 meter spectrometer or monochromator with a 4800 l/mm grating [40]. In comparison the resolving power achieved in the HRVUV beamline with a 1200 l/mm grating is ~1×10^4 at 1469 Å (8.44 eV) , which can be improved by a factor of four by use of a 4800 l/mm grating. Estimated photon flux at sample position in HRVUV beamline is ~10^8–10^9 photons/s, which is a reasonable value for a beamline at bending magnet. These results demonstrate the utility of the HRVUV beamline for high resolution spectroscopy of atoms, molecules and clusters in VUV region.

2.2. Photophysics beamline

The PPS beamline is a medium resolution facility which uses a 1 meter Seya-Namioka monochromator for wavelength selection in the range of 500–3000 Å (4–25 eV). A toroidal mirror focuses the SR from the Indus-1 storage ring onto the entrance slit of the monochromator [63] .The monochromatized SR is focused at the sample position by a post focusing toroidal mirror. The resolution achieved is about 1.5Å (4 meV at 4eV and 10 meV at 10 eV) with 2400 l/mm grating [63]. The gas phase absorption cell is a SS six-way cross of length 250 mm, placed after the exit slit. The cell is pumped to a base pressure ~10^{-6} mbar using a TMP. Samples are introduced into the gas cell by freeze-pump-thaw technique and then allowing them to fill the gas cell in a controlled manner to a required pressure. The sample pressure in the gas cell is monitored by a capacitance gauge. A VUV-visible sensitive photomultiplier coupled with a sodium salicylate coated window is used for the detection of light. The light intensity is normalized with respect to the storage ring current. All parameters such as wavelength, intensity of synchrotron light, sample pressure and the beam current are monitored at every step of 0.5Å and data is acquired on a data acquisition system coupled to a personal computer. Absorption spectrum is generated by plotting $\ln(I_0/I)$ v/s wavelength from the Beer-Lambert law, $I=I_0\exp(-n\sigma_\lambda L)$, where I and I_0 are transmitted intensities with and without samples, n is number density, σ_λ is wavelength dependent cross section and L is path length. Calibration is done by recording atomic lines of Kr and Xe in VUV region.

2.3. Development of matrix isolation spectroscopy setup

MIS is a well-established technique where the sample of interest is mixed with large excess of inert gas at very low temperature [9-17, 19-21, 64-69]. In order to exploit the dual advantages of SR as a VUV source and the MIS technique, an experimental station is designed and developed at photophysics beamline. Here the details of the design, development, integration and performance testing MIS set-up are discussed.

2.3.1 MIS setup

The MIS setup consists of a closed loop helium-cryostat, chiller unit, experimental chamber, sample mixing chamber, vacuum instrumentation, temperature sensor and interconnecting gas lines to prepare sample mixtures with inert gases. A schematic of the experimental setup is shown in Fig. 2.8a and b. A photograph of the MIS after integration with the PPS beamline is shown in Fig. 2.8c.

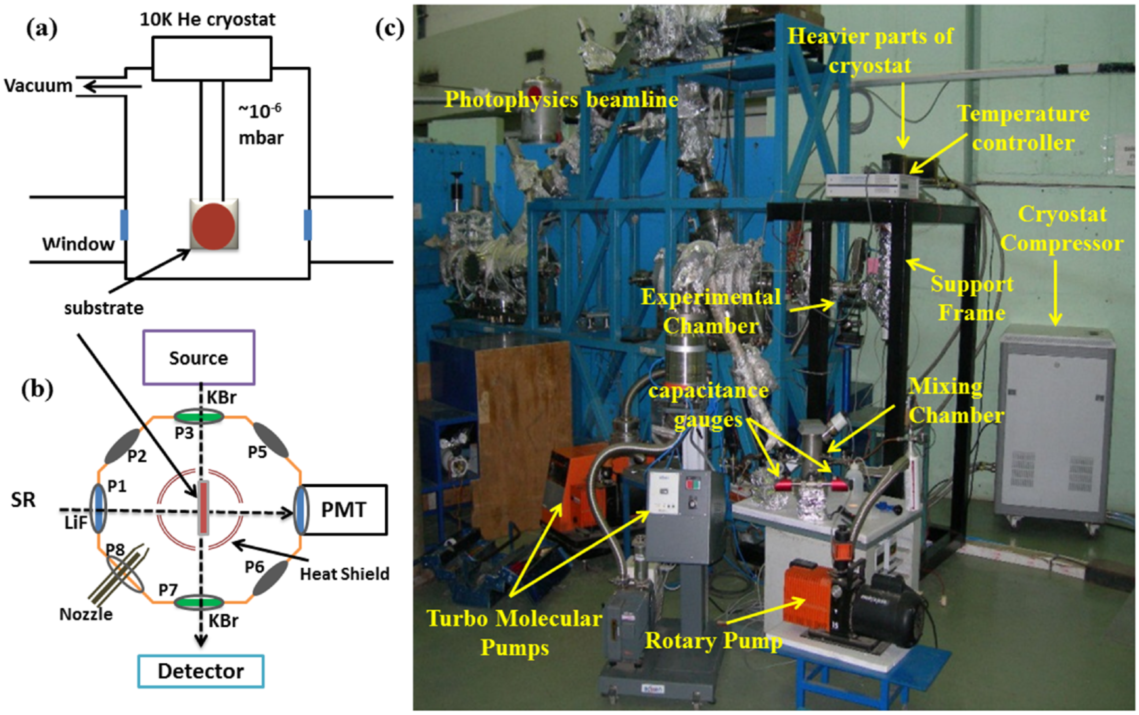

Figure 2.8: Block diagram of (a) cryostat and (b) experimental chamber of MIS system. P1–P8 are ports of octagonal chamber. (c) MIS setup after integration with PPS beamline.

2.3.1.1 Liquid helium cryostat

In order to prepare rare gas matrices, gaseous flux is directed towards a cold window kept in a cryostat at low temperatures (~10 K). There are two common methods using helium as the coolant form for achieving such low temperatures, *viz*. flow type cryostat and closed cycle refrigerator (CCR). A CCR type of cryostat developed in-house at the Cryogenics Section, RRCAT is used in the present experimental station owing to its ease of operation, maintenance and low running cost [11]. Cooling is achieved inside the cryostat by isentropic expansion of helium gas. The cryostat consists of a helium compressor, cold head, chiller unit and temperature measurement sensors. The pressure inside the cryostat chamber is maintained at $\sim 10^{-6}$ mbar by a TMP and is measured using an ionization gauge. The CCR is connected with the other heavier parts i.e. generator, Cu mesh etc. mounted on top of the support frame structure as shown in Fig. 2.8c. A sample holder made of oxygen free high conductivity copper for holding a one inch diameter substrate is connected to the cryostat. The cryo-cooler has a heat shield around the cold head with four openings at 90°.

2.3.1.2 Experimental and mixing chambers

The experimental chamber is an octagonal stainless steel chamber with eight ports (P1 to P8) as shown in Fig. 2.9a. Two additional ports (P9 and P10) are provided for connecting the chamber to the cryostat and for pumping. Ports P1 and P5 are used for entry and exit of the SR. Port P2 at 45° to the SR-entry is used for connecting the nozzle for sample deposition. Ports P3 and P7 are kept for FTIR spectroscopic studies. The remaining ports (P4, P6 and P8) are available for sample thickness measurements and/or for up-gradation of the experimental facility by adding additional characterization techniques in future.

The mixing chamber is a stainless steel cylindrical container with six ¼″ tube connectors (*cf.* Fig. 2.9b) which are used for different functions like pumping, pressure measurement, inlet of gases/gas mixtures and connection to the experimental chamber for deposition. The sample chamber is evacuated to a base pressure of ~1×10^{-6} mbar using a TMP. The sample gas is mixed with high purity argon (99.995%) in the mixing chamber at appropriate manometric ratios, typically 1: 1000–1:100, using a set of two capacitance manometers. A calibrated needle valve is used to deposit the gas mixture in a controlled manner at ~1 mbar/min. The needle valve is connected to 200 µm deposition nozzle located at a distance of 10 mm from the heat shield of the cryo-tip. All connectors are of SS ¼″ ferrule type and all-metal Swagelok shut-off valves are used for isolation of the chamber from the pumps, gauges and sample inlets.

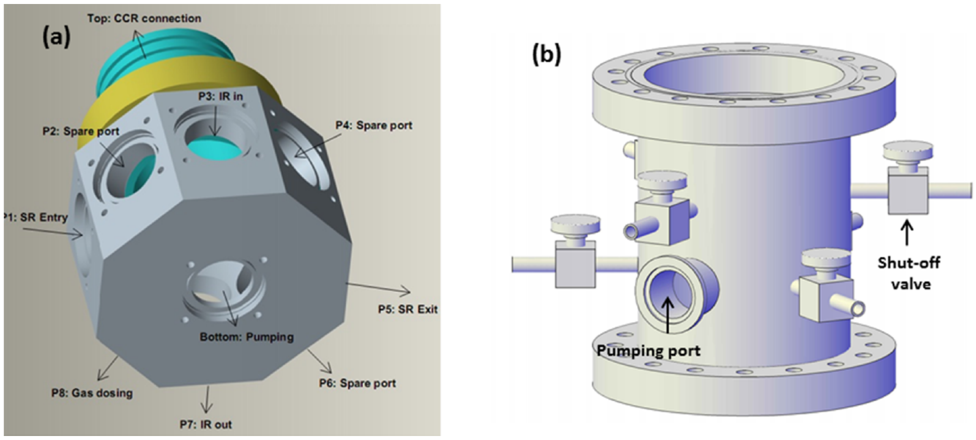

Figure 2.9: (a) Experimental chamber with all ports and (b) Mixing chamber.

2.3.2 Testing of components

The various subsystems such as experimental chamber, mixing chamber, vacuum systems, gas lines and nozzle, leak valves, temperature sensor, capacitance manometers, etc. are tested individually and assembled. Mechanical stability tests of the sample holder, temperature calibration and measurement are performed before connecting to the beamline. Vibration measurements are carried out to evaluate the effect of vibrations produced by the compressor on the sample holder. They are found to be within ± 250µ (±60µ) in the horizontal (vertical) direction and are much smaller than the typical defocused spot size 8mm(H) X 6mm(V) used in the photoabsorption experiments.

The temperature of the sample in the cryostat is monitored with a silicon sensor (Si470) placed at the bottom of the sample holder, which is calibrated at room, liquid N_2 and liquid He temperatures. A resistively heating arrangement using kapton coated nichrome wire is provided to anneal the sample from 10 K to 300 K in-situ. Temperature of the sample holder is measured during cooling and heating cycles as shown in Fig. 2.10a. It takes approximately 1.5 hours to reach 10 K. At the base pressure of 2×10^{-6} mbar, the gases present in the chamber at room temperature are predominantly H_2O, H_2, CO, CO_2, N_2 and O_2. On lowering the temperature, these gas molecules get adsorbed at various low temperature locations. Below 85 K, the cooling rate starts to increase owing to the faster rate of adsorption for N_2 and O_2. At ~30 K all the other gases start to get adsorbed faster thereby effectively increasing the rate of cooling (*cf.* inset of Fig. 2.10a). Below 15 K the cooling rate becomes slower due to the decrease in the difference between desorption and adsorption of molecules, and that governs the ultimate temperature of the cryostat. In the present case, the final achieved temperature is 10 K. Fig. 2.10a also shows the behaviour of the temperature of the sample holder after the cryostat of put off. To obtain a desired temperature (10-300 K), the sample holder is heated in a controlled manner; a typical time profile is shown in Fig.2.10b.

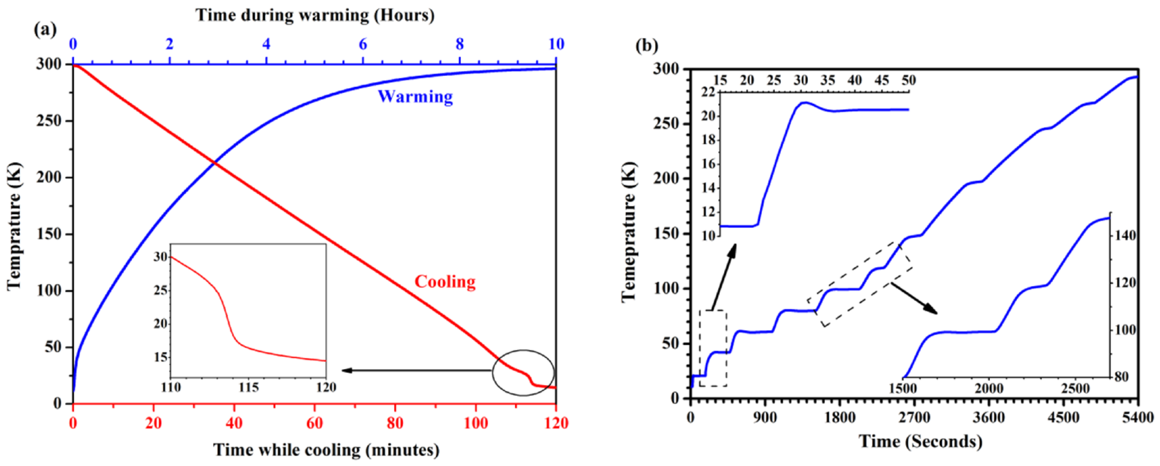

Figure 2.10: (a) Temperature profile during cooling and warming cycles. A sharp fall below 25 K is shown in the inset. (b) Response of cryostat during heating cycles. Insets show magnified view of temperature jump during heating.

2.3.3 Off-line experiments on oxygen ice

The performance of the MIS setup is tested by depositing oxygen at 11 K on a quartz substrate and measuring the UV-visible absorption spectrum of oxygen ice. Temperature dependent optical absorption spectra of oxygen ices from 11 K to 70 K are recorded using a tungsten lamp source and a CCD based spectrograph and shown in Fig. 2.11. Oxygen films in α–phase (monoclinic) and β–phases (trigonal) are prepared by depositing molecular oxygen on to a quartz substrate attached to the sample holder at 11 K and 25 K respectively [70]. A flow rate ~1mbar/min is maintained during deposition using a 200μ nozzle at 10 mm distance from the heat shield. Films are annealed from the deposition temperature up to 70 K at different temperatures in intervals of 5 K. The corresponding band positions for the two phases are given in Tables 2.3 and 2.4. The observed spectra are in very good agreement with the reported literature in respect of the band positions and shapes [68, 71].

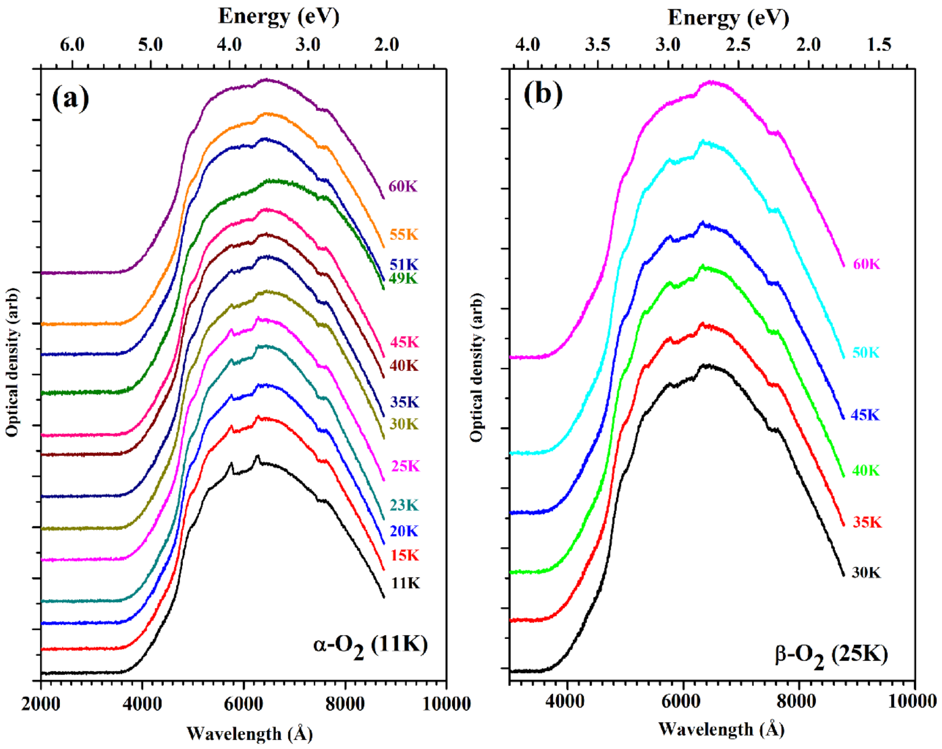

Figure 2.11: Temperature dependent absorption spectrum of oxygen ice in (a) α-phase and (b) β-phase.

Table 2.3: The absorption bands of α–oxygen

Assignment	Band system	Observed peaks (Å)		
		Present studies	Ref [68]	Ref [71]
(0,0)	$^1\Sigma_g^+ \leftarrow {}^3\Sigma_g^-$	7621	7598	--
(0,0)	$^1\Sigma_g^+ \leftarrow {}^3\Sigma_g^-$	7566	7565	7564
(0,0)	$^1\Sigma_g^+ \leftarrow {}^3\Sigma_g^-$	7491	7514	--
(1,0)	$^1\Sigma_g^+ \leftarrow {}^3\Sigma_g^-$	6844	6841	--
(0,0)	$^1\Delta_g + {}^1\Delta_g \leftarrow {}^3\Sigma_g^- + {}^3\Sigma_g^-$	6291	6298	--
(0,0)	$^1\Delta_g + {}^1\Delta_g \leftarrow {}^3\Sigma_g^- + {}^3\Sigma_g^-$	6264	6272	6271
(1,0)	$^1\Delta_g + {}^1\Delta_g \leftarrow {}^3\Sigma_g^- + {}^3\Sigma_g^-$	5756	5764	5763
(2,0)	$^1\Delta_g + {}^1\Delta_g \leftarrow {}^3\Sigma_g^- + {}^3\Sigma_g^-$	5311	5318	5317
(3,0)	$^1\Delta_g + {}^1\Delta_g \leftarrow {}^3\Sigma_g^- + {}^3\Sigma_g^- -$	4920	4943	4942

Table 2.4: The absorption bands of β–oxygen

Assignment	Band system	Observed peaks (Å)		
		Present studies	Ref [68]	Ref [71]
(0,0)	$^1\Delta_g + {}^1\Delta_g \leftarrow {}^3\Sigma_g^- + {}^3\Sigma_g^-$	6287	6282	6281
(1,0)	$^1\Delta_g + {}^1\Delta_g \leftarrow {}^3\Sigma_g^- + {}^3\Sigma_g^-$	5756	5774	5774
(2,0)	$^1\Delta_g + {}^1\Delta_g \leftarrow {}^3\Sigma_g^- + {}^3\Sigma_g^-$	5348	5325	5325
(3,0)	$^1\Delta_g + {}^1\Delta_g \leftarrow {}^3\Sigma_g^- + {}^3\Sigma_g^-$	4949	4949	--

2.3.4 VUV spectrum of CO in argon matrix

After satisfactory off-line performance testing, the MIS system is integrated with PPS beamline. A LiF windowed gate valve is used to isolate the MIS chamber from the rest of the beamline. For VUV photoabsorption studies using synchrotron radiation, a CaF_2 window is used as the substrate. VUV absorption spectrum of CO in argon matrix deposited at 10 K is recorded using SR. Total deposition is varied from 2 to 50 mbar at deposition rate of ~1mbar/min to obtain different film thicknesses.

Spectra of CO in gas phase as well in argon matrix phase are shown in Fig. 2.12. Observed band positions are listed in Table 2.5 along with previously reported values for comparison. There is an overall good agreement between the present studies and reported values, thus validating the performance of the MIS setup with synchrotron radiation. It may be noted that for spectroscopy work on CO in argon matrix, CO need not be introduced into the system, since the residual CO as impurity in the vacuum chamber suffices the purpose. For VUV spectroscopy of other molecules in the rare gas matrices, it is important to remove the residual CO via extensive evacuation and conditioning of the MIS system. This strategy is confirmed by recording VUV spectrum of pure Ar films at 10 K. The results confirm the satisfactory performance of the MIS system.

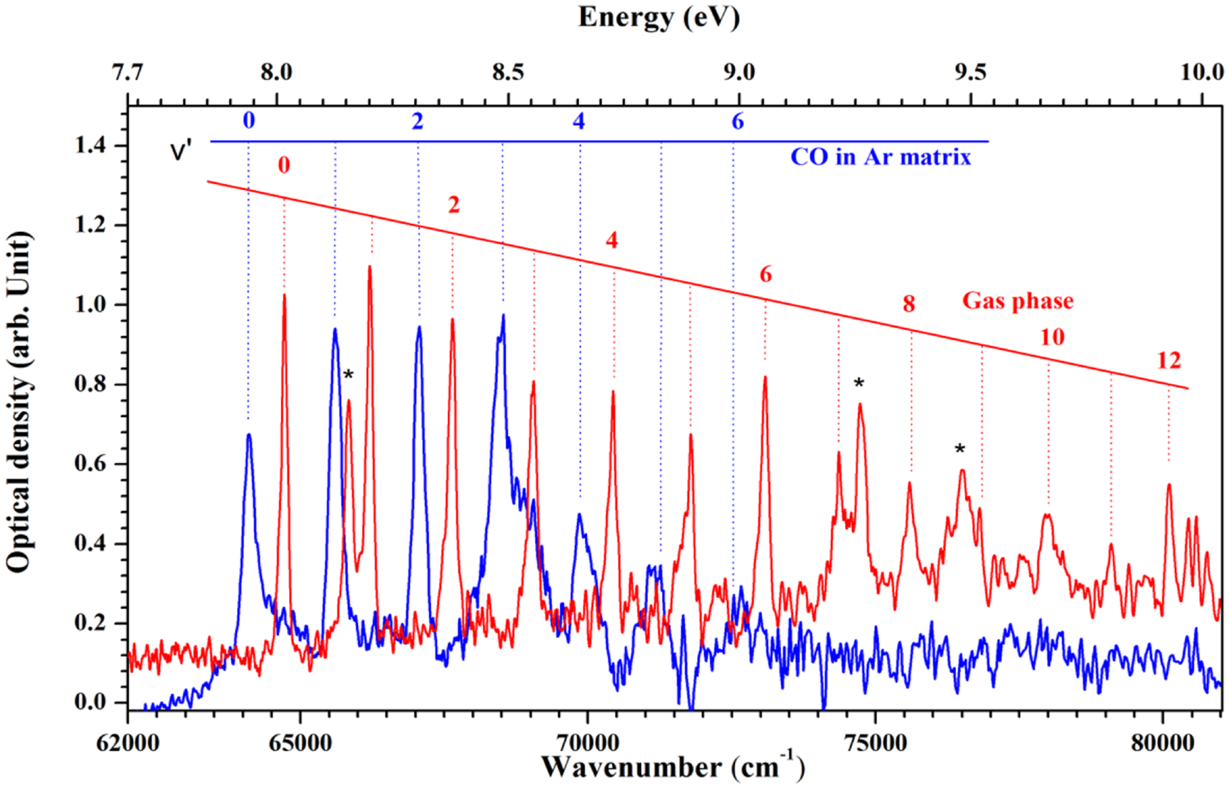

Figure 2.12: VUV absorption spectrum of CO using synchrotron radiation in gas phase and in argon matrix. Asterisks denote peaks of unknown origin.

Table 2.5: Observed spectral features in the $A^1\Pi \leftarrow X$ system of CO

v'	Gas Phase			CO in Argon		
	Present study	**Ref [72]**	**Ref [73]**	**v'**	**Present study**	**Ref [72]**
	64,714	64,744	--	0	64,096	64,130
	65,839[a]	--	--	1	65,599	65,630
0	66,210	66,228	66,218	2	67,070	67,090
1	67,646	67,669	67,670	3	68,525	68,510
2	69,055	69,079	69,122	4	69,878	69,900
3	70,434	70,453	70,493		71,096[a]	--
4	71,792	71,800	71,783	5	71,255	71,240
5	73,082	73,111	73,154	6	72,528	72,540
6	74,363	74,383	74,364		72,662[a]	--
7	74,727	75,623	75,655			
	75,605[a]	--	--			
8	76,815	76,828	76,865			
9	77,937	77,993	77,994			
10	79,095	79,140	79,123			
	79,402[a]	--	--			
	80,115[a]	--	--			
11	--	80,244	80,252			
	80446[a]	--	--			

[a] peaks of unknown origin.

Chapter-3

Vibronic analysis of $\tilde{E} - \tilde{X}$ system of SO_2

3.1 Introduction

Sulphur dioxide (SO_2) is a common atmospheric pollutant and is also found in planetary atmospheres and the interstellar medium; the sulphur cycle playing an important role in the atmosphere of Venus and Io [74-76]. On the earth, the major source of SO_2 in the stratosphere is from volcanic emissions whereas tropospheric SO_2 is known to arise mainly from fossil fuel combustion. Quantitative measurements of SO_2 from volcanic eruptions have been recently performed by satellite based detection in the UV/visible region [77]. SO_2 is a precursor of sulphates which form major components of tropospheric and stratospheric aerosols and acid rain [78]. These reactions are initiated by the oxidation of SO_2 either by chemical reactions or photolysis. Due to its impact on the environment and its presence in various astrophysical objects like comets and planets, photochemistry of SO_2 has been studied quite extensively [78, 79]. An understanding of the electronically excited states of SO_2 is of paramount importance in gaining an insight into its complex photochemistry.

The electronic absorption spectrum of SO_2 extends from visible to VUV-soft X-ray regions, and exhibits rich and complex structure. Photoabsorption studies of SO_2 in the UV-visible and VUV regions have concentrated mainly on absorption cross section measurements due to the importance of this data in astrophysics and environmental sciences [76, 80-87]. The first electronic absorption bands lie in the visible region above 3500 Å (< 3.5 eV) and involve excited triplet states [50, 88]. The next region *viz*. 2500–3500 Å (3.5–5.0 eV) shows an intense absorption system due to a forbidden transition which is made allowed via the Herzberg-Teller effect [50]. Interestingly, the geometries of the upper electronic states in the first two excited states differ considerably from the ground state geometry and also from each other. The $\tilde{X}^1A_1 \rightarrow {}^1B_2$ system of SO_2 lying in the 1700–2300 Å region has been the subject of numerous investigations [52, 53, 89-91]. Analysis of the vibronic structure in this region has led to the conclusion that the geometry of the excited state is not only considerably different, but also has unequal SO bond lengths resulting in a modification of the point group from C_{2v} in the ground state to C_s in the excited state [90, 91]. In the deeper VUV region, i.e. < 1700 Å (>7.3 eV), gas phase photoabsorption studies of SO_2 are few and sparse [51, 85, 92]. The VUV absorption spectrum of SO_2 in the wavelength region 1380–1600 Å (7.7–9.0 eV) corresponds to the system classically designated as $\tilde{E} - \tilde{X}$ [50, 51, 88]. Early VUV studies have reported the presence of three diffuse bands in the region 1400–1600 Å [88], a picture revised later with the advent of better VUV sources and optical equipment. Holtom *et al*. [93] have carried out VUV photoabsorption studies on SO_2 ice with a view to understand its behavior in the interstellar medium. They have concluded that while the gas phase spectrum indicates the presence of a single excited state, electron impact studies [94-97] suggest that there may be two electronic states in this region, one of which is a triplet. The atmospheric importance of the molecule has prompted several studies probing photodissociation dynamics proceeding through excitation to the $\tilde{E}$ state [78, 79]. Two-photon pump–probe experiments in the region of the $\tilde{E}$ state show that photodissociation in this region proceeds via cleavage of an S–O bond to form sulphur monoxide in an excited state [78]. Although there exist a few earlier reports which have attempted to carry out vibronic analysis of this system, they have had very limited success [50, 51]. For example, theoretical calculations by Palmer *et al.* [50] predict several singlet and triplet valence electronic states with high oscillator strength lying between 7.6–9.2 eV. However no definitive conclusions regarding the excited electronic and vibrational states involved in the transitions have been drawn.

The absence of detailed studies of concrete spectroscopic assignments and understanding of the symmetries of the excited states in the $\tilde{E} - \tilde{X}$ system motivated the present study. Experimental and theoretical investigations on the photoabsorption spectrum of SO_2 in the 7.6–9.2 eV region are discussed in this chapter.

3.2 Experimental

Photoabsorption studies of sulphur dioxide are carried out at a resolution of ~0.3 Å using the HRVUV beamline. Details of this beamline and experimental setup are discussed in Chapter-2. The SO_2 sample (M/s. Alchemie Gases, India) of stated purity of 99.9% is used without further purification. The atomic absorption line of Xenon at 1469 Å is used as a reference to calibrate the wavelength scale. The absorption signal is normalized with respect to the synchrotron beam current. Spectrum is recorded at several sample pressures in the range of 10^{-1} to 10^{-3} mbar. The optimum pressure for observation of the VUV spectrum in the region of interest is found to be ~0.01 mbar. No evidence of any impurities is observed in the recorded spectrum.

3.3 Results and discussion

3.3.1 Experimental observations

The photoabsorption spectrum of SO_2 in the 1350–1650 Å (7.6–9.2 eV) region recorded on the HRVUV beamline is shown in Fig. 3.1. The spectrum consists of several bands superimposed on an underlying continuum. The observed bands are listed in Table 3.1. Compared to earlier studies which have reported ~8–10 bands in the 1400–1600 Å region [51], more than 13 distinct bands are identified in the present study. Owing to the better resolution, each of these bands can be discerned to further consist of several peaks. There is apparently no single progression that these bands can be arranged into, suggesting that the observed vibronic structure may be composed of several overlapping progressions. An overview of the band positions (*cf.* Fig. 3.1) shows that most of the intense features appear to be members of progressions in which the successive vibrational quanta are changing by 500–620 cm^{-1}. The maximum uncertainty in measurement is about ± 12 cm^{-1}. Also the regularity of the progression breaks down after a few members and another series starts. In this manner, six overlapping series may be identified as shown in Table 3.1. The inset of Fig. 3.1 shows an expanded view of the spectral region 64,400–66,500 cm^{-1}. A few series of lines (labeled a, b, c and d), which exhibit spacing of ~ 480–600 cm^{-1}, are marked in the inset. It is observed that every progression, which persists up to more than 3–4 members, can be classified into one of the series as given in Table 3.1. The progressions, which die out within 3 successive members, are not considered here. All spectral features are reproducible within the experimental accuracy.

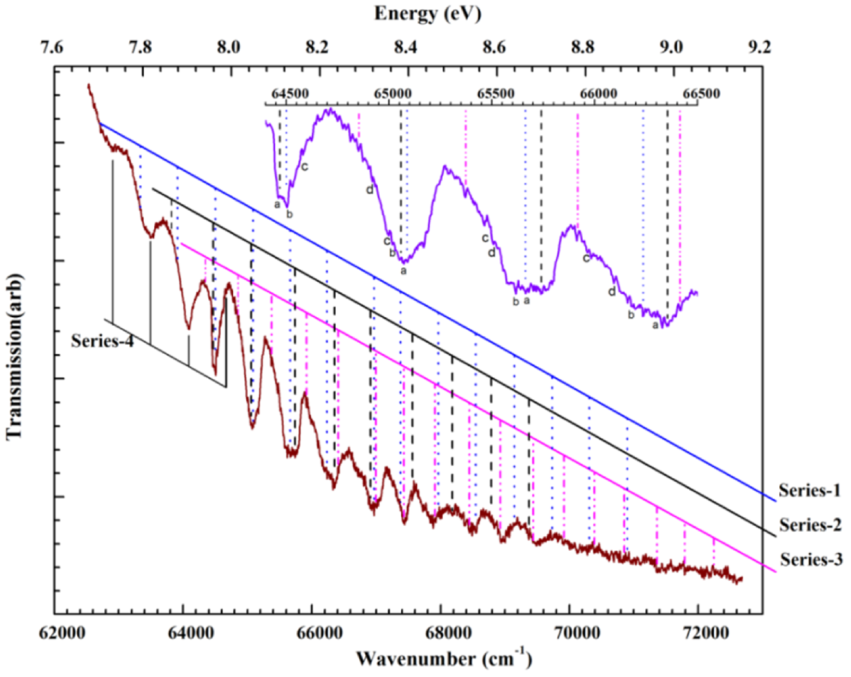

Figure 3.1: VUV photoabsorption spectrum of the $\tilde{E}$–$\tilde{X}$ system of SO_2 recorded using the HRVUV beamline. A few series of lines (labeled a, b, c and d) having spacing of ~480–600 cm^{-1}, are marked in the inset.

Table 3.1: List of observed bands in the the $\tilde{E}-\tilde{X}$ system of SO_2

S.no.	Series-1	Series-2	Series-3	Series-4	Series-5	Series-6
1	62,740	63,820	64,345	62,903	62,740	63,335
2	63,335	64,470	64,855	63,493	64,500	64,345
3	63,915	65,108	65,375	64,088	66,236	65,375
4	64,500	65,740	65,920	64,668	67,961	66,418
5	65,088	66,353	66,418		69,729	67,428
6	65,663	66,965	66,930		71,492	68,438
7	66,236	67,560	67,428			69,440
8	66,810	68,160	67,920			70,390
9	67,381	68,780	68,438			71,360
10	67,961	69,370	68,938			72,356
11	68,549		69,440			
12	69,139		69,910			
13	69,729		70,390			
14	70,307		70,858			
15	70,885		71,360			
16			71,795			
17			72,255			
Average separation	582(8)	617(20)	495(27)	588(8)	1750(19)	1002(28)

All values are in cm^{-1}, Entries in parenthesis are standard deviation.

A pertinent question is how many excited states are involved in the transition and what are their symmetries. Holtom *et al*. [93], in their study of SO_2 ice have observed two distinct peaks at 7.8 eV and 8.4 eV in the amorphous solid phase and an additional peak at 7.2 eV in the crystalline solid phase. Similarly electron energy loss studies have also observed the presence of two states in this region at 7.8 eV and 8.45 eV [95]. According to Palmer *et al*. [50], there is a smooth progression starting at about 61,976 cm^{-1} (7.684 eV), with a spacing of 588 cm^{-1} (73 meV) which breaks down after 8 members followed by two further sequences at ~66,169 cm^{-1} (8.204 eV) and 68,678 cm^{-1} (8.515 eV). However whether these series originate from the same electronic transition is uncertain [50] and related to this is an important issue concerning the excited state geometry. It has been concluded from vibrational and rotational analysis that several of the low lying excited states of SO_2 have an equilibrium geometry differing considerably from the ground state and sometimes showing unequal bond lengths [98, 99]. It is not clear whether a similar conclusion can be drawn in the case of the excited states in the 7.6–9.2 eV region, since such studies have not been carried out so far for this energy region. Nonetheless observation of a large number of vibrational quanta certainly suggests a change in geometry upon excitation. This, however, needs to be addressed with the help of theoretical calculations, as described in subsequent sections.

3.3.2 Computational results

SO_2 is an 18 valence electron system having a bent C_{2v} geometry in the ground state. The ground state molecular orbital configuration is given by: [core] $(5a_1)^2(3b_2)^2(6a_1)^2(4b_2)^2(7a_1)^2(2b_1)^2(5b_2)^2(1a_2)^2(8a_1)^2$ which gives rise to a $\tilde{X}^1A_1$ state. The coordinate system used for calculations is such that the SO_2 molecule is in the YZ plane with the sulphur atom lying on the Z axis. The contour plots of a few highest occupied and lowest unoccupied MOs are visualized using the software MacMolPlt [100] and are shown in Fig. 3.2. The HOMO ($8a_1$) is a sulphur lone pair non-bonding orbital. Further HOMO-1, HOMO-2 show nonbonding character, and HOMO-3 has some bonding character between S and O. Similarly LUMO+1 and LUMO+2 show weak bonding character, and LUMO and LUMO+3 are of nonbonding nature. Palmer *et al.* [50] have carried out extensive theoretical calculations of electronically excited states of SO_2 and have reported singlet and triplet excitation energies for valence and Rydberg states up to the first ionization potential. Detailed computations of a few potential energy surfaces of excited electronic states have been carried out by Kamiya and Matsui [101] with particular emphasis on understanding of the dissociation dynamics of the $^1B_2$ state. However there is no report on geometry optimization and vibrational frequency calculations of the excited states lying in the 7.6–9.2 eV region, to the best of our knowledge.

Since the region of interest is 7.6–9.2 eV, calculations in the present study are restricted to excited states lying below ~10 eV. Electron correlation is handled employing the DFT, CI and the MP2 methods. DFT computations are carried out using two hybrid exchange correlation GGA functionals PBE0 [35] and B3LYP [33, 34]. Basis sets used in the calculations include Pople's split valence basis set 6-31G (3d) with three d-type polarization functions [102], correlation consistent polarized basis sets of Dunning cc-pVnZ [103, 104] and the polarization consistent basis sets of Jensen, pc-4 [105, 106]. These families of basis sets are suitable for recovering the correlation energy, whereas the pc-4 basis is known to be particularly suited to DFT calculations [107]. The aug-cc-pVnZ basis sets which are augmented with diffuse functions are also used for some of the calculations. Although some of the theoretical calculations presented here are not directly related to the analysis of the $\tilde{E}$–$\tilde{X}$ system, they nevertheless may serve as useful data for future work on SO_2.

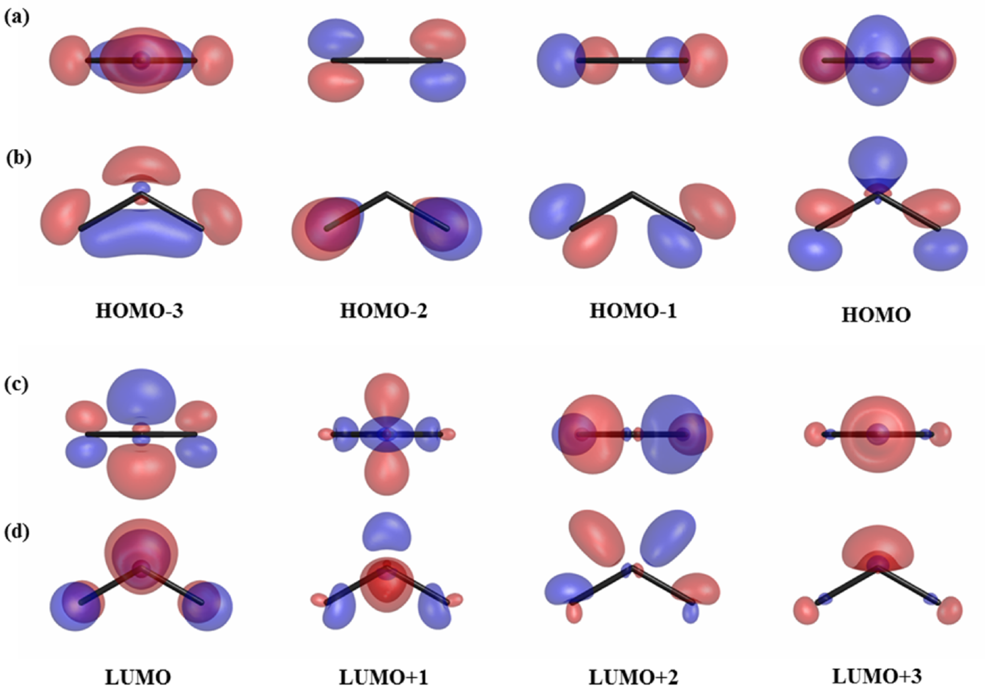

Figure 3.2: Contour plots of MOs (highest four occupied, lowest four unoccupied) at B3LYP/PC4 level viewed (a ,c) along z–axis and (b, d) along x–axis.

3.3.3 Ground state geometry and vibrational frequencies

The ground state equilibrium structure of SO_2 has been well studied in earlier experimental [108-112] and theoretical [50] works. The experimental equilibrium structure obtained from microwave studies [108] is r(S–O) = 1.430782 Å and θ(O–S–O) = 119.3297° whereas electron diffraction studies [111, 112] yield r = 1.4343 Å and θ = 119.5°. The theoretical values obtained by various computations [50] are also in agreement with these values. In the present study, the equilibrium geometrical parameters given by microwave studies [108] are used as the reference geometry. However, for maintaining consistency with excited state calculations, the ground state geometries are also optimized computationally. Ground state geometries optimized at various levels of theory and using different basis sets are presented in Table 3.2. Since the results of geometry optimization using the B3LYP and PBE0 functionals do not differ much, only the B3LYP functional is reported in Table 3.2. It is observed that the cc-pV5Z and pc-4 basis sets yield the best results. Further for a given basis set, the agreement with experimental data is better in the case of B3LYP.

Vibrational frequencies at the ground state optimized geometries calculated using GAMESS (USA) are shown in Table 3.3. The frequencies are in good agreement with the experimentally observed frequencies of the ground state of SO_2 *viz.* the symmetric stretch (ν_1) = 1151 cm^{-1}, bending (ν_2) = 518 cm^{-1} and the asymmetric stretch (ν_3) = 1362 cm^{-1} [88]. The closest match with experimental frequencies is given by the DFT/B3LYP with the basis set 6-31G (3d)+. A further test of the appropriateness of the basis sets used is provided by calculation of the first ionization energy of SO_2 using different methods and basis sets. These are listed in Table 3.3. Calculated ionization energies, ionic structure and frequencies agree remarkably well with the reported experimental values [113] and previous theoretical calculations [114]. Thus the molecular system is well described by the methods and basis sets used.

Table 3.2: Ground state energies, optimized geometries and frequencies of SO_2.

Basis Set	r_e**(Å)**	θ_e**(°)**	**E(a.u.)**	**Frequencies (cm^{-1})**		
				ν_1	ν_2	ν_3
6-31G(3d)	1.442	119.45	-548.5065	1162	513	1371
	1.457	119.94	-547.7852	1092	495	1320
6-31G+(3d)	1.444	119.49	-548.5150	1154	508	1359
	1.459	120.04	-547.9603	1081	489	1304
cc-pVTZ	1.437	119.22	-548.5994	1184	522	1387
	1.447	119.96	-547.9603	1135	507	1365
aug-cc-pVTZ	1.438	119.11	-548.6048	1177	519	1375
	1.451	119.68	-547.9798	1120	499	1339
cc-pVQZ	1.435	119.18	-548.6189	1180	523	1380
	1.443	119.79	-548.0312	1134	508	1358
cc-pV5Z	1.434	119.19	-548.6274	1180	523	1380
	1.442	119.75	-548.0512	1134	508	1356
pc-4	1.434	119.24	-548.6298	1181	523	1380
	1.442	119.79	-548.0474	1133	507	1355
Experimental [108]	1.431	119.33	--	1151	518	1362

Upper and lower entries for each basis set are for DFT/ B3LYP and MP2; a.u. = atomic unit = 27.2 eV.

Table 3.3: Calculation of ionization energies (eV) of SO_2 using DFT/B3LYP

Basis Set	**V.I.E.**	**A.I.E.**	**Optimized ground state parameters of SO_2^+**				
			Geometry		**Frequencies (cm^{-1})**		
			r**–SO(Å)**	θ**(°)**	ν_1	ν_2	ν_3
cc-pVTZ	12.338	12.169	1.425	132.35	1121	417	1303
aug-cc-pVTZ	12.439	12.270	1.426	132.35	1117	416	1297
cc-pVQZ	12.406	12.235	1.422	132.28	1120	420	1302
cc-pV5Z	12.441	12.270	1.422	132.38	1121	419	1307
aug-cc-pV5Z	12.433	12.262	1.422	132.38	1121	419	1306
pc-4	12.441	12.270	1.421	132.41	1121	420	1308
Previous work	---	12.350[a]	1.432[a]	136.50[a]	1151[a]	454[a]	1276[b]

V.I.E. = vertical ionization energy; A.I.E. = adiabatic ionization energy; [a]Ref [114]; [b]Ref [113]

3.3.4 Excited state energies, geometry optimization and vibrational frequencies

Excited state calculations are carried out using the TDDFT formalism and the *ab initio* CIS method. Vertical excitation energies (VEE) for the first few singlet states are calculated using the cc-pVnZ and pc-4 basis sets at both the experimental and the computationally optimized ground state geometry. Since the experimental geometry is known very accurately, the VEE of the first few singlet excited states at the experimental ground state geometry are given in Table 3.4.

Table 3.4: Calculated vertical excited states for for first few singlet states

	Present study				**Previous studies**	
Sym.	**cc-pVTZ**	**cc-pV5Z**	**aug- cc-pV5Z**	**PC4**	**QZVP/CI**[a]	**MRSD CI (DZP+d)**[b]
X^1A_1	0.000	0.000	0.000	0.000	0.000	0.000
2^1A_1	10.339(19819)	10.015(49644)	9.729(45496)	9.839(58625)	7.693 (13026)	9.08
	8.918(40341)	8.561(49628)	8.186(36045)	8.346(52937)		
3^1A_1	10.712(108432)	10.553(89560)	10.370(92073)	10.480(91944)	8.178 (28930)	9.56
	9.454(14368)	9.335(11234)	8.716(40846)	9.217(23877)		
4^1A_1	12.917(104800)	12.210(2386)	10.542(14417)	10.987(17014)	8.479 (49441)	--
	10.826(95925)	10.460(75414)	9.244(295)	9.384(16225)		
1^1A_2	5.589(0)	5.594(0)	5.592(0)	5.599(0)	4.165 (0)	4.47
	4.666(0)	4.656(0)	4.651(0)	4.654(0)		
2^1A_2	9.934(0)	9.889(0)	9.868(0)	9.877(0)	7.703 (0)	9.10
	8.440(0)	8.405(0)	8.398(0)	8.400(0)		
3^1A_2	10.631(0)	10.320(0)	10.058(0)	10.161(0)	8.831 (0)	--
	9.754(0)	9.416(0)	9.088(0)	9.227(0)		
1^1B_1	4.843(16176)	4.839(15307)	4.836(14999)	4.845(15204)	3.865 (4709)	4.34
	4.246(6036)	4.242(5654)	4.238(5522)	4.243(5575)		
2^1B_1	9.666(5726)	9.606(6585)	9.586(6859)	9.592(6794)	7.656 (4529)	8.84
	8.362(2299)	8.319(2688)	8.312(3036)	8.312(2930)		
3^1B_1	11.989(40065)	11.644(53870)	11.112(40007)	11.368(55506)	8.329 (12380)	--
	10.687(21579)	10.369(28396)	9.232(33548)	9.682(42828)		
1^1B_2	7.154(103489)	7.086(103855)	7.068(101937)	7.076(102407)	5.816 (118013)	6.75
	6.546(56360)	6.465(57505)	6.438(55472)	6.414(56448)		
2^1B_2	10.967(33657)	10.648(32892)	10.336(29613)	10.429(36414)	8.959 (612)	--
	9.539(2020)	9.177(799)	8.739(1535)	8.909(2974)		

Upper and lower entries for each state are for CIS and TDDFT in eV. Oscillator strengths ($x10^6$) are shown in parenthesis.
[a]Ref[50]; [b]Ref[101].

In a similar manner, vertical excitation energies for the first few triplet states calculated using the same basis sets and methods are listed in Table 3.5. In these tables, the excited states are arranged as per their symmetries in the order A_1, A_2, B_1, B_2. It is observed that the order of appearance of the various excited states calculated by different basis sets differs slightly except for the first four excited states. For example, the fifth excited state is predicted to be a $^1A_2$ using cc-pVnZ and pc-4 basis sets whereas using the aug-cc-pVnZ basis functions it is a $^1A_1$ state. This not unusual as the order of molecular orbitals, especially those lying close in energy often get re-ordered when the basis set is changed.

Table 3.5: Calculated vertical excited states for of first few triplet state

Symmetry	**Present Studies**				**Previous Studies**		
	cc-pVTZ	**cc-pV5Z**	**aug-cc-pV5Z**	**pc-4**	**CIS/ QZVP**[a]	**MRSD CI(DZP+d)**[b]	**V-SDTQ CI (DZP)**[b]
1^3A_1	6.955 7.129	6.892 7.051	6.872 7.033	6.878 7.039	6.648	7.81	7.82
2^3A_1	8.026 9.171	7.556 8.871	7.552 8.697	7.619 8.752	7.566	10.22	9.07
3^3A_1	9.693 11.676	9.431 11.309	8.555 10.010	8.865 10.435	8.717	--	--
4^3A_1	-- --	-- --	9.142 --	9.228 --	9.143	--	--
1^3A_2	4.116 5.021	4.116 5.027	4.114 5.025	4.117 5.033	3.801	4.45	4.86
2^3A_2	7.576 8.911	7.556 8.867	7.537 8.851	7.554 8.859	7.446	9.08	8.55
3^3A_2	9.301 10.036	9.013 9.754	8.771 9.557	9.112 9.629	8.160	--	--
1^3B_1	3.035 3.133	3.034 3.123	3.033 3.121	3.037 3.127	2.940	3.74	3.67
2^3B_1	7.548 8.546	7.504 8.464	7.496 8.441	7.498 8.448	7.111	8.37	8.37
3^3B_1	10.268 11.376	10.007 11.099	-- 10.856	-- 10.913	9.643	--	--
1^3B_2	3.806 3.921	3.823 3.939	3.823 3.939	3.828 3.951	3.635	4.23	4.60
2^3B_2	8.561 9.204	8.364 9.031	8.160 8.936	8.210 8.946	7.257	8.87	9.28
3^3B_2	8.734 10.346	8.485 10.134	8.278 9.989	8.356 10.037	8.184	--	--

Upper and lower entries for each state are for TDDFT and CIS in eV. [a]Ref [50]; [b]Ref [101]

It may be noted that for the B3LYP functional used here, significant errors are to be expected for $\Lambda < 0.3$ [37]. In the present study, the calculated Λ values for all the excited states are found to be greater than 0.4, with most of them lying between 0.5 and 0.8, thus confirming the suitability of the TDDFT method for these states. It may also be mentioned that a relatively large value of Λ implies short range excitations, therefore these states are predominantly valence in character as expected. The calculated values reported by Palmer *et al.* [50] and Kamiya *et al.* [101] where available are shown alongside for comparison. Whereas both the CIS and TDDFT energies obtained in the present study are somewhat higher than those reported by Palmer *et al.* [50], the TDDFT values are in better agreement with their work, while in very good agreement with the calculations by Kamiya *et al.* [101]. As can be seen from the listing of TDDFT energies several excited singlet and triplet states appear in the region 7.0–10.0 eV. Of these the singlet states with high oscillator strengths (2^1A_1, 3^1A_1, 2^1B_1 and 2^1B_2) are expected to contribute most significantly to the photoabsorption spectrum. Calculated oscillator strengths for these states using TDDFT/pc-4 are 0.052937, 0.023877, 0.002930 and 0.002974 respectively which are comparable to earlier reports [50]. It is to be noted that transitions to $^1B_1$ states cannot be accompanied by excitation of odd quanta of the asymmetric stretching mode ν_3' which is of b_2 symmetry. Therefore excitation of ν_1', ν_2' and even quanta of ν_3' are expected in this case. On the other hand transitions to $^1A_2$ states which are electronically forbidden, can be observed due to excitation of odd quanta of the ν_3' mode, therefore, the 2^1A_2 and 3^1A_2 states also can contribute to the spectrum through vibronic selection rules.

The geometry optimization of each of the excited states is attempted using the TDDFT method. It is found that the geometry optimization runs starting with the equilibrium ground state geometry converge for only a few excited states. For the excited states which fail to converge (2^1A_1 and 1^1A_2), it is concluded that the equilibrium geometry in the excited state is drastically different from the ground state geometry, a feature commonly encountered in polyatomic molecules. In the case of the 4^1A_1 state, calculated frequencies for ν_1' using two different basis sets viz. cc-pVTZ and pc-4 differ considerably. However as discussed below, this state is not expected to contribute to the spectrum, therefore it has not been considered further. Adiabatic excitation energies, optimized structures (r_e and θ_e) and vibrational frequencies for the geometry optimized states are calculated and compiled in Table 3.6. In all the optimized states, the symmetry of the molecule is close to C_{2v}, with the two SO bond lengths differing very slightly. Only one bond length is given here because the difference in bond lengths is ≤ 0.0001 Å in all cases. It can also be seen that the SO bond length is, without exception, larger in the excited states than in the ground state. The OSO bond angle on the other hand reduces considerably in the excited states with a percentage change of up to 20% in some cases. This suggests that electronic excitations to these states are likely to be accompanied by symmetric stretching or bending vibrations. The adiabatic excitation energies are in general lower than the vertical excitation energies by ~1 eV. Excitation in the Franck-Condon regime would therefore result in transitions to relatively high vibrational quanta.

Vibronic band positions corresponding to transitions from the ground state to excited electronic states can be predicted using Eq. (1.2). The predicted positions of the ν_{00} transitions for the singlet states lying in the region of interest are given in Table 3.7. It is clearly seen that the only states which can give rise to fairly long progressions in 62,000–72,000 cm^{-1} region are 3^1A_1, 2^1A_2 and 2^1B_1. The most intense vibronic transitions are of course expected to proceed from the $(0,0,0)''$ state. Due to the low energy of the bending mode, the $\nu_2(v''=1)$ level is expected to have a population of ~ 8% at room temperature. Thus hot band transitions from the $(0,1,0)''$ level may also appear as weak features in the spectrum. Simultaneous excitation of more than one mode in the excited electronic state leading to combination bands is also a distinct possibility.

Table 3.6: Geometry optimization and frequency calculation for excited singlet states using TDDFT

Symmetry	**V.E.E. (eV)**	**A.E.E. (eV)**	r_e**(Å)**	θ_e**(°)**	**Frequencies (cm^{-1})**		
					ν_1	ν_2	ν_3
X^1A_1	0.000	0.000	1.437	119.2	1184	522	1387
	0.000	0.000	1.434	119.2	1181	523	1380
2^1A_1	8.858	--	--	--	--	--	--
	8.327	--	--	--	--	--	--
3^1A_1	9.355	8.061	1.588	97.6	859	769	1540
	9.208	--	--	--	--	--	--
4^1A_1	10.721	8.934	1.634	110.0	2063	675	2630
	9.384	9.342	1.448	122.6	1242	479	2273
1^1A_2	4.584	--	--	--	--	--	--
	4.648	--	--	--	--	--	--
2^1A_2	8.369	7.746	1.537	108.0	922	442	1254
	8.391	--	--	--	--	--	--
3^1A_2	9.659	8.726	1.613	104.0	827	605	1418
	9.208	--	--	--	--	--	--
1^1B_1	4.186	3.433	1.529	94.9	781	421	1050
	4.229	3.454	1.525	94.8	778	425	1050
2^1B_1	8.266	7.427	1.570	117.8	897	380	1202
	8.295	7.428	1.567	117.4	897	382	1198
3^1B_1	10.586	--	--	--	--	--	--
	9.682	8.873	1.607	109.7	600	1721	1833
1^1B_2	6.460	5.610	1.548	105.1	455	392	960
	6.433	5.562	1.542	104.7	453	405	964
2^1B_2	9.463	--	--	--	--	--	--
	8.902	8.422	1.557	108.8	810	786	1417
3^1B_2	11.234	10.424	1.546	97.1	708	479	1412
	9.799	--	--	--	--	--	--

Upper and lower entries for each state are for cc-pVTZ/ B3LYP and pc-4 /B3LYP levels of theory;
V.E.E. = vertical excitation energy; A.E.E. = adiabatic excitation energy

Table 3.7: Predicted positions of the ν_{00} bands for selected states

Symmetry	**A.E.E(eV)**	**Z.P.E.(cm^{-1})**	**Band position (cm^{-1})**
X^1A_1	0.000	1515.5[a]	--
3^1A_1	8.061	1584.0	65085*
4^1A_1	8.934	2684.0	73226
2^1A_2	7.746	1309.0	62269*
3^1A_2	8.726	1425.0	70289
1^1B_1	3.433	1126.0	27268
2^1B_1	7.427	1240.0	59627*

[a]Ref [88]; A.E.E. = adiabatic excitation energy; Z.P.E.= zero point energy.
*Denotes states which can give rise to progressions in the observed region.

3.3.5 Potential energy curves

In order to probe the nature of the excited states which can give rise to transitions in the 7.0–9.0 eV region, potential energy curves (PECs) for the first few excited singlet and triplet states are generated at the CIS/cc-pVTZ level. PECs as functions of the OSO bond angle as well as the SO bond lengths are shown in Figs. 3.3–3.7. PEC as a function of bond angle for singlet and triplet states are shown plotted together in Fig. 3.7. PECs with respect to symmetric and asymmetric variation of the bond lengths (Figs. 3.5 and 3.6) show fairly regular behavior in the vicinity of the equilibrium geometry. The overall results for the PECs agree well with the work of Kamiya *et al*. [101]. The curves are plotted by performing a single point energy calculation at each geometrical configuration. The calculated points are simply joined together and fitted with a spline function.

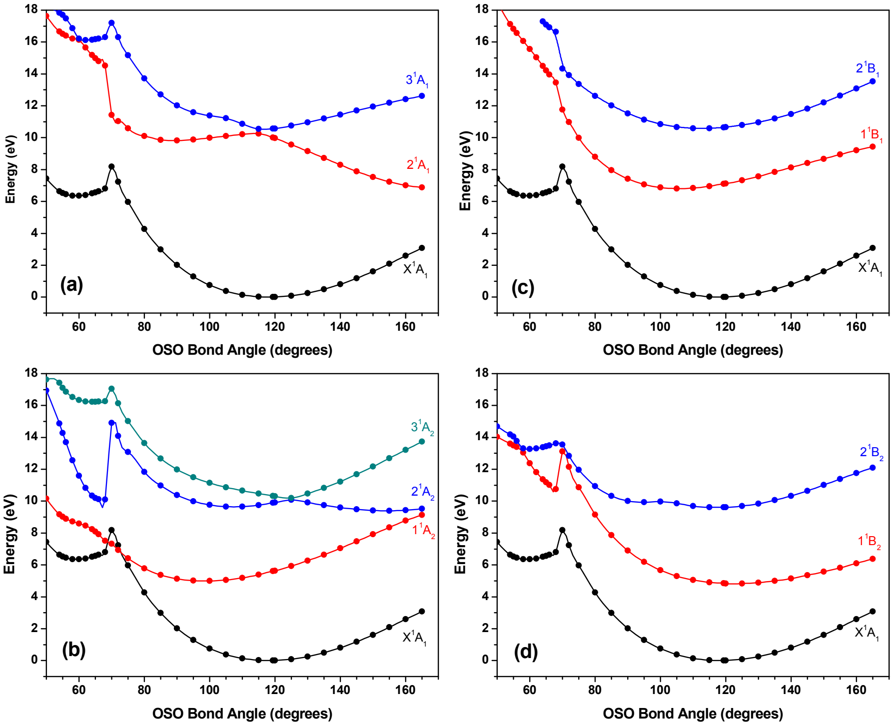

Figure 3.3: Potential energy curves for singlet states with respect to OSO bond angle, keeping SO bond lengths fixed at equilibrium value. Frames (a)-(d) correspond to $^1A_1$, $^1A_2$, $^1B_1$ and $^1B_2$ symmetry. The ground state is shown in all frames for reference.

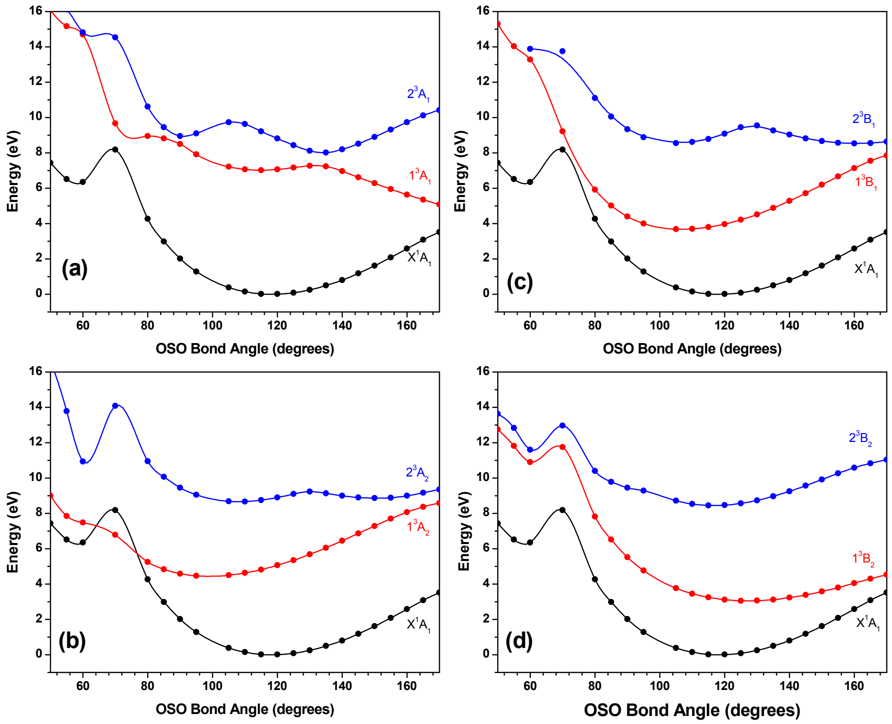

Figure 3.4: Same as Fig.3.3 but for the triplet states. Frames (a)-(d) correspond to $^3A_1$, $^3A_2$, $^3B_1$ and $^3B_2$ symmetry. The ground state is shown in all frames for reference.

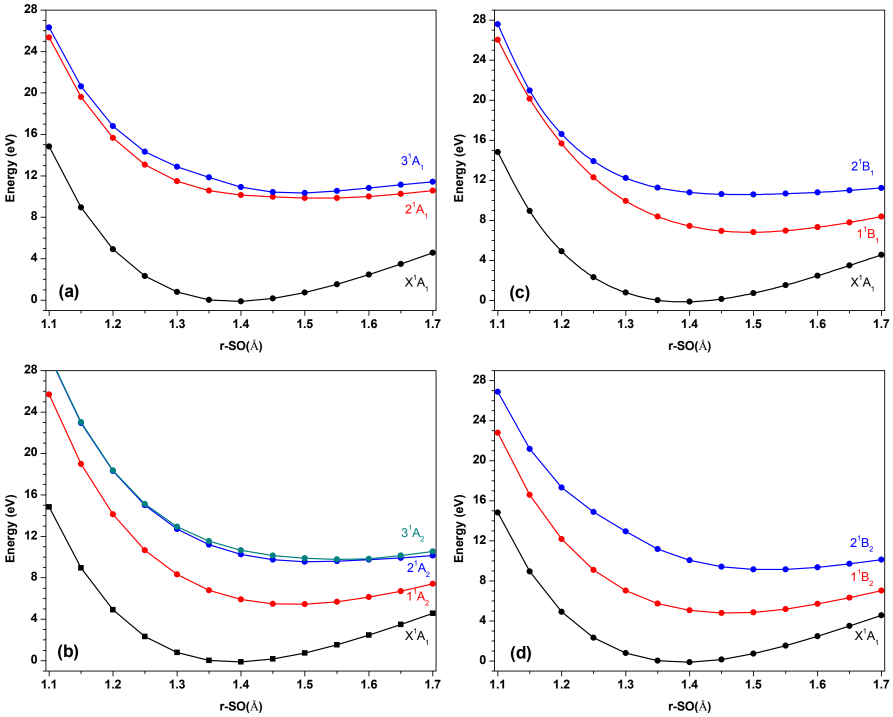

Figure 3.5: Potential energy curves with respect to a symmetric variation of SO bond length, keeping OSO bond angle fixed at equilibrium value. Frames (a)-(d) correspond to $^1A_1$, $^1A_2$, $^1B_1$ and $^1B_2$ symmetry. The ground state is shown in all frames for reference.

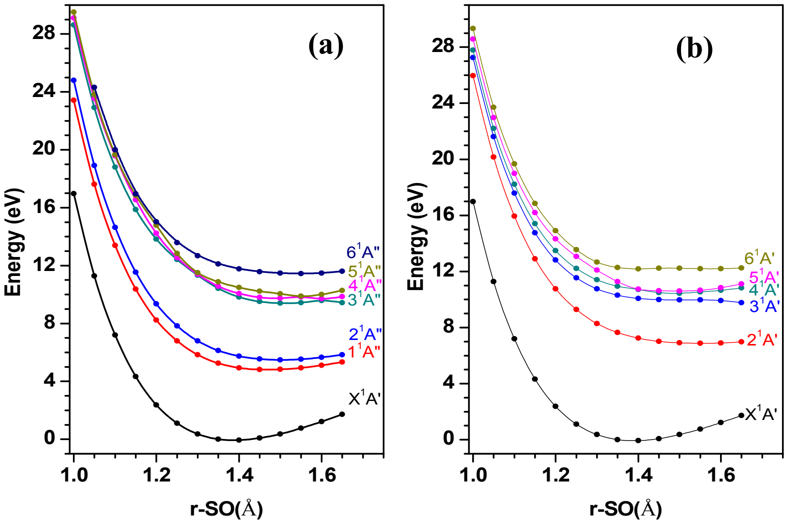

Figure 3.6: Potential energy curves with respect to an asymmetric variation of SO bond length, keeping OSO bond angle and one SO bond length fixed at equilibrium value. Frames (a) and (b) correspond to A″ and A′ symmetry. The ground state is shown in both frames for reference.

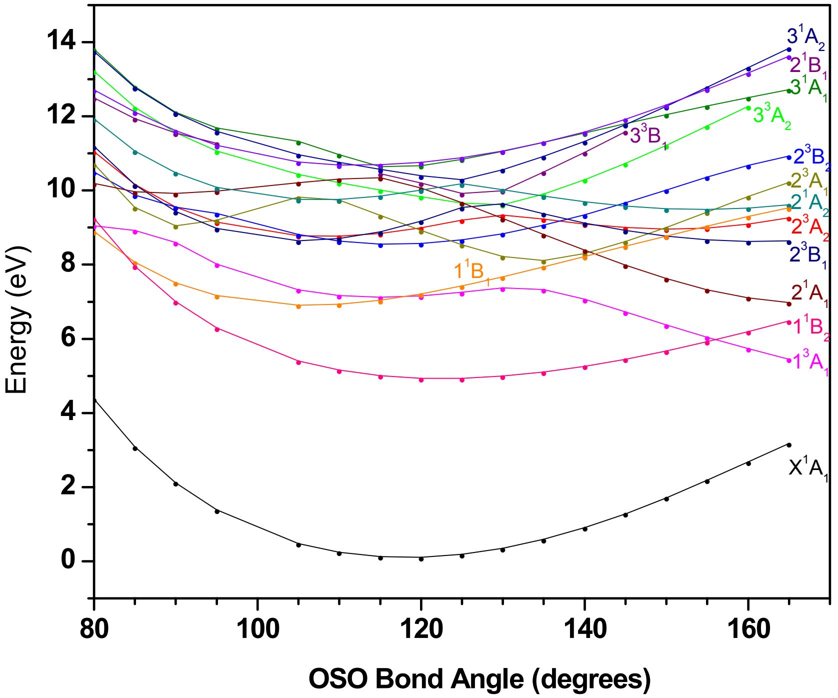

Figure 3.7: An expanded view of the singlet and triplet potential energy curves with respect to bond angle in the energy region ~ 6eV – 11eV.

At the outset, the PECs for singlets and triplets as a function of bond angle present a very complex picture (*cf.* Fig. 3.6). However, a few qualitative observations may be made. The PECs show extensive overlap and crossing over at several points. Some states like the 2^3A_1 show a double well potential structure with local minima at about 90º and 135º. The 2^1A_1 state, which has appreciable oscillator strength, shows a local maximum at angles slightly lower than the ground state equilibrium OSO angle of 120º. This is probably due to an avoided crossing with the 3^1A_1 state (*cf.* Fig. 3.3). At higher angle, this state shows a repulsive behavior. The origin of the underlying continuum in in the $\tilde{E}-\tilde{X}$ system may be partly attributed to transitions to this repulsive region.

3.4 Correlation of experimental data with theoretical results

A comparison of the theoretically predicted band positions with the experimental data helps to carry out tentative assignments of the bands observed in the experiment (*cf.* Table 3.7). Of the observed 4 series (*cf.* Fig. 3.1) with successive spacing of ~500–620 cm^{-1}, at least 15 members in series-1, 10 members in series-2, 17 members in series-3 and 4 members in series-4 could be distinguished. Overlapping with these series, two more could be identified *viz*. series–5 and 6 (*cf.* Table 3.1). It may be mentioned that Palmer *et al.* [50] have reported a breakdown of the first series after 8 members with a spacing of ~ 588 cm^{-1}. The present theoretical results (*cf.* Table 3.6) do not predict any excited state frequency for the energy region under consideration which can be correlated with experimentally observed spacing of ~580 cm^{-1}.

Of the excited states which lie in the energy region of interest, transition to the 2^1A_1 state is a possibility, but the potential energy plot (*cf.* Fig. 3.2) shows that a vertical transition to this state exhibits a saddle point at ~115º. Thus, although transition to 2^1A_1 has high oscillator strength, it could contribute to the underlying continuum, but not to the vibronic structure. Moreover, the unusual vibrational frequencies obtained for the 3^1A_1 state *viz*. ν_1' (859 cm-1) ≈ ν_2' (769 cm^{-1}) could be due to its avoided crossing with the 2^1A_1 state. As such all the three states *viz*. 3^1A_1, 2^1A_2 and 2^1B_1 can give rise to extensive series in this region. The calculated frequencies obtained for the 3^1A_1 and 2^1B_1 states cannot explain the observed spacing of ~590 cm^{-1}. The 2^1A_2 state which is dipole forbidden can be excited only if accompanied by odd quanta of the ν_3' mode, therefore the four series with average spacing of ~590 cm^{-1} cannot be associated with this state. However it is possible that alternate members of these series spaced by ~1250 cm^{-1} may be assigned to the ν_3' vibrational mode of the 2^1A_2 state. Moreover, the predicted value of the ν_3' frequency of the 2^1B_1 state is also of the same order (1202 cm^{-1}), therefore these series could belong to either of these two states (2^1A_2 or 2^1B_1). Alternate members of this series can therefore be assigned to 2^1A_2 and 2^1B_1 through excitation of the asymmetric stretching mode ν_3'. The combination mode (ν_2' + ν_3') of the 3^1A_1 state (2310 cm^{-1}) can also account for some of the members of this series.

The fifth series with separation of ~1750 cm^{-1} can arise due to the combination mode (ν_1' + ν_2') of the 3^1A_1 state (~1630 cm^{-1}). The combination modes (ν_2' + ν_3') of the 2^1A_2 (~1700cm^{-1}) or 2^1B_1 (~1580 cm^{-1}) states can also contribute to alternate members. However, it is seen (*cf.* Table 3.6) that there is a larger change in the OSO bond angle for the 3^1A_1 and 2^1A_2 states as compared to the 2^1B_1. This indicates that excitation of the bending mode ν_2' is more likely for these states. Therefore, series-5 is probably due to the combination modes (ν_1' + ν_2') and (ν_2' + ν_3') of the 3^1A_1 and 2^1A_2 states respectively. Series-6 (~1000 cm^{-1}) can be identified with the ν_1' modes of 3^1A_1 or 2^1B_1. It may be noted that present analysis is based on the average spacing observed experimentally. Small discrepancies may be attributed to effects like anharmonicity and higher order perturbations which are not included in the present studies. Although it is very difficult to assign vibrational quantum numbers to the observed transitions, it is nevertheless very likely that all the series listed in Table 3.1

can be assigned to the electronic transitions $\tilde{X}\,^1\mathrm{A}_1 \rightarrow 3\,^1\mathrm{A}_1$, $\tilde{X}\,^1\mathrm{A}_1 \rightarrow 2\,^1\mathrm{A}_2$ and $\tilde{X}\,^1\mathrm{A}_1 \rightarrow 2\,^1\mathrm{B}_1$. Geometry optimization calculations indicate that the molecule maintains C_{2v} symmetry in these excited states although the bond lengths and bond angle do differ from their ground state values.

3.5 Summary

Gas phase photoabsorption studies of the lesser understood ~1350–1625 Å (7.6–9.2 eV) region of the VUV spectrum of SO_2 are performed using SR from HRVUV beamline. Most of the observed bands are arranged into four series with successive band spacing of ~500 – 620 cm^{-1}. Two additional series with average separations of 1750 cm^{-1} and 1000 cm^{-1} are identified. All the observed series could be assigned to various vibronic transitions, however the exact vibrational numbering is not known. To aid the analysis of the spectrum, calculations of vertical and adiabatic excitation energies, equilibrium geometries and vibrational frequencies of excited electronic states are carried out. Calculated potential energy curves corresponding to each of the normal modes of the SO_2 molecule are helped in gaining a qualitative understanding of the nature of the excited states in this region. Based on the results of these computations, it is concluded that at least three excited electronic states are involved in the $\tilde{\mathrm{E}}-\tilde{\mathrm{X}}$ system *viz.* $\tilde{X}\,^1\mathrm{A}_1 \rightarrow 3\,^1\mathrm{A}_1$, $\tilde{X}\,^1\mathrm{A}_1 \rightarrow 2\,^1\mathrm{A}_2$ and $\tilde{X}\,^1\mathrm{A}_1 \rightarrow 2\,^1\mathrm{B}_1$. Further, the observed vibrational features are mainly due to excitation of the combination modes ($\nu_1' + \nu_2'$) and ($\nu_2' + \nu_3'$) with some contributions from ν_1' and ν_3'. Here ν_1', ν_2' and ν_3' denote the frequencies of symmetric stretch, bending and asymmetric stretch modes respectively in excited state. The present study is a step towards a better understanding of the excited state structure and dynamics of SO_2 in the 7.6–9.2 eV region.

Chapter-4

VUV photoabsorption studies of acetone

4.1 Introduction

Acetone is the simplest aliphatic ketone and is the first 10 atom molecule reported in the interstellar medium [115, 116]. The UV photodissociation of acetone is a source of ·OH radicals in the upper troposphere [117]. The importance of acetone in photochemistry and interstellar chemistry and its benchmark status in the study of methyl torsional effects have stimulated a large number of investigations over the past few decades [116-139]. The torsional vibrational mode is actually an internal rotation of the methyl group which is hindered from a 360° rotation by a potential barrier. Torsional modes have been recognized to play an important role in the structure and dynamics of excited electronic states of polyatomic molecules [131-133, 140-145]. In acetone, which is the smallest carbonyl compound having two methyl (CH_3) torsional groups [146], these vibrations have been explored with the aim of gaining insight into the nature of potential barriers inhibiting internal rotation [147-149]. The two torsional modes of acetone are shown in Fig. 4.1. Of the 24 normal modes of acetone, the two torsional modes are well separated in frequency from the other normal modes [150]. Due to the low frequency of these modes, an appreciable population is expected in excited torsional levels at room temperature. For instance ~70% (77%) of the ground state population would be in the ν_{12} state and ~55% (62%) in the ν_{24} state of acetone-h_6 (acetone-d_6) at room temperature. Thus the probability of occurrence of intense hot bands in the electronic absorption spectrum of acetone-h_6 and acetone-d_6 is rather high.

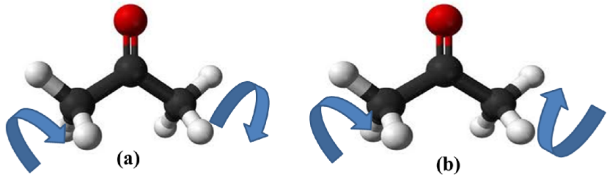

Figure 4.1: CH_3 torsional mode of acetone (a) in phase gearing mode ν_{12} (a_2 symmetry) and (b) out of phase antigearing mode ν_{24} (b_1 symmetry)

The excited electronic states of acetone have been extensively studied experimentally [119-121, 123-127, 129, 130, 132-136, 142, 145, 151-174] and theoretically [118, 129, 138, 139, 175-185] in the past few decades. Despite the significant role played by the torsional modes in the room temperature photoabsorption spectrum, very few reports have touched upon this aspect [133, 145, 151]. The electronic absorption spectrum of acetone lies largely in the VUV region, with one weak absorption system in the UV region. Subsequent to the early experiments by Duncan [152] and Lake and Harrison [153], numerous studies of the electronically excited states of acetone relevant to atmospheric chemistry, *viz*. photodissociation dynamics and quantum yield measurements [119-121, 126, 163-168] and UV absorption cross section measurements [124, 169] have been carried out. Photoionization [124, 169], photoelectron spectroscopy [171] and electron energy loss experiments [172-174] have also been used to probe the electronic structure. Quantum chemical calculations dealing with various aspects of the photoabsorption and photodissociation processes in acetone have been reported in recent years [118, 138, 139, 175-184].

The lowest observed transition in the electronic absorption spectrum is a broad band at about 4 eV which is attributed to a dipole forbidden transition, *viz*. $S_1(n, \pi^*)$ [123, 125, 127, 129, 130, 134-136, 154-162]. In the 6–9.7 eV region, the spectrum is dominated by *ns*, *np* and *nd* Rydberg series [123, 125, 127, 129, 130, 134-136, 151-154, 156-162, 186] converging to the first *IP* with valence states making an indirect appearance through vibronic coupling with the Rydberg states [127, 129]. The *ns* Rydberg series, especially the $n_y \rightarrow 3s$ transition lying at 6.35 eV [125, 127, 133, 136, 151, 156, 157, 186] is most extensively studied. A few vibronic features belonging to the 3*s* state have been assigned in earlier room temperature as well as jet cooled work [136, 151].

Polarization selected 2–photon and 3–photon resonance enhanced multiphoton ionization (REMPI) techniques have been used to investigate the 3*p* Rydberg states of acetone and to assign the accompanying vibronic structure [129, 130, 135, 158-162]. The order of the $3p_x$ (2^1A_2), $3p_y$ (2^1A_1) and $3p_z$ (2^1B_2) states has been satisfactorily established [129, 130, 158, 162]. Some of the highlights of these studies are the observation of several totally symmetric a_1 modes in the excited 3*p* states, reduction in frequency of the two a_1 symmetric CH stretching modes and interpretation of the vibrational perturbation of CH mode in terms of interstate vibrational coupling. In contrast, studies of the 3*d* Rydberg states and higher members ($n \geq 4$) of the *ns*, *np* and *nd* Rydberg are few and sparse. Mérchan *et al.* [129] have performed polarization selected photoaccoustic and resonance multiphoton ionization measurements on static and jet cooled samples of acetone-h_6 and acetone-d_6 along with *ab initio* calculations of vertical excited energies, potential energy curves and interactions between valence and Rydberg states. Anomalies in the observed intensities of the 3*d* Rydberg states are attributed to coupling of these states with a short lived $\pi \rightarrow \pi^*$ valence excited state [129]. Photoelectron spectroscopy of excited states populated by 2– or 3–photon excitation has been employed by ter Steege *et al.* [127] to study the vibronic structure and dynamics of 3*d* Rydberg states. They have reported the origins of several *np* and *nd* Rydberg states and also vibrational frequencies of a few Rydberg states.

Recently, the complete room temperature electronic absorption spectrum of acetone-h_6 up to its first *IP* (9.708 eV) using SR has been reported by Nobre *et al*. [123]. The authors have proposed vibronic assignments for a number of Rydberg and valence transitions, together with higher members of the *ns*, *np* and *nd* Rydberg series of acetone-h_6. However, the assignments of some of the vibronic features appear to be doubtful. This, partly may be due to non-inclusion of hot bands corresponding to population of the torsional modes in the ground state and an existing confusion related to the numbering of the vibrational modes ν_{13} to ν_{24} of acetone (*cf.* Table 4.1). The assignments of the Rydberg series origins (ν_{00}) and quantum defects in this work also show several discrepancies.

The present study is motivated by the need to clarify the assignments of the electronic and vibronic transitions observed in the photoabsorption spectrum of acetone. Considerable overlap and interaction between valence and Rydberg states lead to difficulties in assignments. Additionally, vibrational assignments in excited electronic states are complicated by the fact that that direct measurements of vibrational frequencies are not usually available, and one has to depend on theoretically predicted values or ionic frequencies. Since the geometry of the excited states could be considerably different from the ground state or ionic geometries, there is always an element of uncertainty in assignments carried out using these values. In this context, isotopic substitution is a useful and well known tool for confirming vibrational assignments in molecular spectra [187-190]. Frequency shifts expected for various normal modes can be used to ascertain the accuracy of the assignments. Several earlier papers on the excited electronic states of acetone have also used the isotope shift to assign vibrational features in 3*s* and 3*p* states [127, 129-137]. The only prior study of deuteroacetone which covers the entire VUV region (6.2–9.7 eV) is the early report by Lawson and Duncan [137] using a hydrogen discharge source and photographic plate detection. Subsequent reports [123, 127, 129-136] have carried out more detailed studies in small wavelength regions.

However, a complete assignment of the entire VUV region was not reported. In the present work, UV and VUV photoabsorption studies of acetone-h_6 and acetone-d_6 are performed using SR. Detailed Rydberg and vibronic analysis in the entire VUV region up to the first *IP* are presented in the following sections.

4.2 Experimental

VUV photoabsorption studies of acetone-h_6 and acetone-d_6 are performed using the experimental setup on photophysics beamline. Samples of purity >99.5% (M/s Sigma Aldrich, USA) are used after subjecting them to several freeze-pump-thaw cycles to eliminate volatile impurities. Spectra are recorded at several sample pressures of 10^{-4} mbar to 100 mbar in VUV region. The optimum pressure for obtaining clear absorption features in the VUV region is ~0.01 mbar. Higher pressures (1–100 mbar) are used for recording the UV region due to relatively low absorption cross sections.

4.3 Results and discussion

Acetone belongs to the C_{2v} point group with the ground state electronic configuration $...(2b_1)^2(5b_2)^2$: 1^1A_1. The contour plots of a few MOs generated using the software MacMolPlt [100] are shown in Fig. 4.2. The HOMO has a weak bonding character between two carbon atoms and a non–bonding lone pair character on O atom; approximately represented by the $2p_y$ atomic orbital on O. HOMO-1 shows σ type bonding character between C–H and π type bonding between C and O. HOMO-2 shows bonding between C–C–C and C–H with an O lone pair, while HOMO-3 is a purely bonding orbital. The LUMO has nonbonding character while LUMO+1 and LUMO+2 are very similar and show predominantly non-bonding character. LUMO+3 also exhibits an O lone pair along with weak bonding character between two of the C–H bonds. The first few excited states of acetone arise from promotion of an electron from these lone pair orbitals. The symmetries and energies of excited electronic states 3*s*, 3p_x, 3p_y, 3p_z, 3d_{xy}, 3d_{yz} and $3d_{x^2-y^2}$ are reported in literature [127, 129].

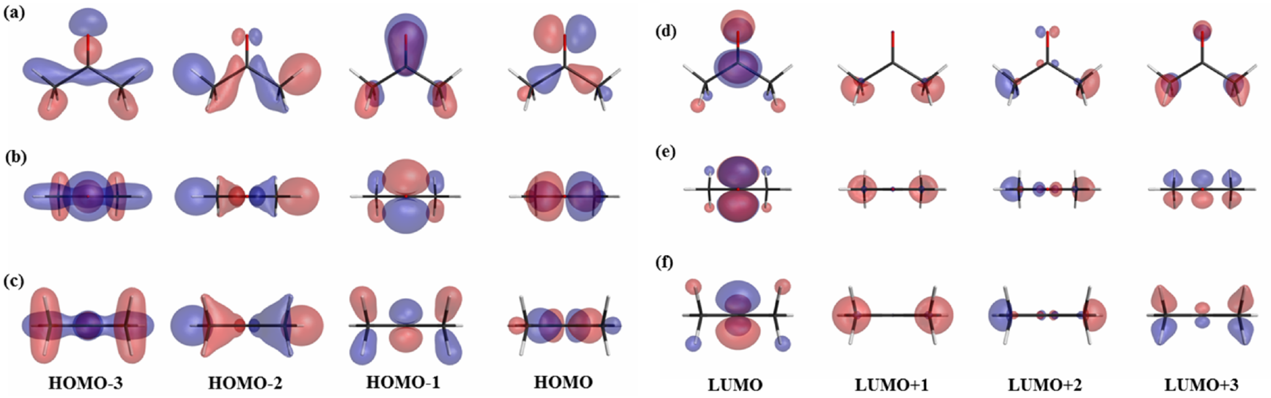

Figure 4.2: Contour plots of MOs of acetone (highest four occupied, lowest four unoccupied) view from x–axis (a, d), along z–axis in –z direction (b, e) and along z–axis in +z direction (c, f).

The ground state and excited state frequencies available from earlier studies for acetone-h$_6$ and acetone-d$_6$ are given in Table 4.1. While the 24 fundamental vibrational modes of acetone are well established from infrared spectroscopy [150], there is some ambiguity regarding the classification and numbering of the normal modes ν_{13} to ν_{24}. The reason may be traced to the choice of the Cartesian axes X, Y, Z with respect to the molecule. By convention, the Z axis is taken to be the symmetry axis C$_2$ which lies along the C=O bond. If the molecule is assumed to be placed in the YZ plane, so that the out of plane direction is along X, then the modes ν_{13} to ν_{19} belong to b_2 and modes ν_{19} to ν_{24} belong to b_1. If, on the other hand, the molecule is placed in the XZ plane, then the normal modes ν_{13} to ν_{19} belong to b_1 and modes ν_{19} to ν_{24} belong to b_2 as given by Shimanouchi [150]. The antigearing torsional mode (*cf.* Fig. 4.1) would be classified as b_1 with the former choice of axes, and b_2 with the latter. This mode has been labeled as ν_{17} by some authors [133, 136, 151, 158] and ν_{24} by others [123, 127, 150]. In the present work, convention of placing the molecule in the YZ plane is followed while retaining the numbering scheme given by Shimanouchi [150].

Table 4.1: Vibrational frequencies of acetone in the ground, 3s, 3p_x, 3p_y, 3p_z and ionic states

Symmetry and Normal mode		**Ground State**[a]	**3s**[b]	**3p_x**[b]	**3p_y**[b]	**3p_z**[b]	**Ionic (Calc)**[c]
$\nu_1(a_1)$	CH_3-d-stretch	3019	--	--	3128	3148	3084
	CD_3-d-stretch	2264	--	2433	--	2411	2291
$\nu_2(a_1)$	CH_3-s-stretch	2937	--	--	2424	--	2940
	CD_3-s-stretch	2123	--	2165	1792	--	2108
$\nu_3(a_1)$	CO stretch (ac-h_6)	1731	--	1468	--	--	1570
	CO stretch (ac-d_6)	1732	--	--	--	--	1534
$\nu_4(a_1)$	CH_3-d-deform	1435	1232	1373/1395	--	1367/1376	1395
	CD_3-d-deform	1080	991[d]	1,028,941	--	1,022,967	1030
$\nu_5(a_1)$	CH_3-s-deform	1364	1191/1160	1293	1309	1272/1280	1269
	CD_3-s-deform	1035	914[d]	969	--	--	966
$\nu_6(a_1)$	CH_3 rock	1066	1047/1016	1056/1050	1023/1058	1036/1042	1045
	CD_3 rock	887	827[d]	823/823	832/840	817/822	798
$\nu_7(a_1)$	CC stretch (ac-h_6)	777	763	--	--	733	675
	CC stretch (ac-d_6)	689	691[d]	672	660	665	669
$\nu_8(a_1)$	CCC deform (ac-h_6)	385	322/309	327/326.2	327/324	310/316	321
	CCC deform (ac-d_6)	320	279[d]	286	278, 280	275/280	234
$\nu_9(a_2)$	CH_3-d-stretch	2963	--	--	--	--	3007
	CD_3-d-stretch	2205	--	--	--	--	2228
$\nu_{10}(a_2)$	CH_3-d-deform	1426	--	1432	--	--	1400/1484
	CD_3-d-deform	1021	--	1109	--	--	1113
$\nu_{11}(a_2)$	CH_3 rock	877	--	892	--	--	868
	CD_3 rock	669	--	671	--	--	678
$\nu_{12}(a_2)$	CH_3 torsion (in phase)	77.8	118/133	72/70.8	70	--	-49/ 66.7[e]
	CD_3 torsion (in phase)	53.4	33[d]	49/49.1[f]	53.4[f]	--	42.4
$\nu_{13}(b_2)$	CH_3-d-stretch	3019	--	--	--	--	3083
	CD_3-d-stretch	2264	--	--	--	--	2287
$\nu_{14}(b_2)$	CH_3-d-stretch	2937	--	--	--	--	2933
	CD_3-d-stretch	2123	--	--	--	--	2103
$\nu_{15}(b_2)$	CH_3-d-deform	1410	--	--	--	--	1385
	CD_3-d-deform	1004	--	--	--	877	898
$\nu_{16}(b_2)$	CH_3-s-deform	1364	--	--	--	--	1313
	CD_3-s-deform	1035	--	--	--	--	988
$\nu_{17}(b_2)$	CC stretch (ac-h_6)	1216	--	--	--	--	984
	CC stretch (ac-d_6)	1242	--	--	--	--	1033
$\nu_{18}(b_2)$	CH_3 rock	891	--	--	--	868	882
	CD_3 rock	724	--	--	--		704
$\nu_{19}(b_2)$	CO in-plane bend (ac-h_6)	530	--	--	--	366	350
	CO in-plane bend (ac-d_6)	475	--	--	340[g]	345	355
$\nu_{20}(b_1)$	CH_3-d-stretch	2972	--	--	--	--	3014
	CD_3-d-stretch	2227	--	--	--	--	2232
$\nu_{21}(b_1)$	CH_3-d-deform	1454	--	--	--	--	1424
	CD_3-d-deform	1050	--	--	--	--	1025
$\nu_{22}(b_1)$	CH_3 rock	1091	--	--	--	--	1032
	CD_3 rock	960	809[h]	--	--	723[i]	888
$\nu_{23}(b_1)$	CO out-of-plane bend (ac-h_6)	484	--	325/453	330/484	--	454
	CO out-of-plane bend (ac-d_6)	405	254[i]	282	279	278	383
$\nu_{24}(b_1)$	CH_3 torsion (out of phase)	124.5	175/215	129	--	--	116/125[d]
	CD_3 torsion (out of phase)	96	66[d]/132[i]	98.2[f]	100/96.0[f]	--	87

[a]Ref[150]; [b]Ref[130]; [c]Ref[127]; [d]Ref[136], [e]Ref[147]; [f]Ref [131]; [g]Present work; [h]Ref[134]; [i]Ref [133]; all values are in cm^{-1}.

Photoabsorption spectra of acetone-h$_6$ and acetone-d$_6$ in the region 50,000–80,000 cm^{-1} (6.2–9.9 eV) are shown in Fig. 4.3. The spectra of acetone-h$_6$ and acetone-d$_6$ observed in the present work are in good agreement with earlier works [123, 127, 129, 137, 151, 158]. There is sufficient evidence of hot band structure corresponding to the methyl torsional modes in the spectrum. The spectral analysis is divided into two parts for the ensuing discussion; (i) valence transitions in UV region and (ii) Rydberg series and vibronic transitions in the VUV region.

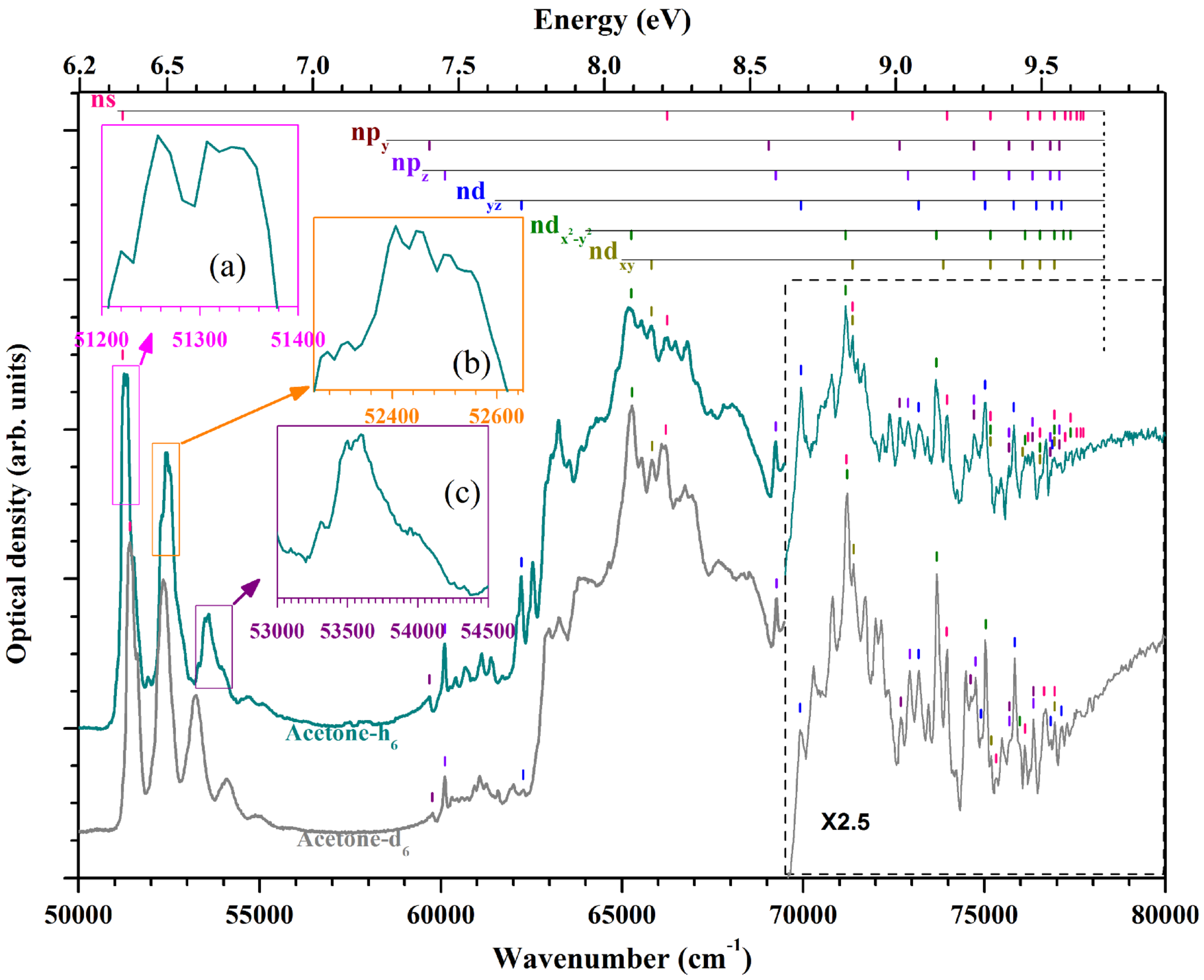

Figure 4.3: The VUV absorption spectra of acetone-h$_6$ and acetone-d$_6$ showing *ns*, *np* and *nd* Rydberg series converging to first *IP* at 9.708eV. The portion of the spectra in dotted box shows an expanded view with respect to y–axis. Expanded views of the region 51200–54500 cm^{-1} are shown in insets (a), (b) and (c).

4.3.1 Valence excited states

The first singlet excited state 1^1A_2 ($^1A''$) of acetone is dipole forbidden and corresponds to the *n→π** electronic transition. *Ab initio* studies show that the intensity for this transition is largely borrowed from the allowed $^1A_1 \rightarrow {}^1B_2$ (*n→3s*) transition due to vibronic coupling through the ν_{20}', ν_{22}' and ν_{23}' normal modes and to a lesser extent from the $^1A_1 \rightarrow {}^1B_1$ ($n \rightarrow 3d_{xy}$) transition through the ν_{19}' mode [179]. This vibronic coupling is reflected by a change in molecular symmetry from C_{2v} to C_s. Fluorescence studies by Baba *et al.* [142] have located the ν_{00} transition of this electronic system at 30435 cm^{-1} [142]. Spectra of acetone-h_6 and acetone-d_6 in UV region are similar showing a broad structureless hump, therefore only acetone-h_6 spectrum is shown in Fig. 4.4. Nobre *et al.* [123] have reported some discrete structures superimposed on the continuum, in the present spectrum no discrete features are discernible. However the overall absorption at high pressure appears to be composed of two overlapping absorption features as evident by the double maximum. A deconvolution of the observed peak into two Gaussians yields two peaks, one with high intensity and another with low intensity located at ~ 4.64 and 4.25 eV. Theoretical calculations by Mérchan *et al.* [129] predict two valence transitions in this region of which one is a singlet (1^1A_2) and the other is a triplet (1^3A_2), both corresponding to excitation of $n_y \rightarrow \pi^*$ observed earlier in electron impact studies [173] at 4.38 eV and 4.16 eV respectively. However, since the energy separation observed in the present work is considerably larger than the predicted difference between 1^1A_2 and 1^3A_2, therefore the weaker structure cannot be attributed to the triplet state. More sophisticated experimental techniques and higher level of theory would be required to resolve this issue. Higher valence states have not been directly observed so far in photoabsorption studies. However experimental and theoretical studies indicate that these states mix with Rydberg states through vibronic interactions giving rise to the observed anomalous intensities of the Rydberg states [129, 134].

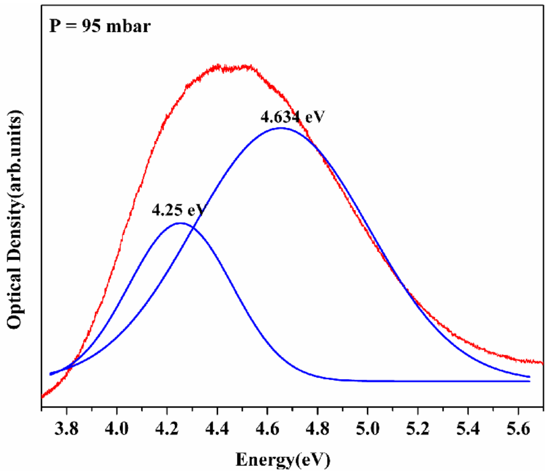

Figure 4.4: Photoabsorption spectrum of acetone-h_6 in UV region showing evidence of two overlapping peaks.

4.3.2 Rydberg series

In the energy region 6.2–9.9 eV (50,000–80,000 cm^{-1}) extensive Rydberg series converging to the lowest *IP* at 9.708 eV are observed (*cf.* Fig. 4.3). From molecular beam photoionization studies of acetone-h_6 and acetone-d_6, the experimentally measured first *IP* of acetone-d_6 is same as that of acetone-h_6 [160]. Rydberg series corresponding to *ns*, *np* and *nd* type are classified based on a quantum defect analysis using Eq. (1.1). From the selection rule $\Delta l = \pm 1$, transitions to *ns* and *nd* are expected to be relatively strong and transitions to *np* should be weak with the intensities of higher Rydberg series members expected to decrease as $1/n^3$ [128]. Although several works have reported detailed studies of 3*s*, 3*p* and 3*d* Rydberg states of acetone-h_6 and acetone-d_6 [123, 127, 129-136], quantum defect and vibronic analyses for Rydberg states of acetone-d_6 with $n \geq 4$ have not been reported earlier.

Accompanying vibrational excitations are observed for several of the lower Rydberg series members. Vibrational frequencies for a few totally symmetric and torsional modes in the excited electronic states 3*s*, $3p_x$, $3p_y$ and $3p_z$ have been measured by earlier workers [130, 133, 149, 151, 158, 159]. Vibrational frequencies in higher Rydberg states of the neutral molecule are expected to be closer to that of the ion. In the present analysis, measured values of frequencies in excited states or calculated ionic frequencies [127] are used as appropriate (*cf.* Table 4.1). For an allowed electronic transition, in the absence of vibronic coupling, only totally symmetric vibrations are expected to be excited with selection rules $\Delta v_i = \pm 1, \pm 2 ...$ However due to vibronic coupling, i.e. Herzberg-Teller effect, non-totally symmetric modes can also be excited with weaker intensities. Hot sequence bands like ν_{12} (1,1) and ν_{24} (1,1) must also be included. Dipole allowed vibronic transitions (for $\Delta v_i = \pm 1$) under the C_{2v} point group are given in Table 4.2.

Table 4.2: Electric dipole allowed (√) and forbidden (×) vibronic transitions

Symmetry of normal mode	**Symmetry of excited electronic state**			
	A_1 ($3p_y$, $3d_{yz}$)	**A_2 ($3p_x$)**	**B_1 ($3d_{xy}$)**	**B_2 ($3s$, $3p_z$, $3d_{x^2-y^2}$)**
$\nu_1 - \nu_8$ (a_1)	√	×	√	√
$\nu_9 - \nu_{12}$ (a_2)	×	√	√	√
$\nu_{13} - \nu_{19}$ (b_2)	√	√	×	√
$\nu_{20} - \nu_{24}$ (b_1)	√	√	√	×

A comparison of the observed Rydberg series origins (ν_{00}) of acetone-d_6 with those of acetone-h_6 is carried out using Eq. (1.2). If the excitation energy for a given transition is assumed to be same in acetone-h_6 and acetone-d_6, then the expected isotope shift is just the difference between the zero point energy differences in upper and lower states. Taking the lower state frequencies to be the known ground state frequencies [127, 134] and the upper state frequencies to be given approximately by the ionic frequencies for Rydberg states [127]. The difference in zero point energy between the excited and ground state is calculated to be about 479 cm^{-1} for acetone-h_6 and 567 cm^{-1} for acetone-d_6 respectively. This means that the origins of the acetone-d_6 electronic transitions are expected to be red shifted by about 88 cm^{-1}. Allowing for some error in determination of the upper state frequencies, nevertheless, one would expect a red shift of about 70 - 100 cm^{-1} for all Rydberg states, based on the above estimates. The experimental observations in the current work as well as by earlier authors [127, 191] indicate that the magnitude and sign of the isotope shift varies in an irregular manner. This means that either the excitation energies of both isotopic species are not the same, or that the assumption of ionic frequencies calculated based on an equilibrium C_{2V} geometry are not correct, and there is a non-negligible change in excited state geometry which varies from state to state. It is possible to predict the isotope shift for a given transition only if all normal mode frequencies for the excited state are known accurately. It may be noted that the frequencies of the torsional modes in acetone-d_6 are lower (53.4 and 96 cm^{-1}) than in acetone-h_6 (77.8 and 124.5 cm^{-1}) and hence the relative populations with respect to the ground state are expected to be greater in acetone-d_6 (~77% and 62%) as compared to acetone-h_6 (~70% and 55%). Consequently, similar to the room temperature absorption spectrum of acetone-h_6, the spectrum of acetone-d_6 is also expected to exhibit substantial contribution from hot bands due to the torsional modes.

4.3.2.1 Assignment of *ns* Rydberg series and accompanying vibronic structure

The *ns* Rydberg series is characterized by a quantum defect of ~0.98–1.10 (*cf.* Table 4.3). The highest members of the *ns* Rydberg series that can be distinguished clearly are n=15 and 10 for acetone-h_6 and acetone-d_6 respectively. For higher members i.e. n >15 in acetone-h_6 and 10 in acetone-d_6, overlap with other Rydberg series makes it difficult to make unambiguous assignments within the resolution used. This could be the reason why the work by Nobre *et al.* [123] for acetone-h_6 which is carried out at a similar resolution shows deviations in the calculated quantum defect for higher Rydberg series members. For example the 16*s* Rydberg state reported by them has a quantum defect of 0.684 which deviates sharply from the range of values expected for *ns* series.

The location of the origin of the 3*s* Rydberg transition of acetone-h_6 has been reported at various positions by different authors (51,203 cm^{-1} [133], 51,232 cm^{-1} [151], 51,268.9 cm^{-1} [136], 51,199 cm^{-1} [156], 51,204.5 cm^{-1} [157], 51,337 cm^{-1} [123]). The ambiguity is due to sequence band structure arising from population of the methyl torsional modes. In the present room temperature work, the band observed at 51,221 (51415) cm^{-1} is assigned to the ν_{00} of 3*s* transition of acetone-h_6 (acetone-d_6) in agreement with several earlier works [133, 151, 157], which supports a satisfactory assignment of the rest of the vibrational structure based on available upper state vibrational frequencies. The ν_{00} of 3*s* in acetone-d_6 is shifted by ~200 cm^{-1} to the higher wavenumber side as compared to acetone-h_6.

Table 4.3: Peak positions and quantum defects of *ns* Rydberg series

n	**Present study**				**Previous study for acetone-h_6 [123]**	
	Acetone-h_6		**Acetone-d_6**			
	position	**Q.D**	**position**	**Q.D**	**position**	**Q.D**
3	51,221	0.987	51,415	0.980	51,337	0.983
4	66,244	0.983	66,201*	0.988	66,291	0.977
5	71,364*	1.022	71,197*	1.070	71,299	1.041
6	73,964	0.969	73,963	0.970	73,880	1.017
7	75,237*	1.015	75,326	0.926	75,243	1.009
8	76,054*	1.010	76,119*	0.907	76,050	1.018
9	76,537*	1.111	76,635	0.882	76,566	1.045
10	76,927*	1.061	76,939*	1.022	76,953	0.974
11	77,226	0.893	--	--	77,187	1.071
12	77,380	1.080	--	--	77,429	0.776
13	77,549	0.914	--	--	77,591	0.566
14	77,658	0.929	--	--	77,671	0.793
15	77,728	1.152	--	--	77,752	0.855
16	--	--	--	--	77,833	0.684

*Denotes blended lines; Peak positions are in cm^{-1}; Q.D.=quantum defect value.

Vibronic assignments for the low lying *ns* series members are listed in Table 4.4 and 4.5. For acetone-h_6, Nobre *et al*. [123] assign all vibronic structure observed in the 6.3 to 6.9 eV region to a valence state whose symmetry is not specified, whereas the 3*s* Rydberg state is not assigned any vibrational structure by them. However, in their work the higher Rydberg series members like 4*s* and 5*s* have been assigned vibronic structure. While a few early works [136, 172] do refer to some ambiguity in the valence/Rydberg character of the transition at 6.35 eV, later theoretical [129] and experimental works [133, 136, 151] clearly conclude that this state is Rydberg in nature, arising from the promotion of a lone pair electron to the 3*s* Rydberg orbital giving rise to a $^1B_2$ state. In fact, theoretical calculations do not predict any valence state in this energy region, therefore it is concluded that all vibronic bands observed in this energy region belong to the 3*s* Rydberg state. A unique feature of the 3*s* transition is that there is a considerable energy gap between the 3*s* Rydberg state and the next higher members, therefore vibronic structure appearing with 3*s* can be clearly distinguished and is free from overlap with other transitions.

Table 4.4: Vibronic bands observed in the 3*s* Rydberg Transitions

Assignment	**Present Study**		**Previous study for acetone-h_6 [123]**	
	Observed position			
	Acetone-h_6	**Acetone-d_6**	**Position**	**Assignment**
3*s*	51,221	51,415	--	--
$3s + \nu_{12}' - \nu_{12}''$	51,260	--	51,256	ν_{00} (valence)
$3s + \nu_{12}'$	51,336	--	51,337	3*s*
$3s + \nu_8'$	51,527	51,615	--	--
$3s + \nu_7' - \nu_{12}''$	51,917	--	51,917	ν_7' (valence)
$3s + \nu_7'$	51,977	52,039	--	--
$3s + \nu_6'$	52,268	--	--	--
$3s + \nu_5' - \nu_{12}''$	52,311	--	52,305	ν_6' (valence)
$3s + \nu_5'$	52,407	52,345	52,409	ν_4' (valence)
$3s + \nu_4'$	52,451	--	--	--
$3\mathrm{s} + \nu_5' + \nu_{12}'$	52,505	--	--	--
--	--	--	52,749	$\nu_4' + \nu_8'$ (valence)?
--	--	--	53,071	$\nu_4' + \nu_7'$ (valence)
$3s + 2\nu_6'$	53,315	--	--	--
$3s + \nu_4' + \nu_6'$	53,495	53,196	53,474	$\nu_4' + \nu_6'$ (valence)
$3s + 2\nu_5'$	53,594	53,246	53,587	$2\nu_4'$(valence)
$3s + 2\nu_4' + \nu_8' - \nu_{12}''$	53,946	--	53,958	$2\nu_4' + \nu_8'$ (valence)?
$3s + 2\nu_4' + \nu_8'$	54,003(d)	--	--	--
$3s + \nu_1' - \nu_{12}''$	54,256(w)	--	54,281	$2\nu_4' + \nu_7'$ (valence)
$3s + \nu_1'$	54,329(w)	--	--	--
--	--	--	54,644	$2\nu_4' + \nu_6'$ (valence)
--	--	--	54,765	$3\nu_4'$ (valence)
--	--	--	55,128	$3\nu_4' + \nu_8'$ (valence)?
--	--	--	55,491	$3\nu_4' + \nu_7'$ (valence)

All values are in cm^{-1}; (d) and (w) denote weak and defuse peaks.

Vibrational modes excited in the 3*s* state of acetone-h_6 are ν_1', ν_4', ν_5', ν_6', ν_7' and ν_8' (*cf.* Table 4.4). Hot bands due to the torsional modes ν_{12}'' and ν_{24}'' are also seen along with a few overtones and combination bands of the above modes. The vibrational peaks accompanying the 3*s* state in acetone-h_6 and acetone-d_6 appear to be shifted non-uniformly. However, a detailed analysis shows that the shifts are consistent with the expected changes in vibrational frequencies in going from acetone-h_6 to acetone-d_6. As mentioned in section 4.1, vibrations involving the CH_3 groups are expected to be shifted considerably towards lower frequencies whereas other modes show relatively less shifts. For the 3*s* Rydberg state of acetone-d_6, hot band transitions involving the ν_{12}'' torsional mode are not resolved, probably due to the lower frequency of this mode in acetone-d_6 (53 cm^{-1}). The ν_4' and ν_6' modes are appeared as shoulders in acetone-d_6 and hence not included in the table. The broad weak feature at ~55,080 (54,880) cm^{-1} in acetone-h_6 (acetone-d_6) is left unassigned.

In the 4*s* state, excitation of the ν_3' vibration as well as a progression of ν_8' (up to $v'=6$ and 3) is observed in both acetone-h_6 and acetone-d_6 (*cf.* Table 4.5). Additionally, excitation of ν_4', ν_5' and ν_6' are also observed in acetone-h_6. Hot bands due to the torsional modes ν_{12}'' and ν_{24}'' are also seen along with a few overtones and combination bands of the above modes in both the species. In the 5*s* state, prominent bands are due to ν_8' and its overtones and excitation of $2\nu_{24}'$, ν_6' and ν_1' are consistently seen both in acetone-h_6 and acetone-d_6. It may be noted that the 5*s* vibronic assignments of Nobre *et al*. [123] for acetone-h_6 involving ν_{24}' (*cf.* Table 4.5) are likely to be in error, as odd quanta of vibrational excitations with b_1 symmetry would be forbidden in an electronic transition to a $^1B_2$ state. In the 6*s* state, excitation of a hot band involving $2\nu_{24}''$ and ν_6' is again seen in both acetone-h_6 and acetone-d_6. An additional excitation of $2\nu_{24}'$ is observed at 74,123 cm^{-1} in acetone-d_6. On the other hand, excitation of ν_{10}' in the 6*s* and 7*s* states observed in acetone-h_6 are not seen in acetone-d_6. Higher states ($n \geq 7$) in the *ns* series do not show any vibronic features.

Table 4.5: Vibronic bands observed in the 4*s*, 5*s* ,6*s* and 7*s* Rydberg Transitions

	Present Study		**Previous study for acetone-h$_6$ [123]**	
Assignment	**Observed position**			
	Acetone-h$_6$	**Acetone-d$_6$**	**Position**	**Assignment**
$4s$	66,244	66,201*	66,291	$4s$
$4s + \nu_8'$	66,572	66,483*	66,621	$4s + \nu_8'$
$4s+ 2\nu_8'- \nu_{12}''$	66,805*	--	--	--
$4s+ 2\nu_8'$	--	66,756*	66,871	$4s + 2\nu_8'$
$4s+ 3\nu_8'-2\nu_{12}''$	66,805	66,923	--	--
$4s+ 3\nu_8'- \nu_{24}''$	67,075*	--	67,186	$4s + 3\nu_8'$
$4s + \nu_6'$	67,256(s)	--	--	--
$4s + \nu_4'- \nu_{12}''/ \nu_5'$	67,398*	--	--	--
$4s + \nu_4'/4\nu_8'- \nu_{12}''$	67,463	--	--	--
$4s +\nu_3'- 2\nu_{12}''/ \nu_{16}'$	67,561	--	67,509	$4s + 4\nu_8'$
$4s + \nu_3'$	--	67,666	--	--
$4s+ 5\nu_8'- \nu_{12}''$	67,803	--	67,831	$4s + 5\nu_8'$
$4s+ 5\nu_8'$	67,864(s)	--	--	--
	--	--	67,936	$4s + 4\nu_8' + \nu_{19}'$
$4s+ 6\nu_8'- \nu_{24}''$	68,040*	--	--	--
$4s+ 6\nu_8'$	68,154(s)	--	68,154	$4s + 6\nu_8'$
$4s + 2\nu_6'$	68,306	--	--	
--	--	--	68,476	$4s +7\nu_8'$
--	--	--	71,299	$5s$
$5s$	71,364*	71,197*	--	--
--	--	--	71,509	†$5s + \nu_{24}'$
$5s+ 2\nu_{24}'$	71,588	71,374*	--	--
$5s+ \nu_8'$	71,682*	--	--	--
--	--	--	71,816	†$5s + \nu_{24}' + \nu'_8$
--	--	--	71,945	$5s + \nu_{24}' + \nu'_{19}$
$5s+2\ \nu_8'$	72,004*	71,702*	--	
--	--	--	72,106	†$5s + \nu_{24}' + 2\nu'_8$
--	--	--	72,332	†$5s + \nu_{24}' + 2\nu_{16}'$
$5s+ \nu_6'$	72,388*	71,995*	--	--
$5s+ 4\nu_8'/ \nu_5'$	72,659*	72,148*	72,541	$5s + \nu_{24}' + 2\nu'_8+ \nu'_{19}$
$6s -2\nu_{24}''$	73,718*	73,690	--	--
6s	73,964	--	73,880	$6s$
$6s +2\nu_{24}'$	--	74,123	--	--
$5s + \nu_1'$	74,461*	73,458*	--	--
$6s+ \nu_6'$	75,022	74,758*	--	--
$6s+ \nu_{10}'$	75,451	--	--	--
$7s$	75,237	--	--	--
$7s+ \nu_{10}'$	76,698*	--	--	--

All values are in cm^{-1}; †Forbidden by vibronic selection rules; * and (s) denotes blended and shoulder lines.

4.3.2.2 Assignments of *np* Rydberg series and accompanying vibronic structure

The 3*p* Rydberg series have been extensively studied earlier [13,21,27,28,34] for acetone-h_6. CASSCF calculations [129] predict the symmetries of the three 3*p* Rydberg transitions to be 2^1A_2 ($n_y \rightarrow 3p_x$), 2^1A_1 ($n_y \rightarrow 3p_y$) and 2^1B_2 ($n_y \rightarrow 3p_z$). The theoretically predicted symmetries and energies are well corroborated by experiments [127, 129, 162], establishing the ν_{00} transitions of the $3p_x$, $3p_y$ and $3p_z$ series to be at 7.36, 7.41 and 7.45 eV respectively. The $3p_x$ ($^1A_2$) Rydberg transition is dipole forbidden and is not expected to appear in the photoabsorption spectra. For acetone-h_6, Nobre *et al.* [123] have attributed a few absorption peaks to vibrational structure accompanying the $3p_x$ transition. In this case only modes of a_2, b_1 or b_2 symmetry would be allowed by vibronic selection rules. In view of this, the assignments of Nobre *et al.* which are attributed to the dipole forbidden ν_4 (a_1) mode are doubtful. In the present study only the np_y and np_z Rydberg series are observed for both species with quantum defects in the range ~ 0.43 to 0.57 as listed in Tables 4.6 and 4.7 respectively. The oscillator strength of the $3p_y$ state is predicted to be an order lower than that of the $3p_z$ state, and both 3*p* states are expected to have considerably lower intensities than the 3*s* state [129]. As seen from Fig. 4.2, the assignment of the features at 59,695 cm^{-1} and 60,107 cm^{-1} (59,764 cm^{-1} and 60,113 cm^{-1}) to the ν_{00} bands of $3p_y$ and $3p_z$ of acetone-h_6 (acetone-d_6) are consistent with this prediction.

The highest principal quantum number observed for np_y and np_z series is *n*=10 for acetone-h_6 and *n*=8 for acetone-d_6 (*cf.* Tables 4.6 and 4.7). Comparing *np* series of acetone-d_6 with acetone-h_6, the $3p_y$ state is blue shifted by ~ 75 cm^{-1}, whereas all higher np_y states and all np_z states including the $3p_z$ state are shifted by very small amounts (< 50 cm^{-1}). Moreover, the electronic origin of the $3p_y$ state is considerably broadened and is lower in intensity than $3p_z$, both in acetone-h_6 and acetone-d_6. This has been explained convincingly by ter Steege *et al.* [127] as arising due to vibronic coupling of the

$3p_y$ ($^1A_1$) state with the short lived $\pi\pi^*$ (A_1) valence state and the vibronic level $3p_x + \nu_8' + \nu_{12}'$. In contrast, the origin of the $3p_z$ transition is sharp as expected for an unperturbed Rydberg state. For $n > 6$, the two components of the np_y and np_z series are not resolved in the present experiment and the two series merge into a single one. The highest principal quantum number observed is 10. Higher np_y transitions are generally observed to be weaker than the corresponding np_z transitions. Nobre *et al*. [123] have reported the np_y series up to n=10, and the np_z series up to n=16. However there seems to be some discrepancy in the np_z series assignments, as they have not observed n=14 and n=15, but have nevertheless assigned the band at 9.652 eV to n=16. Moreover it is somewhat surprising that they could distinguish the 16*s* band at 9.65 eV from the $16p_z$ band at 9.652 eV with their stated resolution of 6 meV at 10 eV. There is no prior literature on the isotopic shifts and relative intensities for higher *np* Rydberg states.

Assignments of the vibrational bands accompanying the np_y and np_z Rydberg states are listed in Tables 4.8 and 4.9 respectively. Fig. 4.5–4.7 show some of the vibronic assignments. In both species, the $3p_y + \nu_{19}'$ band is not clearly resolved as its expected position coincides with the rapidly rising part of $3p_z$. Several overtones of the ν_{19}' mode are however observed clearly. While Nobre *et al*. [123] also assign several peaks to overtones of ν_{19}' in acetone-h_6, the measured frequency shows a large variation in the range of 400–480 cm^{-1}. In the present assignment, the measured spacing between successive overtones of acetone-h_6 is almost constant with a value of ~350–360 cm^{-1}. Although there is no earlier measured value of ν_{19}' in the $3p_y$ state available for comparison, the calculated value of ionic frequency of ν_{19}' and measured value of ν_{19}' in the $3p_z$ state are in this range (*cf.* Table 4.1) [127]. Further, on the basis of the extensive progressions observed, it is concluded that the frequency of this mode in the $3p_y$ state for acetone-h_6 and acetone-d_6 is ~350 and 340 cm^{-1} respectively which are close to corresponding ionic frequencies.

Table 4.6: Peak positions and quantum defects of *np*$_y$ Rydberg series

n	Present study				Previous study for acetone-h$_6$ [123]	
	acetone-h$_6$		acetone-d$_6$			
	position	Q.D	position	Q.D	position	Q.D
3	59,688	0.572	59,764	0.567	59,685	0.572
4	69,045	0.557	69,097	0.547	68,960	0.572
5	72,710	0.569	72,694*	0.576	72,832	0.520
6	74,646	0.520	74,610	0.547	74,606	0.550
7	75,682*	0.526	75,689*	0.517	75,671	0.540
8	76,326*	0.556	76,354*	0.491	76,300	0.593
9	76,815*	0.404	--	--	76,776	0.515
10	77,068*	0.563	--	--	77,107	0.412

Peak positions values are in cm^{-1}; *Denotes blended lines; Q.D.=quantum defect value.

Table 4.7: Peak positions and quantum defects of *np*$_z$ Rydberg series

n	Present study				Previous study for acetone-h$_6$ [123]	
	acetone-h$_6$		acetone-d$_6$			
	position	Q.D	position	Q.D	position	Q.D
3	60,105	0.544	60,113*	0.544	60,121	0.543
4	69,241	0.520	69,264	0.515	69,348	0.499
5	72,900	0.492	72,941*	0.475	72,856	0.510
6	74,715	0.468	74,758*	0.434	74,679	0.495
7	75,682*	0.526	75,689*	0.517	75,703	0.500
8	76,326*	0.556	76,354*	0.491	76,365	0.471
9	76,815*	0.404	--	--	76,776	0.515
10	77,068*	0.563	--	--	77,107	0.412
11	--	--	--	--	77,308	0.483
12	--	--	--	--	77,510	0.217
13	--	--	--	--	77,607	0.422

Peak positions values are in cm^{-1}; *Denotes blended lines; Q.D.=quantum defect value.

The value of ν_2' in the 3p_y state for acetone-h$_6$ has been taken as ~2541cm^{-1} in the work of Nobre *et al.* [123]. This band is observed at ~2440 cm^{-1} in present work, in agreement with the experimentally measured value of 2424 cm^{-1} [130]. For the ν_4' mode on the other hand no prior measurements exist in the 3p_y state, however the frequency of this mode has been measured to be ~1367–1395 cm^{-1} in the $3p_x$ and $3p_z$ states (*cf.* Table 4.1). The ν_4' excitation is observed at ~1370 cm^{-1} in the present work which is consistent with the earlier reported measurements of this mode [127]. Other modes observed along with the np_y series are the totally symmetric modes ν_2', ν_3', ν_6' and ν_7' and $2\nu_{23}'$ for acetone-h_6 and $\nu_2'+\nu_8'$ for acetone-d_6.

Here, it should be noted that within the Born-Oppenheimer approximation, only vibrations which belong to the totally symmetric species (a_1) are expected, and the observation of a non-totally symmetric vibration is due to vibronic coupling of the $3p_y$ ($^1A_1$) and $3p_z$ ($^1B_2$) states as pointed out in the photoelectron spectroscopy study by ter Steege *et al.* [127]. Excitation of the ν_2' mode (CH stretch) implies an appreciable change in the CH bond length in the excited state. This coupled with the drastic reduction of the ν_2' frequency compared to its ground state value is at odds with the excitation of the non bonding oxygen lone pair electron and also indicates a strong coupling with the $\pi\pi^*$ valence state. As can be seen from Table 4.8, vibronic assignments of all members of the np_y series for acetone-d_6 are in excellent agreement with corresponding assignments in acetone-h_6. It may be noted that the transitions $8p_y + \nu_{19}'$ and $6p_y + 2\nu_6'$ which are appeared at the same position (76,698 cm^{-1}) in acetone-h_6 are separated out into two peaks at 76,354 and 76,681 cm^{-1} in acetone-d_6.

Vibronic assignments in the np_z series, some of which are marked in Figs. 4.5 - 4.7 are given in Table 4.9. Progressions involving the totally symmetric vibration ν_8' are observed along with $3p_z$, $4p_z$ and $5p_z$ in both acetone-h_6 and acetone-d_6. Assignments for acetone-h_6 are in overall agreement with the observations of Nobre *et al.* [123]. In addition several observed bands that arise due to the ground state torsional modes are accordingly assigned as hot bands. An extensive progression involving ν_{19}' is identified in the $4p_z$ transition. Other modes excited in the np_z series are ν_1', ν_2', ν_5', ν_6', and ν_7'. All vibronic assignments in the np_z series for acetone-h_6 are observed with the expected isotopic shifts in acetone-d_6, thus confirming their validity.

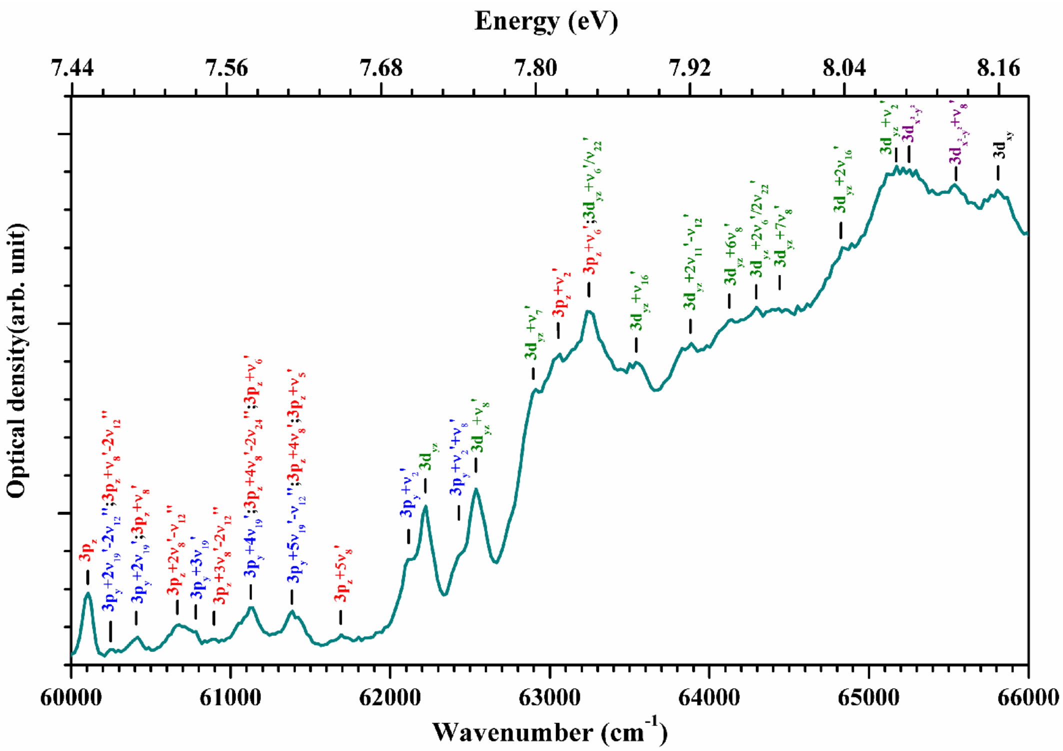

Figure 4.5: VUV photoabsorption spectrum of Acetone-h_6 in the region of the 3*p* and 3*d* Rydberg states. Vibronic assignments of the prominent bands are marked.

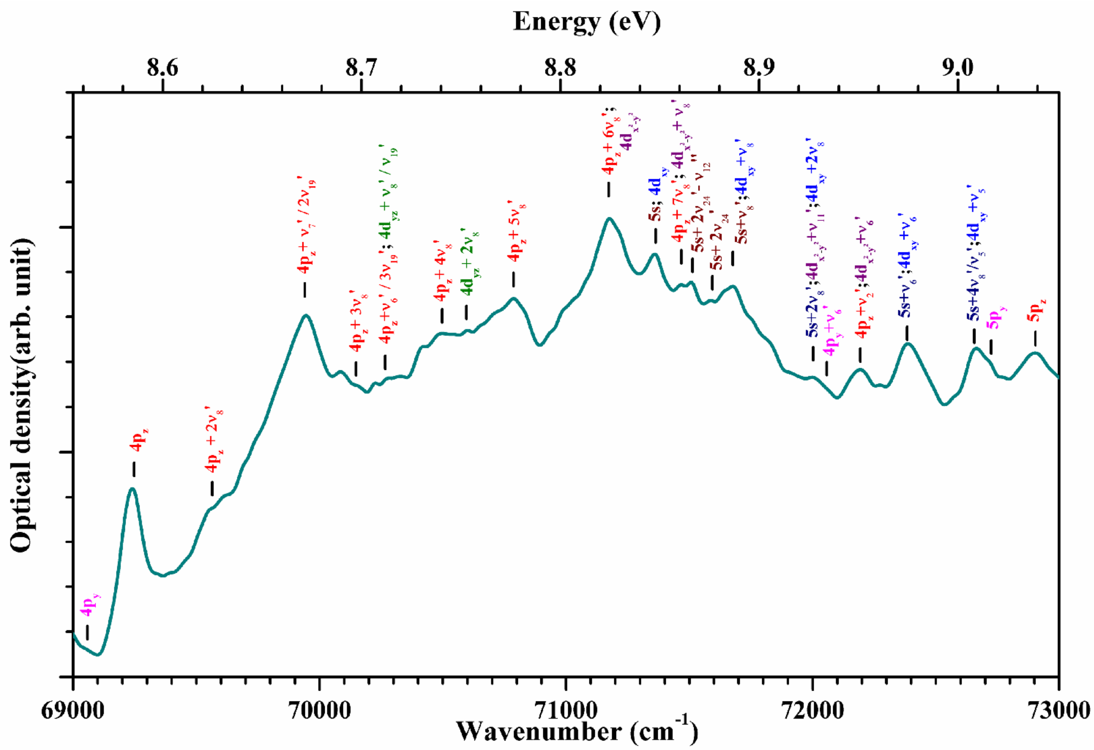

Figure 4.6: VUV photoabsorption spectrum of Acetone-h_6 in the region of the 5*s*, 4*p*, 4*d*, 5*p* and 5*d* Rydberg states. Vibronic assignments of the prominent bands are marked.

Table 4.8: Vibronic bands observed in the $3p_y$, $4p_y$, $5p_y$ and $6p_y$ Rydberg transitions

Present Study			**Previous study for acetone-h$_6$**			
Assignment	**Position**		**Ref. [123]**		**Ref. [130]$^{\#}$**	
	Acetone-h$_6$	**Acetone-d$_6$**	**Position**	**Assignment**	**Position**	**Assignment**
$3p_y$	59,688	59,764	59,685	$3p_y$	59,769	$3p_y$
--	--	--	60,008	$3p_y+\nu_8'$	--	--
$3p_y+\nu_{19}'$	--	60,113*	60,120	$3p_y+\nu_{19}'$	60,100	$3p_y+\nu_8'$
$3p_y+2\nu_{19}'-2\nu_{12}''$	60,252*	60,319*	60,258	$3p_y+2\nu_8'$	--	--
$3p_y+2\nu_{19}'$	60,410*	60,444*	--	--	60,419	$3p_y+2\nu_8'$
--	--	--	60,572	$3p_y+3\nu_8'/2\nu_{19}'$	--	--
$3p_y+3\nu_{19}'$	60,775	60,741*	--	--	60,759	$3p_y+3\nu_8'$
--	--	--	--	--	60,833	$3p_y+\nu_6'$
--	--	--	60,903	$3p_y+4\nu_8'/\nu_4'$	--	--
--	--	--	61,056	$3p_y+3\nu_{19}'$	61,078	$3p_y+\nu_5'$
$3p_y+4\nu_{19}'$	61,127*	61,089*	--	--		
--	--	--	--	--	61,382	$3p_y+\nu_6'+2\nu_8'$
$3p_y+5\nu_{19}'-\nu_{12}''$	61,382(s)	--	--	--	--	--
--	--	--	61,459	$3p_y+4\nu_{19}'$	--	--
--	--	--	61,879	$3p_y+5\nu_{19}'$	--	--
$3p_y+\nu_2'$	62,128	61,574	62,153	$3p_y+2\nu_4'$	--	--
--	--	--	62,226	$3p_y+\nu_2'$	62,193	$3p_y+\nu_2'$
$3p_y+\nu_2'+\nu_8'$	62,446(s)	61,927	--	--	--	--
--	--	--	62,556	$3p_y+\nu_2'+\nu_8'$	62,517	$3p_y+\nu_2'+\nu_8'$
--	--	--	--	--	62,897	$3p_y+\nu_1'$
--	--	--	63,395	$3p_y+3\nu_4'$	--	--
--	--	--	68,960	$4p_y$	--	--
$4p_y$	69,045	69,097	--	--	--	--
--	--	--	69,928	$4p_y+\nu_6'$	--	--
$4p_y+\nu_6'$	70,082	69,911*	--	--	--	--
--	--	--	70,896	$4p_y+2\nu_6'$	--	--
--	--	--	71,945	$4p_y+3\nu_6'$	--	--
$5p_y$	72,710(s)	--	71,832	$5p_y$	--	--
$5p_y+2\nu_{23}'$	73,661*	--	--	--	--	--
$6p_y$	74,646(s)	74,610	74,606	$6p_y$	--	--
$6p_y+\nu_7'$	75,331	75,326	--	--	--	--
$6p_y+\nu_6'$	75,682*	75,487	75,671	$7p_y$	--	--
$6p_y+\nu_3'$	76,207	76,119*	--	--	--	--
$8p_y$	76,320*	--	76,300	$8p_y$	--	--
$6p_y+2\nu_6'$	76,698*	76,354*	--	--	--	--
$8p_y+\nu_{19}'$; $6p_y+2\nu_6'$	76,698*	76,681	--	--	--	--

All values are in cm^{-1}; $^{\#}$ REMPI study of jet cooled sample; * and (s) denotes blended and shoulder lines.

Table 4.9: Vibronic bands observed in the $3p_z$, $4p_z$, $5p_z$ and $6p_z$ Rydberg Transitions

Present Study			**Previous study for acetone-h$_6$**			
Assignment	**Position**		**Ref.[123]**		**Ref.[130]$^{\#}$**	
	Acetone-h$_6$	**Acetone-d$_6$**	**Position**	**Assignment**	**Position**	**Assignment**
$3p_z$	60,105	60113*	60,120	$3p_z$	60,100	$3p_z$
$3p_z+\nu_8'-2\nu_{12}''$	60,252*	60319*	--	--	--	--
$3p_z+\nu_8'$	60,410*	60444*	60,419	$3p_z+\nu_8'$	60,410	$3p_z+\nu_8'$
$3p_z+2\nu_8'-\nu_{12}''$	60,674	60617	--	--	--	--
$3p_z+2\nu_8'$	--	60741*	60,750	$3p_z+2\nu_8'$	60,733	$3p_z+2\nu_8'$
--	--	--	--	--	60,833	$3p_z+\nu_7'$
$3p_z+3\nu_8'-2\nu_{12}''/\nu_6'-2\nu_{24}''$	60,891	--	--	--	--	--
--	--	--	61,056	$3p_z+3\nu_8'$	--	--
$3p_z+\nu_6'/4\nu_8'-2\nu_{24}''$	61,127*	60,925	61,145	$3p_z+\nu_6'$	61,078	$3p_z+\nu_6'$
$3p_z+\nu_5'$	61,382*	61,089*	--	$3p_z+\nu_4'$	--	--
$3p_z+3\nu_8'$	--	61,089*	--	--	--	--
$3p_z+4\nu_8'$	61,382*	61,262	61,387	$3p_z+4\nu_8'$	61,372	$3p_z+\nu_5'$
$3p_z+5\nu_8'$	61,693	--	61,726	$3p_z+5\nu_8'$	--	--
$3p_z+2\nu_5'$	--	62,007	62,153	$3p_z+2\nu_6'$	--	--
$3p_z+\nu_2'$	63,060	--	--	--	--	--
$3p_z+\nu_1'$	63,250*	--	--	--	63,248	$3p_z+\nu_1'$
--	--	--	63,798	$3p_z+3\nu_4'$	--	--
$3p_z+2\nu_1'$	66,426	--	--	--	--	--
$4p_z$	69,241	69,264	--	--	--	--
$4p_z+\nu_8'$	--	69,537	69,348	$4p_z$	--	--
$4p_z+\nu_{19}'$	--	69,601	69,686	$4p_z+\nu_8'$	--	--
$4p_z+2\nu_8'$	69,560	--	--	--	--	--
$4p_z+\nu_7'/2\nu_{19}'$	69,943*	69,911*	69,928	$4p_z+2\nu_8'$	--	--
	--	--	70,049	$4p_z+\nu_8'+\nu_{19}'$	--	--
$4p_z+3\nu_8'$	70,145	--	70,170	$4p_z+3\nu_8'$	--	--
$4p_z+3\nu_{19}'$	70,271*	70,290*	--	--	--	--
$4p_z+\nu_6'$	70,271*	--	--	--	--	--
$4p_z+4\nu_8'$	70,503	--	70,493	$4p_z+4\nu_8'$	--	--
$4p_z+5\nu_8'$	70,788	--	70,815	$4p_z+5\nu_8'$	--	--
$4p_z+6\nu_8'$	71,174*	--	71,138	$4p_z+6\nu_8'$	--	--
$4p_z+7\nu_8'$	71,482*	71,197*	--	--	--	--
$4p_z+\nu_2'$	72,193*	71,374*	--	--	--	--
$4p_z+7\nu_{19}'$	--	71,702*	--	--	--	--
$4p_z+8\nu_{19}'$	--	71,995*	--	--	--	--
$4p_z+9\nu_{19}'$	--	72,355*	--	--	--	--
$4p_z+10\nu_{19}'$	--	72,694*	--	--	--	--
$5p_z$	72,900	72,941*	72,856	$5p_z$	--	--
--	--	--	73,074	†$5p_z+\nu_{24}'$	--	--
$5p_z+\nu_8'$	73,218*	73,185*	--	--	--	--
$5p_z+2\nu_8'$	--	73,458*	--	--	--	--
$5p_z+\nu_7'$	73661*	73,690*	--	--	--	--

All values are in cm^{-1}; $^{\#}$ REMPI study of jet cooled sample; *denotes blended lines; †Forbidden by vibronic selection rules.

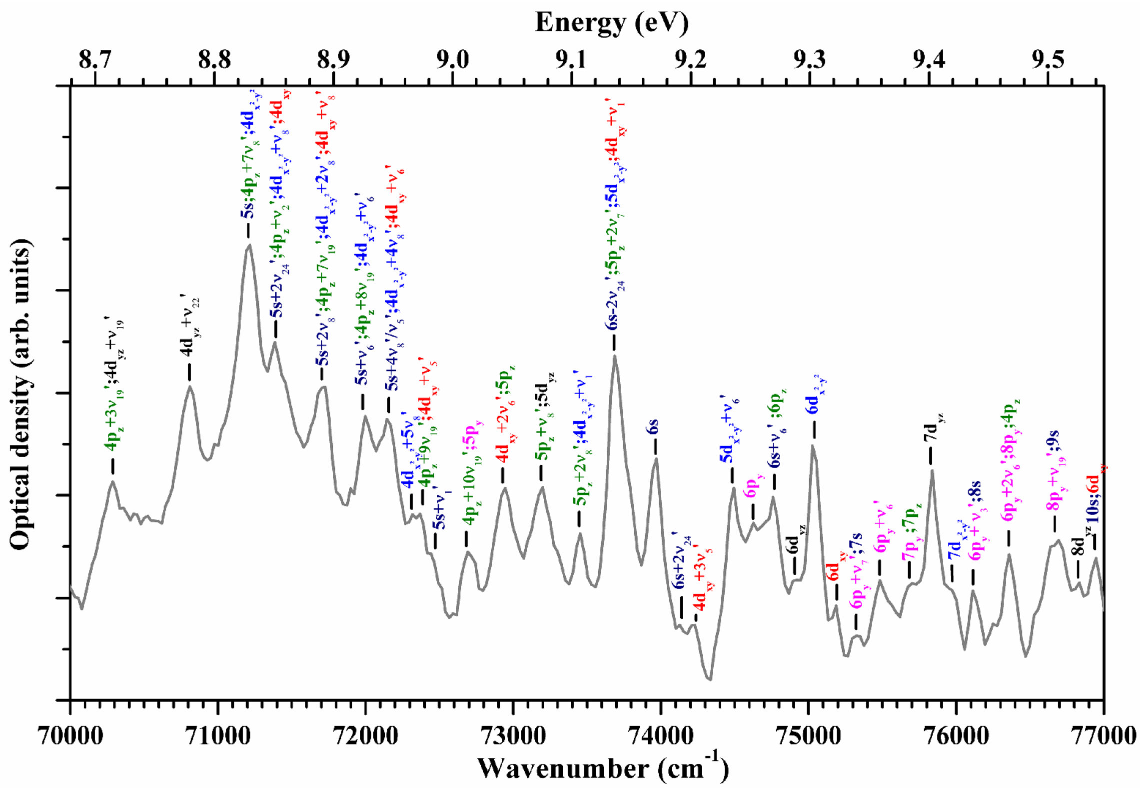

Figure 4.7: VUV photoabsorption spectrum of acetone-d_6 in region 70,000–77,000 cm^{-1} showing vibronic assignments.

4.3.2.3 Assignments of *nd* Rydberg series and accompanying vibronic structure

The *nd* Rydberg series origins have been reported by ter Steege *et al*. [127] up to n=7 and Nobre *et al*. [123] up to n =10 for acetone-h_6. In case of acetone-d_6 there is very little prior literature available [129]. In this energy region (> 62,500 cm^{-1}) the absorption signals increase drastically and the n >3 members of the *np* series overlap with the *nd* series. Theoretical calculations [129, 185] predict that of the five possible components of the *3d* Rydberg state ($^1A_1$ $3d_{yz}$, $^1B_2$ $3d_{x^2-y^2}$, $^1A_2$ $3d_{xz}$, $^1B_2$ $3d_{z^2}$ and $^1B_1$ $3d_{xy}$), $3d_{xz}$ is forbidden and $3d_{z^2}$ has very low oscillator strength. Consequently, only three series should be observed. Of these only two have been observed by earlier workers [127, 129] whereas Nobre *et al*. [123] have reported all three. A possible reason could be that the earlier works were carried out using the REMPI technique which detects only those states which live long enough to absorb additional photons for ionization [129]. Thus the short lived diffuse state ($^1A_1$ $3d_{yz}$) was not detected. In the present work, all three series components are observed and listed in Table 4.10–4.12. While the overall spectral features are in good agreement with earlier work [123], the vibronic analysis of *nd* states is further investigated and assignments are consolidated with the help of comparisons between the vibronic structure of acetone-h_6 and acetone-d_6.

Table 4.10: Peak positions and quantum defects of nd_{yz} Rydberg series

n	**Present study**				**Previous study for acetone-h_6 [123]**	
	acetone-h_6		**acetone-d_6**			
	position	**Q.D**	**position**	**Q.D**	**position**	**Q.D**
3	62,224	0.387	62,272	0.383	62,226	0.387
4	69,943*	0.376	69,911*	0.383	70,170	0.326
5	73,190	0.366	73,185*	0.368	73,397	0.269
6	74,909	0.312	74,909	0.312	74,937	0.288
7	75,816	0.354	75,839	0.323	75,905	0.232
8	--	--	--	--	76,453	0.292
9	--	--	76,827	0.370	76,865	0.257
10	--	--	77,124	0.342	77,107	0.412

Peak positions are in cm^{-1}; *Denotes blended lines; Q.D.=quantum defect value.

Table 4.11: Peak positions and quantum defects of $nd_{x^2-y^2}$ Rydberg series

n	**Present study**				**Previous study for acetone-h_6 Ref.[123]**	
	acetone-h_6		**acetone-d_6**			
	position	**Q.D**	**position**	**Q.D**	**position**	**Q.D**
3	65,255	0.100	65,272	0.098	65,250	0.100
4	71,174*	0.079	71,197*	0.070	71,146	0.084
5	73,718*	0.106	73,690*	0.121	73,719	0.106
6	75,168	0.081	75,039	0.199	75,171	0.078
7	--	--	75,955	0.160	75,977	0.127
8	76,537*	0.111	--	--	76,542	0.100
9	76,922*	0.077	--	--	76,921	0.080
10	--	--	--	--	77,187	0.071
11	77,378	0.092	--	--	77,373	0.123

Peak positions are in cm^{-1}; *Denotes blended lines; Q.D.=quantum defect value.

Table 4.12: Peak positions and quantum defects of nd_{xy} Rydberg series

n	Present study				Previous study for acetone-h$_6$ Ref.[123]	
	acetone-h$_6$		acetone-d$_6$			
	position	Q.D	position	Q.D	position	Q.D
3	65,810	0.036	65,832*	0.033	65,855	0.031
4	71,364*	0.022	71,374*	0.020	71,299	0.041
5	--	--	--	--	73,856	0.031
6	75,237*	0.015	75,187	0.063	75,252	0.001
7	76,050	0.017	--	--	76,050	0.017
8	76,570	0.036	--	--	76,566	0.045
9	76,935	0.035	76,939*	0.022	76,921	0.080
10	--	--	--	--	77,187	0.071

Peak positions are in cm^{-1}; *Denotes blended lines; Q.D.=quantum defect value.

Note that the expected relative intensity is predicted to go as I ($3d_{yz}$) > I ($3d_{x^2-y^2}$) > I ($3d_{xy}$) with approximate ratio 18:3:1. In the photoabsorption spectrum however, the intensities of $3d_{xy}$ and $3d_{x^2-y^2}$ are comparable and are much higher than that of $3d_{yz}$. This anomalous intensity pattern has been explained by Mérchan *et al.* [129] as arising due to a mixing between the ($^1A_1$) $3d_{yz}$ Rydberg state and the hitherto unobserved ($^1A_1$) π–π^* valence state [129]. Ter Steege *et al.* [127] have also pointed out that this vibronic coupling may be responsible for loss of intensity of Rydberg states of A_1 symmetry. In the present study, it is observed that this anomaly appears to be maximum for the n=3 states, while intensities of all the three 4*d* components are almost equal. It may be mentioned here that consequent to the present work, a recent theoretical study on excited states of acetone has been reported using molecular quantum defect method [185]. Oscillator strengths reported by them for the 3*d* states are in good agreement with present experimental studies. For higher *nd* series members, a comparison between observed intensities and calculated oscillator strengths cannot be made as there is a lot of overlap between the various electronic and vibronic transitions.

As seen from Tables 4.10 - 4.12, the highest principal quantum number observed is n=10, 11 and 9 for Rydberg series nd_{yz}, $nd_{x^2-y^2}$ and nd_{xy} respectively. The nd Rydberg series are characterized by average quantum defects of 0.35 (nd_{yz}), 0.13 ($nd_{x^2-y^2}$) and 0.03 (nd_{xy}). Quantum defects for acetone and deuteroacetone are almost constant through a series with a given orbital angular momentum, as expected, except for some minor deviations in $nd_{x^2-y^2}$ and nd_{xy}. In the nd_{xy} series, the quantum defect reduces from a value of 0.035 for $3d_{xy}$ till it reaches a value of 0.015 for n = 6 after which it again increases to ~ 0.035. This is in contrast to the earlier work by Nobre *et al.* [123] (*cf.* Table 4.11 and 4.12) in which the variation in quantum defect over the series is quite large. Further understanding of these anomalies would benefit from complementary techniques like high resolution photoelectron spectroscopy.

The unusually large quantum defect of ~0.4 for the nd_{yz} series has been discussed extensively for the analogous molecule formaldehyde [170, 192]. The assignment of these tranistions to a d series rather than a p series is however well established, and the large quantum defect is attributed to a high degree of interaction of the Rydberg orbital with the molecular core [192]. In the nd_{xy} series of acetone-d$_6$, the quantum defect values are observed to vary with n in an oscillatory manner. However in the case of acetone-h$_6$, the quantum defect is seen to decrease systematically till n = 6 and then again increase with n. A few members are observed clearly in one of species but not in the other, possibly due to blending with other bands and limitations imposed by experimental resolution. However the expected positions of these transitions are marked in Fig. 4.2. In this context it should be pointed out that the assignment by Nobre *et al.* of the band at 9.76 eV to $37d_{x^2-y^2}$ of acetone-h$_6$ is certainly incorrect, as their stated experimental resolution of 6 meV would succeed in just resolving the $16d_{x^2-y^2}$ and $17d_{x^2-y^2}$ transitions. From comparison of spectra of acetone-h$_6$ and acetone-d_6, very small shifts are observed in the *nd* Rydberg series except for the $6d_{x^2-y^2}$ transition which is red shifted by ~130 cm^{-1}.

Vibronic assignments for the nd_{yz}, $nd_{x^2-y^2}$ and nd_{xy} series are listed in Tables 4.13 – 4.15 and some of the assignments are marked in Figs. 4.5 - 4.7. Vibrational structure is observed mainly for *n*=3 and 4 in all three *d* series except for $5d_{x^2-y^2}+\nu_6'$ **o**f acetone-d_6. Note that the band at 9.22 eV assigned by Nobre *et al.* (*cf.* Table 4.15) to $5d_{xy}+\nu_{19}'$ of acetone-h_6 is vibronically forbidden. Moreover, the frequency of ν_{19}' in the Rydberg state is likely to be reduced from its ground state value, hence this assignment is doubtful.

Table 4.13: Vibronic bands observed in the $3d_{yz}$ and $4d_{yz}$ Rydberg transitions

	Present Study		**Previous study for acetone-h$_6$ [123]**	
Assignment	**Position**			
	Acetone-h$_6$	**Acetone-d$_6$**	**Position**	**Assignment**
$3d_{yz}$	62,224	62,272	62,226	$3d_{yz}$
$3d_{yz}+\nu_8'$	62,539	--	62,556	$3d_{yz}+\nu_8'$
$3d_{yz}+\nu_7'$	62,911	--	62,935	$3d_{yz}+2\nu_8'$
$3d_{yz}+\nu_{11}'$	63,060	--	--	--
$3d_{yz}+\nu_6'-\nu_{12}''$	--	62,986	--	--
$3d_{yz}+\nu_6'$	63,250*	--	63,274	$3d_{yz}+3\nu_8'$
$3d_{yz}+\nu_{16}'$	63,520	63,244	63,476	$3d_{yz}+\nu_4'$
$3d_{yz}+2\nu_6''-2\nu_{12}''$	--	63,706	63,597	$3d_{yz}+4\nu_8'$
$3d_{yz}+2\nu_{11}'-\nu_{12}''$	63,888	--	63,895	$3d_{yz}+5\nu_8'$
$3d_{yz}+6\nu_8'$	64,140	--	64,202	$3d_{yz}+6\nu_8'$
$3d_{yz}+2\nu_6'$	64,298	63,812	--	--
$3d_{yz}+7\nu_8'$	64,444	--	64,516	$3d_{yz}+7\nu_8'$
$3d_{yz}+3\nu_6'$	--	64,629	64,686	$3d_{yz}+2\nu_4'$
$3d_{yz}+2\nu_{16}'$	64,864	--	64,766	$3d_{yz}+\nu_2'$
$3d_{yz}+\nu_2'$	65,173	--	--	--
$4d_{yz}$	69,943*	69,911*	70,170	$4d_{yz}$
$4d_{yz}+\nu_{19}'/\nu_8'$	70,271*	70,290*	--	--
$4d_{yz}+2\nu_8'$	70,576	--	70,654	$4d_{yz}+\nu_{19}'$
$4d_{yz}+\nu_{22}'$	--	70,812$^{\#}$	--	--
$4d_{yz}+4\nu_{19}'$	--	71,374*	--	--
$4d_{yz}+5\nu_{19}'$	--	71,702*	71,630	$4d_{yz}+\nu_{19}'+\nu_6'$

All values are in cm^{-1}. *Denotes blended lines.

Table 4.14: Vibronic bands observed in the $3d_{x^2-y^2}$ and $4d_{x^2-y^2}$ Rydberg transitions

Assignment	Present Study		Previous study for acetone-h$_6$ [123]	
	Position			
	Acetone-h$_6$	Acetone-d$_6$	Position	Assignment
$3d_{x^2-y^2}$	65,255#	65,272	65,250	$3d_{x^2-y^2}$
$3d_{x^2-y^2} + \nu_8'$	65,553	65,535	65,597	$3d_{x^2-y^2} + \nu_8'$
$3d_{x^2-y^2} + 2\nu_8'$	--	65,832*	65,855	$3d_{x^2-y^2} + 2\nu_8'$
$3d_{x^2-y^2} + 3\nu_8'$	66,186	--	66,137	$3d_{x^2-y^2} + 3\nu_8'$
--	--	--	66,291	$3d_{x^2-y^2} + \nu_6'$
$3d_{x^2-y^2} + 4\nu_8'$	66,471*	66,201*	66,508	$3d_{x^2-y^2} + 4\nu_8'$
$3d_{x^2-y^2} + \nu_3'/\ 5\nu_8'$	66,805*	66,756*	66,823	$3d_{x^2-y^2} + 5\nu_8'$
$3d_{x^2-y^2} + 6\nu_8'$	67,138(s)	--	67,138	$3d_{x^2-y^2} + 6\nu_8'$
$3d_{x^2-y^2} + \nu_1'$	68,330	--	--	--
$3d_{x^2-y^2} + 2\nu_3'$	--	68,374	--	--
$4d_{x^2-y^2}$	71,174*	71,197*	71,146	$4d_{x^2-y^2}$
$4d_{x^2-y^2} + \nu_8'$	71,482*	71,374*	--	--
$4d_{x^2-y^2} + 2\nu_8'$	--	71,702*	--	--
$4d_{x^2-y^2} + 4\nu_8'$	--	72,148*	--	--
$4d_{x^2-y^2} + \nu_{11}'$	72,004*	--	--	--
$4d_{x^2-y^2} + \nu_6'$	72,193*	71,995*	--	--
$4d_{x^2-y^2} + 5\nu_8'$	--	72,355*	--	--
$5d_{x^2-y^2}$	73,718*	73,458*	73,719	$5d_{x^2-y^2}$
$4d_{x^2-y^2} + \nu_1'$	74,250	74,250	--	--
$5d_{x^2-y^2} + \nu_6'$	--	74,492	--	--

All values are in cm^{-1}; *denotes blended lines; #observed at 65,250 cm^{-1} by ter Steege *et al.* [127]

In the present work, major vibrations observed in both acetone-h$_6$ and acetone-d$_6$ are ν_6' and ν_{16}' in the $3d_{yz}$ state. The $3d_{yz}$ + ν_2', ν_7', $\nu_8'$and ν_{11}' transitions observed in acetone-h$_6$ are not well resolved in acetone-d$_6$. In the $4d_{yz}$ state, ν_{19}' is observed in both species, while ν_8' is seen only in acetone-h$_6$ and ν_{22}' is seen only in acetone-d$_6$. The $3d_{x^2-y^2}$ transition is accompanied by an extensive progression in ν_8' in both species. Vibrations excited along with $4d_{x^2-y^2}$ include ν_1', ν_6', ν_8' in both species, while ν_{11}' appears only in acetone-h$_6$. For $5d_{x^2-y^2}$, only the ν_6' mode is observed in acetone-d$_6$ while there is no vibrational structure seen in acetone-h$_6$. In the $3d_{xy}$ state, ν_5', ν_8', ν_{11}' are seen in both isotopic species. Similarly in $4d_{xy}$, ν_1', ν_5', ν_6', ν_8' modes are again observed in both the species.

Table 4.15: Vibronic bands observed in the $3d_{xy}$ and $4d_{xy}$ Rydberg transitions

Assignment	**Present Study**		**Previous study for acetone-h$_6$ [123]**	
	Position			
	Acetone-h$_6$	**Acetone-d$_6$**	**Position**	**Assignment**
$3d_{xy}$	65,810#	65,832*	65,855	$3d_{xy}$
$3d_{xy}+\nu_8'$	66,114	66,097	--	--
$3d_{xy}+2\nu_8'$	66,471*	--	--	--
$3d_{xy}+\nu_{11}'$	66,724	66,483*	--	--
$3d_{xy}+3\nu_8'$	66,805*	--	--	--
$3d_{xy}+\nu_5'$	67,075*	66,756*	--	--
$3d_{xy}+5\nu_8'$	67,398*	--	--	--
$3d_{xy}+7\nu_8'$	68,040*	--	--	--
$4d_{xy}$	71,364*	71,374*	71,299	$4d_{xy}$
$4d_{xy}+\nu_8'$	71,682*	71,702*	--	--
$4d_{xy}+2\nu_8'$	72,004*	--	--	--
$4d_{xy}+\nu_6'$	72,388*	72,148*	--	--
$4d_{xy}+\nu_5'$	72,659 *	72,355*	--	--
--	--	--	74,364	†$5d_{xy}+\nu_{19}'$
$4d_{xy}+2\nu_6'$	73,434	72,941*	--	--
$4d_{xy}+\nu_1'$	74,461*	73,690*	--	--
$4d_{xy}+3\nu_5'$	--	74,221	--	--

All values are in cm^{-1}; *denotes blended lines; # observed at 65,910 cm^{-1} by ter Steege *et al.* [127];
†forbidden by vibronic selection rules

It may be noted that in case of acetone-h$_6$, the frequencies of the ν_8' and ν_{23}' modes are almost equal in the excited states, due to a considerable reduction in frequency of the ν_{23}' mode from 484 cm^{-1} in the ground state to ~330 cm^{-1} in excited states. Thus these modes cannot be distinguished from each other unless one of them is dipole forbidden for a particular transition. Moreover, since several fundamentals and combination bands have very similar frequencies, accidental degeneracies greatly complicate the assignments. Study of deuterated acetone helped in resolving several such discrepancies. Notwithstanding a few minor deviations all vibronic bands observed in acetone-h$_6$ are observed at the expected positions in acetone-d_6, thus confirming the assignments. The most striking feature of the acetone-h_6 assignments is that there are several bands which show structures displaced to the lower wavenumber side by approximately 78 cm^{-1} or 125 cm^{-1} which correspond to thermal population of torsional levels in the ground state. In acetone-d_6 these hot bands are not so prominent probably due to the lower frequencies (53 and 96 cm^{-1}) of these modes.

4.4 Summary

UV and VUV photoabsorption studies of acetone-h_6 and acetone-d_6 up to their first *IP* are carried out using SR. Detailed analysis of the observed vibronic features with particular emphasis on symmetry based selection rules and contribution from hot bands is presented. The comparative study of the electronic absorption spectrum of acetone-h_6 with acetone-d_6 serves to clarify some of the existing ambiguities and gives new insights into the excited state electronic structure. Some open issues like transitions with multiple assignments, unambiguous location of the ν_{00} origins in some of the Rydberg states and anomalous quantum defects observed in the nd_{xy} series are addressed in the current study. Quantum defect analysis and vibronic analysis of higher Rydberg series members of acetone-d_6 are reported for the first time.

The only valence transition observed lies in the UV region and corresponds to the n-π* ($^1A_2$) dipole forbidden transition which borrows intensity from the $n \rightarrow 3s$ ($^1B_2$) transition through vibronic coupling. The VUV absorption spectrum shows richly structured Rydberg series converging to the first *IP* at 9.708 eV. In the present work, assignments of *ns* and *np* Rydberg series are revised and a few new assignments are given for the *nd* Rydberg series. The quantum defect values of the *ns* and *np* series show fairly regular behavior, whereas in the *nd* states there is considerable variation. The anomalous quantum defect behavior observed along the nd_{xy} series in acetone-h_6 is also seen in acetone-d_6 although the variation in quantum defect values is smaller in the case of acetone-d_6.

Additionally, excitation of the non-totally symmetric modes (ν_{11}', ν_{16}' and ν_{19}') in acetone-d_6 leads to the conclusion that the *nd* series is indeed perturbed by a nearby state.

In all *ns* transitions, only totally symmetric vibrations are observed, accompanied by considerable hot band structure. In the *np* series, in addition to a few totally symmetric modes, the ν_{19}' mode appears along with several overtones. The frequency of the ν_{19}' mode in the $3p_y$ state of acetone-d_6 is proposed to be 340 ± 5 cm^{-1}. In the *nd* series, in contrast several non-totally symmetric modes are observed. In the present work, symmetry based selection rules are taken into account carefully while making assignments. Inclusion of hot band structure due to population of low lying torsional modes in the ground state is also resulted in clarification of some of the assignments. Transitions involving hot bands are not appeared very prominently in the room temperature absorption spectrum of acetone-d_6. Several vibronic assignments are confirmed and consolidated on the basis of the expected isotopic shifts in the vibrational modes of the two species and revised assignments are given for a number of transitions. Assignments are proposed for a few bands which are not assigned earlier.

Chapter-5

Rydberg and vibronic states of chloroform

5.1 Introduction

Chlorinated organic compounds are extensively used in industries and rank amongst the major environmental pollutants. VUV photoabsorption studies of chloromethanes are important for understanding atmospheric and interstellar chemical processes involving production of atomic chlorine and chlorine compounds. Chloroform ($CHCl_3$), which is emitted into the Earth's atmosphere from both natural and anthropogenic sources, is of special relevance to tropospheric chemistry, although its contribution to stratospheric ozone depletion is negligible due to its short lifetime [193]. Owing to the weak C–Cl bond, $CHCl_3$ is an ideal candidate for study of internal dissociation dynamics and its UV photolysis has been studied extensively in the laboratory from a fundamental point of view [193]. In contrast, VUV photoabsorption studies of chloroform are relatively sparse and few in number [24, 193-198], often being limited to 193 nm photolysis studies [193, 198].

The VUV absorption spectrum of $CHCl_3$ was first reported by Zobel and Duncan in 1955 [194]. Subsequently, its electronic absorption spectrum has been revisited a few times [24, 195, 196]. The intermediate splitting of the halogen lone pair ionization potential (*IP*) in alkyl polyhalides implies that Rydberg transitions above the first one or two bands are extensively overlapped, making assignments more difficult as compared to the alkyl monohalides. This was first pointed out by Robin [24] who discussed the overall features of the electronic absorption spectra of several chloromethanes and carried out qualitative assignments based on a comparative study. The first SR based VUV photoabsorption study of $CHCl_3$ was reported by Lee and Suto [196] in the wavelength region 105–220 nm (45,500–95,000 cm^{-1}). A few of the observed bands were classified into Rydberg series and vibronic assignments proposed for some of the transitions. However, the assignments made by them show several discrepancies. For instance, some of the intense vibronic features in the 72,500–76,500 cm^{-1} region are left unassigned whereas assignments have been proposed for relatively weak and unresolved features. Assignment of these bands as belonging to the $3e \rightarrow 4p$ transition also is doubtful as it implies a quantum defect of ~2.1 which is rather high for a chlorine p orbital. A mention also must be made here to the fluorescence studies carried out by Seccombe *et al.* [197]. They have mapped the dissociation channels of chloroform after VUV excitation in the region 8–12 eV by monitoring the dispersed fluorescence from the dissociation products, concluding that the fluorescence is mainly from neutral fragments produced by the dissociation of Rydberg states of the parent molecule. Thermochemical pathways and dissociation dynamics of neutral and ionized chloroform have also been studied by a variety of other techniques like threshold photoelectron photoion coincidence (TPEPICO) [199], imaging photoelectron photoion coincidence spectroscopy (IPEPICO) [200] and VUV negative photoion spectroscopy [201]. Other experimental studies of chloroform of relevance to its electronic absorption spectrum include studies of reaction mechanisms using femtosecond laser pulses [202] and electron impact studies of a few low lying excited states [203]. *IP*s for chloroform and several other halomethanes corresponding to excitation from the non bonding *p* orbitals of the halogen atoms have been reported by Dixon *et al.* [204]. On the theoretical front, although a few *ab initio* calculations have been reported for chloromethanes [205-207], most of the work is limited to ground state and ionization energy calculations and understanding of the electronically excited states in the VUV region is generally inadequate.

The present work is motivated by a need to build a better understanding of the high-lying excited states of chloroform particularly in the region 6.2–11.8 eV (50,000–95,240 cm^{-1}). VUV photoabsorption studies of $CHCl_3$ and $CDCl_3$ are performed using SR and a complete Rydberg series and vibronic analysis of the observed spectrum is carried out. The VUV photoabsorption spectrum of the deuterated compound $CDCl_3$ is reported for the first time and it serve to confirm and consolidate proposed vibronic assignments. Spectral analysis is aided by quantum chemical calculations.

5.2 Experimental

Experiments are performed in the energy region 6.2–11.8 eV (1050–2000 Å, 50,000–95,240 cm^{-1}) at a resolution of ~6 meV at 6 eV and ~10 meV at 10 eV using PPS beamline. Samples of $CHCl_3$ and $CDCl_3$ (M/s. MERCK) with stated purities > 99.5% are further purified by the freeze-pump-thaw technique and filled in the cell at the required pressure. Spectrum is recorded at various pressures in the range 10^{-4} to 1 mbar monitored with capacitance gauges.

5.3 Computational

$CHCl_3$ is a 26 valence electron system having C_{3v} geometry in the ground state. The ground state molecular orbital configuration is given by: [core] $(1a_1)^2(1e)^4(2a_1)^2(3a_1)^2(2e)^4(3e)^4(4e)^4(4a_1)^2$ $(1a_2)^2$: X^1A_1 where the numbering excludes the core electrons. The aim of the calculation is to generate the excited state energies for comparison with the experimentally observed photoabsorption spectra. The ground state geometry optimization and vibrational frequency calculations for $CHCl_3$ and $CDCl_3$ are performed under C_{3v} symmetry as well as C_s symmetry. The coordinate system used is such that the

C-H bond of $CHCl_3$ molecule is on the Z axis with the projection of one of the C–Cl bonds being along the Y axis. Electron correlation is included by use of hybrid exchange correlation functionals viz. PBE0 [35] and B3LYP [33, 34]. Ground state bond lengths, bond angles and normal mode frequencies are calculated using several basis sets including Pople's split valence basis set 6-31 G with d- type and f-type polarization functions [102, 208]. Since the excited state vibrational frequencies are not known exactly, ground state geometry optimization and frequency calculations are also carried out for the ionized species $CHCl_3^+$ and $CDCl_3^+$. Calculated values of ground state vibrational frequencies for neutral and ionized $CHCl_3$/$CDCl_3$ are shown in Table 5.1 and they are in good agreement with the experimental values wherever available [209]. It is also verified that all the predicted normal mode frequencies are real, thus ensuring the true minimum of the potential energy surface is obtained. Analysis of vibronic features observed in the electronic absorption spectra is greatly aided by computations of vibrational frequencies as discussed in section 5.4.2.

Table 5.1: Calculated frequencies (B3LYP/6-31 G (df)+) for neutral and ionized chloroform.

Normal Mode (symmetry)	**Neutral chloroform**		**Chloroform Ion**	
	$CHCl_3$	**$CDCl_3$**	**$CHCl_3^+$**	**$CDCl_3^+$**
ν_1: CH stretch (a_1)	3188(3034)	2348(2256)	3175	2340
ν_2: CCl_3 s-str (a_1)	665(680)	645(651)	653	647
ν_3: CCl_3 s-deform (a_1)	367(363)	364(367)	356	353
ν_4:CH bend (e)	1248(1220)	923(908)	1236	896
ν_5: CCl_3 d-str (e)	737(774)	715(737)	680	660
ν_6: CCl_3 d-deform (e)	261(261)	259(262)	148	148

Numbers in parenthesis are experimental values from Ref. [209], All entries are in cm^{-1}.

Excited state energies are calculated assuming the optimized ground state geometries using the TDDFT method. Computations of vertical excited states are performed using several correlation functionals like B3LYP and PBE0 with different basis sets *viz*. 6-31 G (d)+, 6-31 G (df)+, TZV (d)+, TZV (df)+. All these basis sets include heavy atom diffuse functions in order to obtain an accurate description of the Rydberg states. In this notation, df indicates that one set of d-type and one set of f-type heavy atom polarization functions are used. Since the region of interest is 6.2–11.8 eV, calculations are restricted to excited states lying below ~12 eV. When C_{3v} symmetry is imposed in the calculation, symmetry labels for some of the excited states are not correctly generated or show 'broken symmetry'. Since the outcome of the calculation is independent of the point group used, in order to obtain well defined symmetry species for all the excited states, calculations are also carried out under C_s symmetry. About 100 singlet excited states are predicted in the energy region up to 12 eV, however only a few of them are found to have appreciable oscillator strengths. MOs involved in the transitions are visualized by plotting the 3D electron densities using the visualization software MacMolPlt [100]. Theoretical results and their comparison with experimental observations are discussed in subsequent sections.

5.4 Results and discussions

The photoabsorption spectra of $CHCl_3$ and $CDCl_3$ in the region 50,000–95,000 cm^{-1} (~6.2–11.8 eV) are shown in Fig. 5.1. In the observed spectrum, except for the valence transition of $n \rightarrow \sigma^*$ at ~57,000 cm^{-1}, all transitions are of Rydberg type [24]. Most of the bands observed are quite diffuse or broad and a clear vibrational progression is seen only in the region 72,500–76,500 cm^{-1}. Analysis of observed spectra is divided in to two parts i) Rydberg series and ii) vibronic transitions.

5.4.1 Rydberg series

In the energy region 8.0–11.5 eV extensive Rydberg series converging to the first four *IP*s of $CHCl_3$ are observed (*c.f.* Fig. 5.1). Contour plots of the last few occupied orbitals and first few unoccupied orbitals of $CHCl_3$ using B3LYP/6-31 G (df)+ are shown in Figs. 5.2–5.4. HOMOs ($1a_2$, $4a_1$, $4e$, $3e$) are of non-bonding type and correspond to chlorine lone pair orbitals. The first few unoccupied orbitals, including the $5a_1$ LUMO, are antibonding in nature. Thus electronic excitations into the first few unoccupied orbitals are typically from non-bonding to antibonding orbitals, resulting in a series of Rydberg type transitions. The first four *IP*s of chloroform known from photoelectron spectroscopy studies [24, 204] are quite close in energy (11.48, 11.91, 12.01, 12.85 eV), all of them arising from removal of an electron from one of the chlorine lone pair non-bonding orbitals $1a_2$, $4a_1$, $4e$ and $3e$. Rydberg transitions converging to each of these four *IP*s are identified on the basis of quantum defect analysis using Eq. (1.1).

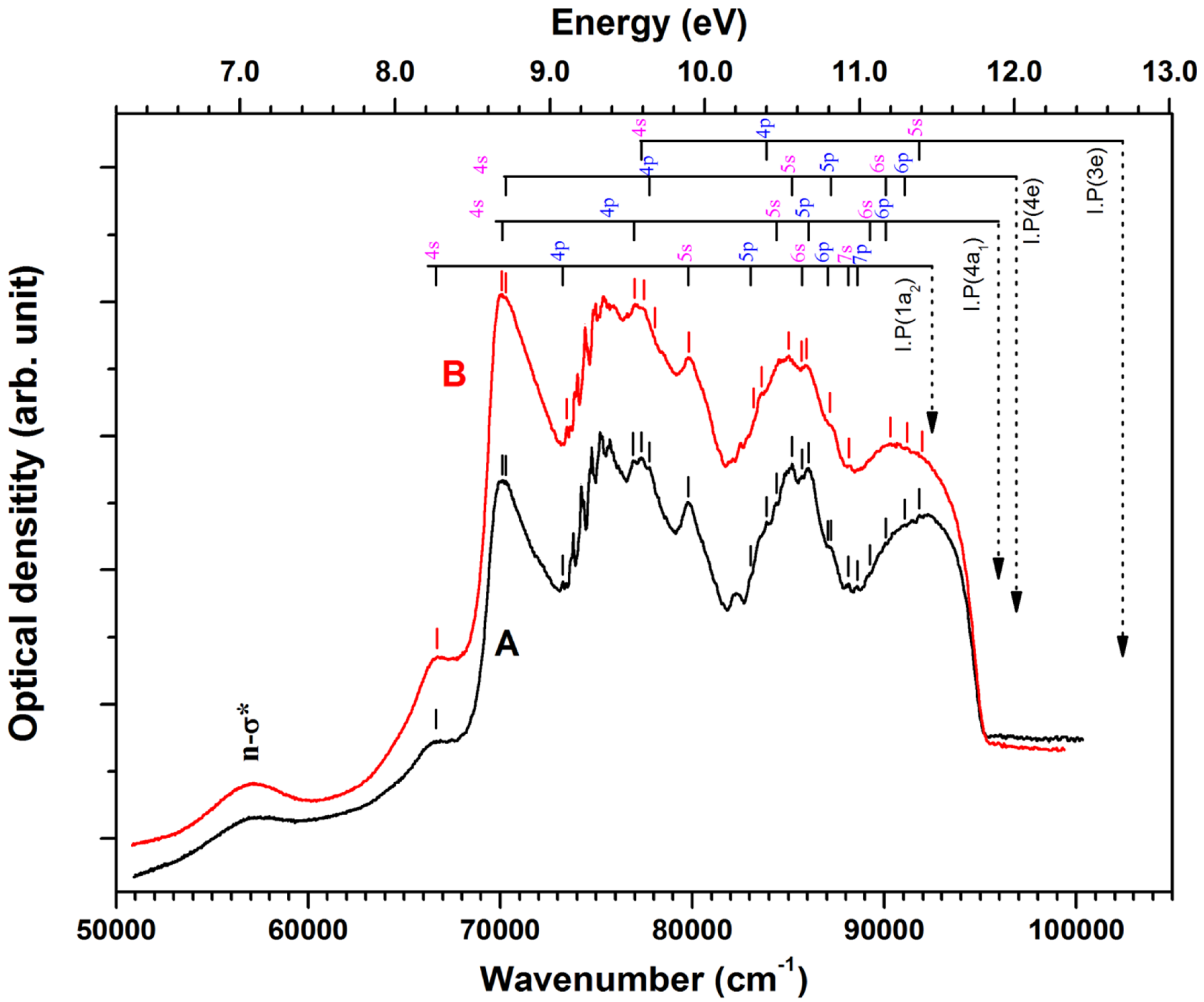

Figure 5.1: VUV photoabsorption spectra of A) $CHCl_3$ and B) $CDCl_3$ showing Rydberg Series converging to the four lowest *IP*s.

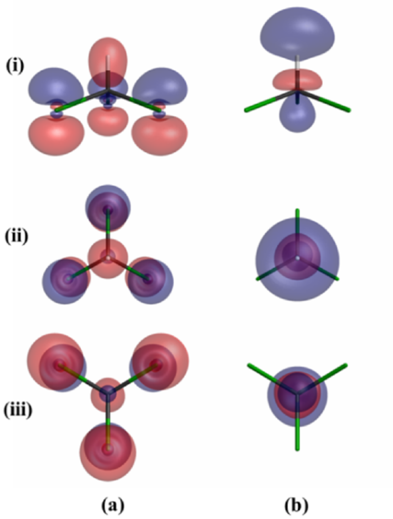

Figure 5.2: Contour maps of initial Cl lone pair $4a_1$ orbital (a) and final antibonding $6a_1$ orbital (b) viewed i) from Y–axis, ii) and iii) from +z and –z direction respectively.

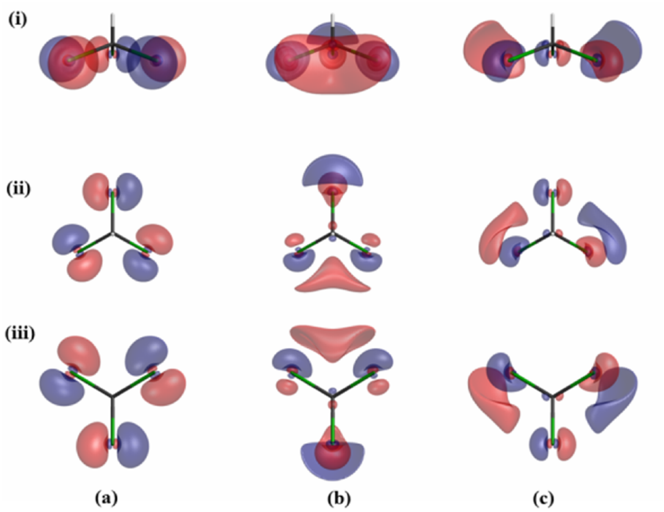

Figure 5.3: Contour maps of initial nonbonding orbital $1a_2$ (a) and final degenerate pair of antibonding $6e$ orbital (b and c) viewed i) from Y–axis, ii) and iii) from +z and –z direction respectively. Note in (c) small π-type bonding between C and one of the Cl atom

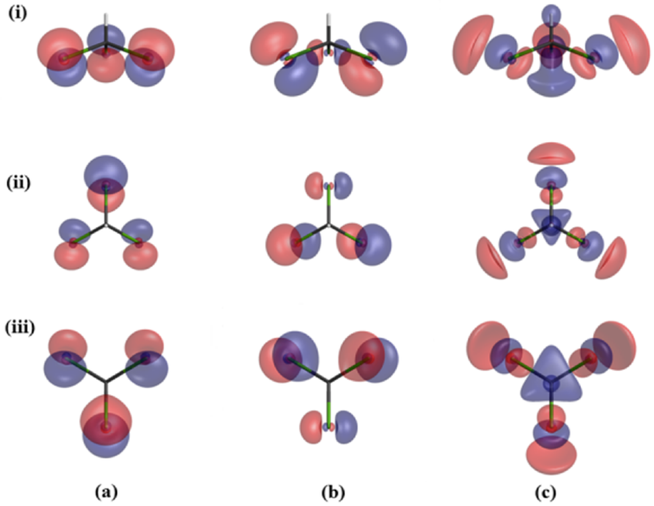

Figure 5.4: Contour maps of initial degenerate pair of $4e$ orbital (a and b) and final antibonding $8a_1$ orbital (c) viewed i) from Y–axis, ii) and iii) from +z and –z direction respectively.

Observed peak positions and quantum defects of $CHCl_3$ and $CDCl_3$ are listed in Table 5.2. The quantum defect values obtained are consistent with the atomic quantum defect values [210] for *s* and *p* orbitals of Cl. This indicates that the excitation is primarily from the chlorine lone pair non-bonding orbitals. Due to the closely spaced *IP*s, the higher members of the Rydberg series overlap with one another. Consequently only the first few members of each series are distinguished clearly. The maximum number of Rydberg transitions are identified for excitation from $1a_2$ (up to n=7), whereas in the case of 3*e*, only 4*s*, 5*s* and 4*p* Rydberg transitions are observed. Rydberg series for excitation from $4a_1$ and 4*e* are extended up to n=6.

Table 5.2: Rydberg transitions observed in the VUV absorption spectrum of Chloroform.

Assignment	**Peak Position**		**Quantum defect**	**Assignment**	**Peak Position**		**Quantum defect**
	(cm^{-1})	**(eV)**			**(cm^{-1})**	**(eV)**	
$1a_2\rightarrow 4s$	66,659	8.265	1.943	$1a_2\rightarrow 4p$	73,249	9.082	1.618
	66,706	8.270	1.941		73,455	9.107	1.605
$1a_2\rightarrow 5s$	79,783	9.892	2.073	$1a_2\rightarrow 5p$	83,049	10.297	1.609
	79,821	9.897	2.069		83,200	10.315	1.582
$1a_2\rightarrow 6s$	85,722	10.628	2.003	$1a_2\rightarrow 6p$	87,064	10.795	1.545
	85,688	10.624	2.013		87,173	10.808	1.500
$1a_2\rightarrow 7s$	88,142	10.928	2.034	$1a_2\rightarrow 7p$	88,598	10.985	1.758
	88,145	10.929	2.032		--	--	--
$4a_1\rightarrow 4s$	70,117	8.693	1.943	$4a_1\rightarrow 4p$	76,926	9.538	1.605
	70,070	8.688	1.945		76,984	9.545	1.602
$4a_1\rightarrow 5s$	84,388	10.463	1.934	$4a_1\rightarrow 5p$	86,047	10.668	1.690
	--	--	--		--	--	--
$4a_1\rightarrow 6s$	89,251	11.066	1.986	$4a_1\rightarrow 6p$	90,067	11.167	1.721
	--	--	--		90,305	11.196	1.634
$4e\rightarrow 4s$	70,280	8.714	1.968	$4e\rightarrow 4p$	77,766	9.642	1.603
	70,280	8.714	1.968		--	--	--
$4e\rightarrow 5s$	85,191	10.562	1.934	$4e\rightarrow 5p$	87,213	10.813	1.629
	85,014	10.540	1.957		87,173	10.808	1.635
$4e\rightarrow 6s$	90,067	11.167	1.983	$4e\rightarrow 6p$	91,059	11.290	1.653
	--	--	--		91,183	11.305	1.606
$3e\rightarrow 4s$	77,357	9.591	1.957	$3e\rightarrow 4p$	83,876	10.399	1.644
	77,476	9.606	1.952		83,600	10.365	1.660
$3e\rightarrow 5s$	91,831	11.386	1.952	--	--	--	--
	91,959	11.401	1.935		--	--	--

Upper and lower entries are observed peak positions of $CHCl_3$/$CDCl_3$

The difference in the zero point energy of the ground and excited state ν_{00} has an important contribution in assignment of the transitions and should be considered for a correct analysis. The predicted value of shift in ν_{00} between $CHCl_3$ and $CDCl_3$ is estimated using Eq. (1.2). The predicted value for isotope shift between $CHCl_3$ and $CDCl_3$ is found to be ~30 cm^{-1}. Note that the experimental values for ground state and ionic vibrational frequencies of $CDCl_3$ are not available in literature, hence calculated values (*cf.* Table 5.1) are considered for estimating the expected isotopic shift in ν_{00}. The observed spectra of $CHCl_3$ and $CDCl_3$ (*cf.* Fig. 5.1) show an isotope shift of up to ±300 cm^{-1} in the peak positions. The difference in observed and predicted values can be attributed to the fact that the actual vibrational frequencies differ from state to state. Here theoretically predicted ionic frequencies are considered for all upper states of $CHCl_3$ and $CDCl_3$ as well as for the ground state of $CDCl_3$, as the experimental values are not available. Moreover, higher order terms like anharmonicity are not included.

Extensive and clear vibrational structure is seen only in the 72,500–76,500 cm^{-1} region for both $CHCl_3$ and $CDCl_3$, assigned to $1a_2 \rightarrow 4p$ Rydberg state. It must be mentioned that the same vibrational structure had been assigned to the $3e \rightarrow 4p$ Rydberg transition (converging to the ^2E ion state of $CHCl_3^+$) by Lee and Suto [196]. However, considering more recent and accurate values of *IP*s [197], assignment of the bands at ~73,250 cm^{-1} to a 4*p* series converging to the 3*e* *IP* at 103,642 cm^{-1} result in a quantum defect of 2.1 which seems too high for a 4*p* orbital of chlorine. The present assignment of these bands to the $1a_2 \rightarrow 4p$ transition yields a quantum defect value of 1.6 which is consistent with that expected for chlorine 4*p* orbital. In higher energy regions, a few weaker vibrational features are observed. Although Lee and Suto [196] have assigned these weaker features to vibronic bands of 5*p*, 6*p* and 7*p*, in the present study it is not possible to distinguish this vibrational structure clearly. This could be due to limitations imposed by experimental resolution and severe overlap with the higher Rydberg series members. The absence of extensive vibrational structure in most of the electronic transitions is a clear indication that these absorption features are likely to be purely electronic in origin. It may also be concluded that there is no significant change in geometry of the molecule in most of the excited states. Moreover the high density of excited states implies that phenomena like predissociation and conical intersections between potential energy surfaces are likely to play a role. The broad and diffuse nature of the observed bands can also be attributed to the short lifetimes of the Rydberg states with respect to dissociation [197].

A comparison of the experimental and calculated excited state energies in the region below the first *IP* is given in Table 5.3. Of the four basis sets used, the 6-31 G sets are found to yield better results than the TZV basis sets. Further addition of an f-type polarization function 6-31 G (df)+ is found to give slightly better agreement with experimental values compared to 6-31 G (d)+. Hence vertical excitation energies, oscillator strengths and Λ values predicted by TDDFT using B3LYP/6-31 G (df)+ are tabulated in Table 5.3. The first few transitions corresponding to excitation from Cl nonbonding orbitals to the first three lowest unoccupied orbitals ($5a_1$ and $5e$) are assigned to valence transitions and are represented by the broad hump at ~7 eV in the experimental spectrum. The first Rydberg transition corresponds to excitation from the highest occupied orbital $1a_2$ to the $6a_1$ orbital. Most of the subsequent excitations are of Rydberg type except for the transitions predicted at 7.896 and 8.765 eV which are valence in nature. The high oscillator strength (0.17) of the transition at 8.765 eV is likely to contribute to the intensity of the experimentally observed broad peak at ~8.7 eV. In comparing the experimental and theoretical data for Rydberg series, a correspondence between the Rydberg series members originating from a given MO, i.e. $1a_2$, $4a_1$, $3e$ or $4e$ with the theoretically calculated energies for excitation from that particular MO is established. The nature of the final orbital is also taken into account.

Table 5.3: calculated (TDDFT/B3LYP/6-31 G (df)+) vertical excitation energies, oscillator strengths and coefficients of wavefunctions for dominant transitions and their comparison with experimentally observed transition energies for $CHCl_3$.

S. No.	**Transitions**			**Excitation Energies (eV)**	**Oscillator Strength**	**Λ**	**Observed (eV)**	**O-C (eV)**
	Initial	**Final**	**Coeff**					
1	H-2,3(4e)	L(5a_1)	±0.97	6.541	0.018	0.62	6.6-7.4[c]	--
2	H-4,5(3e)	L(5a_1)	-0.92	7.156	0.007	0.58		--
3	H(1a_2)	L+1,2(5e)	-0.91	7.385	0.005	0.52		--
4	H-1(4a_1)	L+1,2(5e)	±0.79	7.729	0.005	0.51		--
5	H-2,3(4e)	L+1,2(5e)	0.70	7.763	0.005	0.53		--
6	H(1a_2)	L+3(6a_1)	-0.99	7.880	0.000	0.29	8.265	0.39
7	H-1(4a_1)	L+1,2(5e)	0.53	7.896	0.044	0.54	~ 8.3[c]	--
	H-2,3(4e)	L+1,2(5e)	±0.56					--
8	H-1(4a_1)	L+3(6a_1)	-0.99	8.268	0.013	0.41	8.693	0.42
9	H-2,3(4e)	L+3(6a_1)	0.95	8.371	0.049	0.35	8.714	0.34
10	H-4,5(3e)	L+1,2(5e)	-0.62	8.765	0.170	0.51	~ 8.7[c]	--
11	H(1a_2)	L+4(7a_1)	0.99	8.983	0.000	0.27	9.892	0.91
12	H-4,5(3e)	L+3(6a_1)	±0.91	9.040	0.050	0.34	9.591	0.55
13	H(1a_2)	L+5,6(6e)	-0.90	9.252	0.005	0.35	9.082	-0.17
14	H-2,3(4e)	L+4(7a1)	±0.91	9.436	0.006	0.31	10.562	1.13
15	H-1(4a_1)	L+4(7a_1)	0.95	9.456	0.169	0.43	10.463	1.01
16	H-1(4a_1)	L+5,6(6e)	±0.93	9.598	0.001	0.34	9.538	-0.06
17	H-2,3(4e)	L+5,6(6e)	±0.66	9.696	0.012	0.40	9.642	-0.05
18	H-2,3(4e)	L+5,6(6e)	0.66	9.827	0.030	0.41	9.642	-0.18
19	H-4,5(3e)	L+4(7a_1)	0.63	10.089	0.012	0.29	11.386	1.30
	H(1a_2)	L+7,8(7e)	±0.74				10.297	0.21
20	H(1a_2)	L+9(8a_1)	-0.70	10.247	0.000	0.31	10.628	0.38
21	H-4,5(3e)	L+4(7a_1)	0.70	10.279	0.009	0.30	11.386	1.11
	H(1a_2)	L+7,8(7e)	±0.62				10.297	0.02
22	H-4,5(3e)	L+5,6(6e)	±0.58	10.347	0.089	0.36	10.399	0.05
23	H-4,5(3e)	L+5,6(6e)	±0.65	10.371	0.014	0.37	10.399	0.03
24	H(1a_2)	L+9(8a_1)	-0.69	10.445	0.000	0.31	10.628	0.18
25	H(1a_2)	L+10,11(8e)	-0.52	10.539	0.131	0.46	10.795	0.26
26	H-1(4a_1)	L+7,8(7e)	0.78	10.578	0.010	0.35	10.668	0.09
27	H-2,3(4e)	L+7,8(7e)	0.68	10.679	0.073	0.32	10.813	0.13
28	H-2,3(4e)	L+9(8a_1)	0.63	10.742	0.137	0.43	11.167	0.42
29	H-1(4a_1)	L+9(8a_1)	0.89	10.827	0.000	0.38	11.066	0.24
30	H-1(4a_1)	L+10,11(8e)	±0.71	10.908	0.005	0.36	11.167	0.26
31	H-1(4a_1)	L+10,11(8e)	-0.64	10.988	0.046	0.36	11.167	0.18
32	H-2,3(4e)	L+10,11(8e)	-0.66	11.038	0.003	0.35	11.290	0.25
33	H-2,3(4e)	L+10,11(8e)	±0.57	11.124	0.020	0.36	11.290	0.17
34	H(1a_2)	L+12(9a_1)	0.88	11.195	0.000	0.33	10.928	-0.27
35	H(1a_2)	L+13,14(9e)	±0.74	11.294	0.006	0.28	10.985	-0.31
36	H-4,5(3e)	L+7,8(7e)	0.57	11.394	0.006	0.32	--	--
37	H-4,5(3e)	L+9(8a_1)	0.88	11.545	0.002	0.32	--	--

[a]H = HOMO, L = LUMO; O–C=observed energy – calculated energy; [c]Valence transitions

It is to be noted that the *ns* orbitals are expected to have a_1 symmetry whereas *np* orbitals are expected to have a_1 or *e* symmetry under the C_{3v} point group. Thus transitions from $1a_2 \rightarrow$ *ns* are symmetry forbidden and expected to have zero oscillator strength. From the list of TDDFT predicted energies, the first such transition can be identified at 7.880 eV corresponding to the excitation from $1a_2 \rightarrow 4s(6a_1)$ and observed experimentally at 8.265 eV. Following this logic, the higher members of this Rydberg series are identified with excitations from $1a_2 \rightarrow 7a_1$, $8a_1$, $9a_1$ at 8.983, 10.247 (also 10.445) and 11.195 eV observed experimentally at 9.892, 10.628 and 10.928 eV respectively. Excitations from $4a_1$, 4*e* and 3*e* to *ns* type orbitals can be identified in a similar manner.

Next, looking for excitations from $1a_2$, $4a_1$, 4*e* and 3*e* to np orbitals and keeping in mind that the transition $a_1 \leftrightarrow a_2$ is forbidden under C_{3v} symmetry, 4*p*, 5*p*, 6*p*… *np* can be associated with the MOs 6*e*, 7*e*, 8*e* and so on. Following this approach, *ns* and *np* Rydberg series from Cl nonbonding orbitals observed in the present work could be assigned to theoretically predicted transitions (*cf.* Table 5.3). The difference between observed and calculated values is within 0.4 eV except for transition to the 5*s* state (1eV). In this context, it may be noted that the observed intensity for $1a_2 \rightarrow 5s$ transition (*cf.* Fig. 5.1) is much larger than expected for a symmetry forbidden transition. Such an effect could arise due to perturbation/coupling of the 5*s* state with other nearby states and needs to be investigated further. Note that in the present analysis, only those excitations are considered for which the TDDFT excitation amplitude is >0.5. It is observed that first few predicted excited states are dominated by excitation with high coefficient (>0.9) whereas as for higher energies, mixing of several excitations with lower coefficient (0.5–0.9) is seen. The experimentally observed state at 11.167 eV comprises of two Rydberg transitions $4e \rightarrow 6s$ and $4a_1 \rightarrow 6p$, which are not resolved in the current experiment. On the basis of MO approach described above, the $4e \rightarrow 6s$ transition can be associated with the predicted state at 10.742 eV. In the case of the $4a_1 \rightarrow 6p$ transition, the calculation predicts two energies which can be attributed to it, *viz*. 10.908 eV and 10.988 eV. Assignment of this transition to the state at 10.988 eV is more likely as its oscillator strength is much larger.

A stick spectrum generated from the B3LYP/6-31 G (df)+ calculations by plotting the excited state energies versus oscillator strength is shown in Fig. 5.5 along with the experimental spectrum for comparison. As can be seen from Table 5.3, the calculated and experimental energies are in overall good agreement for all the basis sets used. It may be noted that for the B3LYP functional used here, significant errors are to be expected for Λ< 0.3 [37]. In the present study, the calculated Λ values for all the excited states are found to be in the range 0.3 to 0.6 (*cf.* Table 5.3), thus confirming the suitability of the TDDFT method for these states. The relatively high Λ values for valence transitions (0.5–0.6) compared to Rydberg transitions (0.3–0.4) as seen in Table 5.3 confirm the valence and Rydberg nature of these transitions respectively. It is also observed that most of the predicted excited states of chloroform are predominantly Rydberg in character, consistent with assignment of all major observed transitions to Rydberg series members.

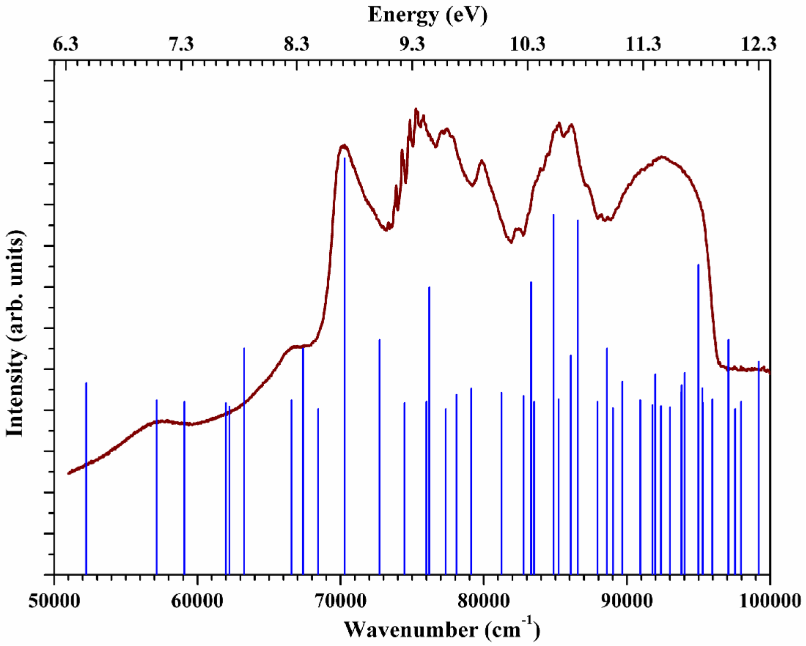

Figure 5.5: Comparison of experimental spectrum (solid line) with stick spectrum predicted theoretically with B3LYP/6-31 G (df)+

The nature of the excited states as valence or Rydberg can also be assessed by visualizing the shapes of the excited MOs (*cf.* Fig. 5.2–5.4). Consider the transition $4a_1$ (H-1)→ $6a_1$ (L+3) corresponding to the experimentally observed state at 8.693 eV. The initial orbital (*cf.* Fig. 5.2a) is Cl lone pair type, which shows a bonding character with respect to C–H. The final orbital is antibonding with respect to C–H whereas the non-bonding character of the 3*p* Cl orbitals is maintained. As can be seen from Fig. 5.2, the final orbital (*cf.* Fig. 5.2b) is also more diffuse in nature as is expected for a Rydberg state. The transition at 9.082 eV corresponds to excitation from $1a_2$ (H) → 6*e* (L+5, 6). The initial orbital is strictly non-bonding (*cf.* Fig. 5.3a), whereas the final orbitals are a degenerate pair of predominantly antibonding orbitals (*cf.* Figs. 5.3b and 5.3c). One of the degenerate pair (*cf.* Fig. 5.3c) has a small π type bonding contribution between the C atom and one of the Cl atoms. Both the excited orbitals are diffuse compared to the initial orbital. Fig. 5.4 shows the dominant excitations corresponding to the Rydberg transition at 11.167 eV. Here the excitation is from a degenerate pair of orbitals 4e (H-2, 3) → $8a_1$ (L+9). Again, the excitation is from non-bonding lone pair type orbitals to a highly diffuse antibonding orbital (*cf.* Fig. 5.4c). Similar observations can be made for other transitions assigned to Rydberg states.

5.4.2 Vibronic analysis of the $1a_2 \rightarrow 4p$ Rydberg Transition

The Rydberg transition $1a_2 \rightarrow 4p$ (72,500–76,500 cm^{-1}) is the only transition which shows a well formed vibrational structure (*cf.* Fig. 5.1), an observation which is corroborated by the isotopic shift of these bands in the spectrum of $CDCl_3$. In the earlier work by Lee and Suto [196], these vibrational bands were assigned to a ν_3' progression belonging to $3e \rightarrow 4p$ based on the available ground state vibrational frequencies of $CHCl_3$. These assignments however do not account for many of the observed features. For instance, the clear and intense features at ~73,746, 74,184, 74,738, 75,131, 75,245 and 75,643 cm^{-1} were left unassigned in their work. It may also be mentioned that Lee and

Suto [196] reported observation of double peaks with separation 120 cm^{-1} for each vibrational band but did not explicitly assign them. A re-examination of this band system with the help of *ab initio* calculations is resulted in a set of improved vibronic assignments and listed in Fig. 5.6 and Table 5.4.

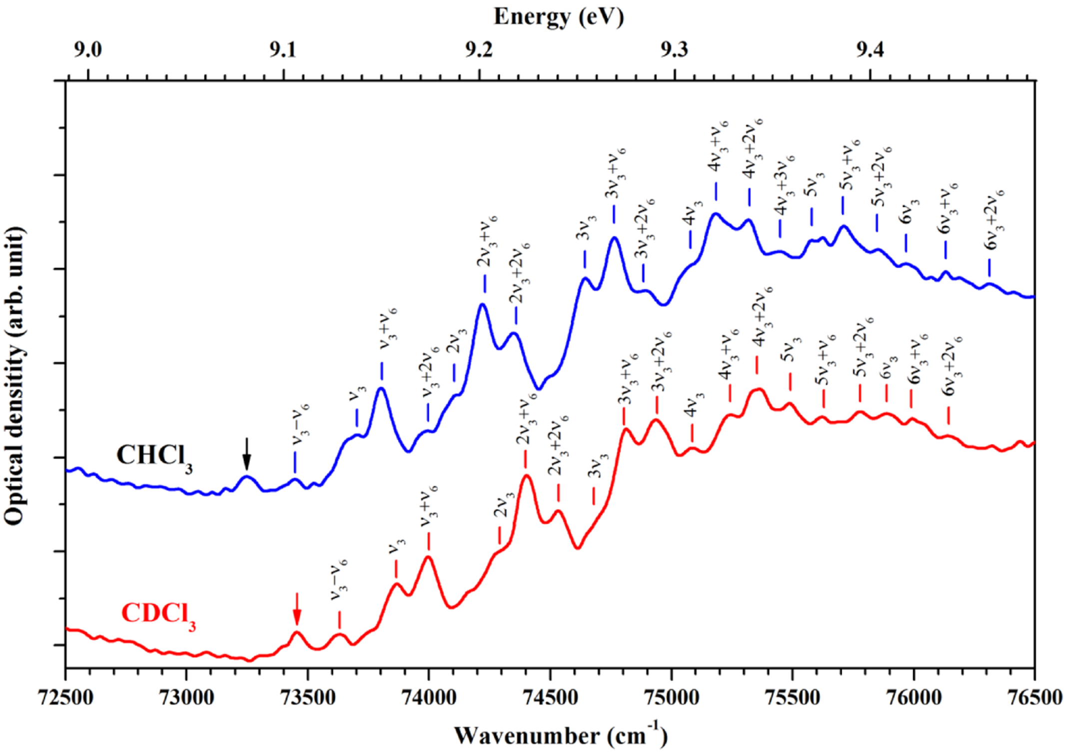

Figure 5.6: Vibronic Assignments in the 1a_2→4p system of CHCl$_3$ and CDCl$_3$. For clarity of presentation, plot of CHCl$_3$ is displaced vertically from CDCl$_3$.

Vibrational frequencies calculated using DFT/B3LYP for neutral and ionic CHCl$_3$ and CDCl$_3$ are given in Table 5.1 along with experimental values wherever available. The assumption that the vibrational frequencies in Rydberg states follow the ionic frequencies closely is a reasonable one as the structure of highly excited states would be closer to that of the ion rather than the neutral molecule. Note that experimental values for vibrational frequencies of CHCl$_3^+$ and CDCl$_3^+$ are not available in literature; hence the calculated values are used in the present analysis.

Table 5.4: Vibronic Assignments[a] in the $1a_2 \rightarrow 4p$ system

Assignment	**$CHCl_3$**		**$CDCl_3$**
	Present study	**Previous study [196]**	**Present study**
ν_{00}	73,249	73,201	73,455
$\nu_3' - \nu_6'$	73,444	--	73,629
ν_3'	73,704	73,605	73,865
$\nu_3' + \nu_6'$	73,811	--	73,998
$\nu_3' + 2\nu_6'$	73,995	--	--
$2\nu_3'$	74,104	74,041	74,291
$2\nu_3' + \nu_6'$	74,212	--	74,398
$2\nu_3' + 2\nu_6'$	74,345	--	74,534
$3\nu_3'$	74,643	74,582	74,680
$3\nu_3' + \nu_6'$	74,763	--	74,804
$3\nu_3' + 2\nu_6'$	74,884	--	74,940
$4\nu_3'$	75,075	74,985	75,085
$4\nu_3' + \nu_6'$	75,185	--	75,241
$4\nu_3' + 2\nu_6'$	75,322	--	75,351
$4\nu_3' + 3\nu_6'$	75,448	--	--
$5\nu_3'$	75,577	75,517	75,490
$5\nu_3' + \nu_6'$	75,709	--	75,628
$5\nu_3' + 2\nu_6$	75,849	--	75,777
$6\nu_3'$	75,962	75,924	75,887
$6\nu_3' + \nu_6'$	76,130	--	75,990
$6\nu_3' + 2\nu_6'$	76,312	--	76,143

[a] all peak positions are in (cm^{-1})

From Table 5.4 it can be seen that the observed spacing between successive vibronic bands cannot be accounted for by any one of the fundamental vibrational frequencies of ground and ionic states. However, properly accounting for the zero point energy of neutral and ionic ground states of both species (Eq. 1.24), and using the theoretically calculated neutral and ionic frequencies, the intense vibrational features may be fitted to progressions formed by combination bands of ν_3' and ν_6', corresponding to symmetrical and degenerate deformation modes. It may also be noted that the ν_3'

vibrational frequency remains almost the same in going from the ground state to the ionic state, whereas the frequency of the ν_6' mode is reduced from ~260 cm^{-1} to ~148 cm^{-1}(*cf.* Table 5.1). In this context it may mention that although the vibrational assignments given by Lee and Suto [196] for the weaker features are essentially correct, they were not able to assign the intense features due to non-consideration of combination bands. Moreover, they used only ground state frequencies in their analysis. In the present work, the calculated values of vibrational frequencies for the ionic states help in arriving at an accurate set of assignments. The double peak structures with separation 120 cm^{-1} mentioned by Lee and Suto [196] are also satisfactorily explained in terms of combination bands of ν_3' and ν_6' (*cf.* Fig. 5.6).

5.5 Summary

A comprehensive photoabsorption study of the Rydberg states of $CHCl_3$ in the VUV region (6–11.8 eV) is carried out using SR. The observed bands are classified into four Rydberg series converging to the first four *IP*s. Quantum defect analysis establishes that all excitations are from one of the non-bonding chlorine lone pair orbitals. TDDFT calculations of excited states are in good agreement with the experimentally observed energies. MO plots give additional insight into the nature of excited states. The only well defined vibrational progression observed in the 72,500–76,500 cm^{-1} region is assigned to the $1a_2 \rightarrow 4p$ Rydberg transition in contrast to the earlier assignment of this progression to the $3e \rightarrow 4p$. Vibronic analysis of this band is carried out with the help of *ab initio* calculations of ground state vibrational frequencies of both neutral and ionic species. Discrepancies in earlier work are clarified and revised assignments are proposed. Comparison with the vibronic spectrum of the deuterated isotopologue $CDCl_3$ serve a useful tool to verifying the assignments. The more intense vibrational features are found to be due to excitation of combination bands ν_3' and ν_6' modes, whereas the weaker features are assigned to excitation of the ν_3' mode. The frequencies of the ν_3' and ν_6' modes of $CHCl_3$ ($CDCl_3$) in the $1a_2 \rightarrow 4p$ state are estimated to be 454±13 (409±4) cm^{-1} and 130±21 (129±13) cm^{-1} respectively from the current set of assignments. This work presents a consolidated analysis of the VUV photoabsorption spectrum of $CHCl_3$ for the first time. These results could be useful inputs in future studies of photochemical processes involving chloroform.

Chapter-6

Matrix Isolation Spectroscopy of Acetone and Sulphur Dioxide

6.1 Introduction

The beginning of MIS was the experiments of Vegard [211] in the 1920s, wherein he observed luminescence resulting from electron bombardment on condensed nitrogen and rare gases. The term ‘matrix isolation’ was coined in 1954 independently by Pimentel *et al*. [64] and Norman and Porter [65], who used this technique for systematic studies of free radicals and transient species. A pictorial representation of molecules isolated in an inert gas matrix at cryogenic temperature is given in Fig.6.1. Highly reactive molecules or radicals with very short lifetimes are likely to have extended lifetimes in inert matrices and spectroscopic studies of such exotic species can be carried out conveniently using this technique. In addition, the effective transparency of rare-gas matrices, lack of appreciable diffusion, weak guest-host interactions and restricted rotational structure have contributed to the widespread use of the MIS technique [12, 19, 67]. Forbidden states, populated through non-radiative relaxation and which present a challenge in gas phase, can also be investigated spectroscopically using MIS techniques.

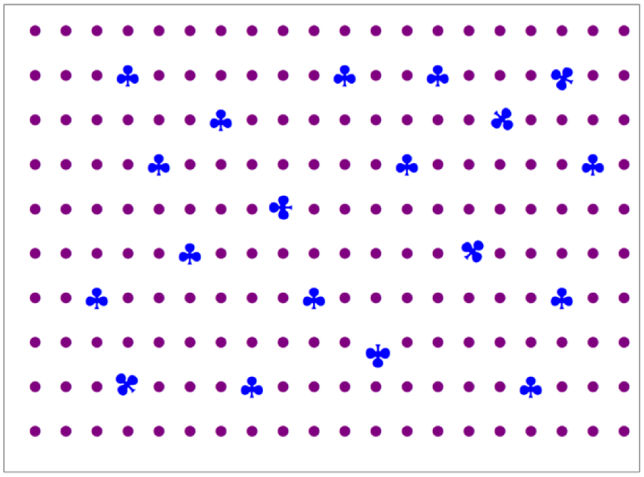

Figure 6.1: Pictorial representation of matrix isolation: the inert host (•) isolates the sample species (♣) from each other thereby preventing intra species interaction.

Today MIS is a well-established technique for a large range of applications including study of stable molecules [11], atmospheric chemistry [19], study of weak interactions (H-bonding, charge transfer and Van der Waals complexes) [13], transient species (radicals and ions generated by photolysis or discharge) [12], conformational studies in molecules [16], solute-solvent interactions, dynamics of molecular solvation [16] and reaction intermediates/mechanisms [17]. Photophysics and photochemistry of a variety of molecules have been very effectively studied using the MIS technique over the past few decades [9-12, 14-17, 19-21, 67].

The matrix can be prepared in two ways: by deposition of pre-mixed gaseous mixture or by co-deposition of the sample of interest to be studied along with the host gas. In both methods, gaseous flux is directed towards a cold window (4–50K) kept inside a cryostat under ultra high vacuum (10^{-7}-10^{-10} mbar). The ratio of sample to inert gas is kept such that the probability of two molecules/atoms occupying adjacent sites is negligible (*cf.* Fig. 6.1) for minimizing intra-species interaction. The trapped species can be studied with a variety of spectroscopic techniques such as FTIR, Raman, ESR, UV–visible or VUV absorption spectroscopy, fluorescence, etc. [19, 20, 67-69]. The exceptional versatility of the MIS technique and the availability of standard instrumentations for the detection of species place this method among fundamental methods of study in chemistry and chemical physics [9, 10, 12-17, 19-21, 66-69, 212]. SR is an ideal tool for carrying out UV/VUV photolysis and photoabsorption spectroscopy of the trapped species [12, 17]. For this purpose, an experimental setup for MIS is designed and developed at PPS beamline, as described in Chapter-2.

6.2 VUV Spectroscopy of Matrix Isolated Molecules: General

In the VUV region, MIS offers the possibility to study the changes in electronic and vibrational energies of the molecule in rare gas solids due to simplification of the spectrum by elimination of hot bands and freezing of the rotational structure [66]. In addition, the shifts in electronic transitions between gas phase and MI phase are important tools to identify the valence/Rydberg nature of the excited state. Rydberg orbitals have relatively large sizes and are more sensitive to perturbation from the matrix cage. Consequently Rydberg transitions show large shifts, typically few thousand cm^{-1} to the higher energy side in going from gas phase to MI phase [213]. Vibronic features of Rydberg transitions in gas phase are retained in rare gas matrices, but may be broadened appreciably. It has been discussed in earlier studies [24] that the width of the absorption peak is dependent on the electronic relaxation time pertaining to the electron mobility in the condensed phase and the electron excited to a free-molecule Rydberg orbital has considerable conduction band character. Generally in high electron mobility matrices like rare gases, where conduction electrons move as plane waves with weak-atom interaction, the relaxation time is expected to be long and the Rydberg transition as a consequence are not broadened significantly. In contrast, relaxation times are shorter in low electron mobility phases (like organic crystals) and Rydberg bands are broadened greatly, to the extent that they may not be observable. On the other hand, the valence shell excitations of the molecule are relatively unperturbed in going from gas phase to MI phase, irrespective of electron mobility of the host. These characteristic differences between Rydberg and valence excitations in gas phase and MI phase can be used to distinguish and confirm the nature of the electronic transitions.

This chapter reports VUV spectroscopy of SO_2, acetone-h_6 and acetone-d_6 in MI phase; the gas phase photoabsorption studies of these molecules are presented in Chapter-3 and -4. The work of this chapter, thus, provides a comparison of the photoabsortion spectra in the gas and MI phases, which is used to obtain a better understanding of the excited states of these molecules. To this end, a MI facility is developed at PPS beamline as discussed in Chapter-2.

6.3 Experimental details and results

6.3.1 VUV photoabsoprtion of SO_2

The MIS studies are carried out by isolating SO_2 in argon matrices at 10 K, in different ratios ranging from 0.2:1000 to 5:1000. VUV absorption spectra of SO_2 gas (room temperature) and ice (10K) are also recorded. To see the effect of annealing, SO_2 ice are annealed up to 80K and cooled back to 10K. Experiments are performed at different total depositions (2–50 mbar). The optimum deposition for VUV absorption studies is found to be 10 mbar.

The photoabsorption spectra of SO_2 recorded in the region 3.5–10 eV in MI and ice phases are shown in Fig. 6.2 and compared with the gas phase spectrum. MI phase spectra at different mixing ratios (SO_2: Ar) are shown in Fig. 6.3. The gas phase absorption spectrum comprises of several electronic band systems classically designated [50] as $\tilde{A}-\tilde{X}$, $\tilde{B}-\tilde{X}$, $\tilde{C}-\tilde{X}$, $\tilde{D}-\tilde{X}$, $\tilde{E}-\tilde{X}$, $\tilde{F}-\tilde{X}$ and $\tilde{G}-\tilde{X}$ as marked in Fig. 6.2. The $\tilde{A}+\tilde{B}$ system of SO_2 between 3.8–5.0 eV is the well known Clement's Band [25]. This band system is assigned to series involving excitation of ν_1' stretching and ν_2' bending modes in the gas phase [214].The absorption spectrum in this region of SO_2 in MI phase using krypton matrix was tentatively assigned to progression $A(\nu_1',\nu_2',0) \leftarrow X(0,0,0)$ in earlier studies [215]. The gas phase as well as the MI phase spectra of Fig.6.2 are in overall agreement with the earlier work.

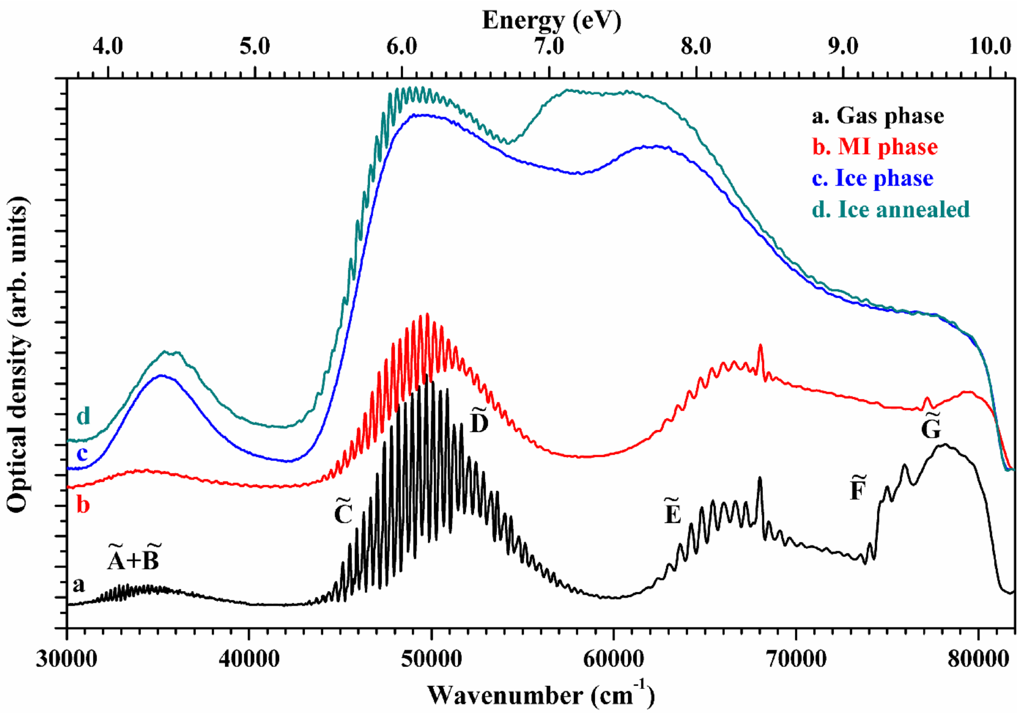

Figure 6.2: VUV absorption spectrum of SO_2 in gas phase (a), isolated in argon matrix (b) and ice phase before and after annealing (c & d) recorded using SR. Gas phase **s**pectrum is displaced vertically for clarity.

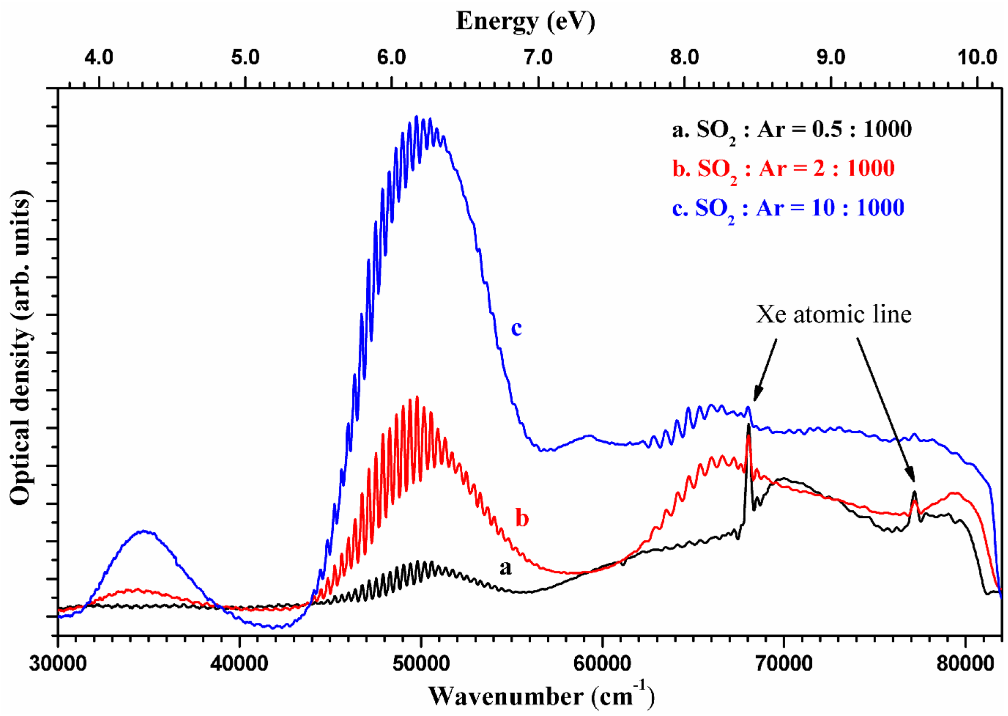

Figure 6.3: VUV absorption spectrum of matrix isolated SO_2 at different mixing ratios of SO_2 : Ar a) 0.5:1000 b) 2:1000 c) 10:1000.

In the MI phase at low concentration of SO_2, $\tilde{A} + \tilde{B}$ band is observed to be weak with weak and overriding vibrational structure. At higher concentrations and in the ice phase, this band appears as a broad hump. Holtom *et al.* [93] reported five bands in the spectrum of annealed SO_2 ice attributed to the ν_1' mode. In the present work, similar weak structures with a spacing of ~750–870 cm^{-1} are seen after annealing up to 80K. Peak positions of bands in this region for gas, MI and ice phase are shown in Table 6.1 along with those reported earlier. The step size used in the present work corresponds to an error of ±15 cm^{-1} in peak positions in this energy region. The bands in MI phase are red shifted compared to the gas phase spectrum. A few additional bands are observed in MI phase compared to earlier studies [93]. The observed band separations suggest excitations of ν_1' and ν_2' modes in the MI phase which are consistent with the gas phase results.

In the energy range ~ 5.2–7.2 eV, the $\tilde{C} + \tilde{D}$ system exhibits a rich band structure in the gas phase [50, 51]. Observed peak positions of vibrational bands of this system in gas, MI and ice phases are shown in Table 6.2. The vibrational bands are blue shifted by ~100–200 cm^{-1} from gas to MI phase but red shifted by ~300–600 cm^{-1} from MI to ice phase. In the gas phase spectrum, excitation of ν_2' bending mode is seen. Observed vibrational progressions show some irregularity and a few weak features which are attributed to Fermi interaction between ν_1' and $2\nu_2'$ modes and contribution from hot bands [50]. Going from gas phase to MI phase, this band retains its vibrational structure with a separation of ~380 cm^{-1} which may be tentatively assigned to the ν_2' mode. In the ice phase this band is devoid of vibrational structure, but upon annealing, structure appears with average spacing as in the MI phase. Weak features appearing in gas phase are not seen in the MI and ice phase. This may be attributed to the low temperatures, where hot bands are not expected to contribute. Since the molecule is trapped in a solid environment, excitation of the ν_1' stretching mode may be restricted leading to lifting of the degeneracy between ν_1' and $2\nu_2'$, thus suppressing the Fermi interaction observed in the gas phase. In the ice phase, SO_2 is expected to form an amorphous structure with random orientation and distribution of molecules due to background deposition. Such a disorder may be responsible for disappearance of vibrational structure. Annealing up to 80K allows the SO_2 molecules to re-order and settle to a more stable crystalline structure, in which a larger coupling between molecules may lead to an increase in the intensity of the vibration[73, 93].

Table 6.1: Vibronic bands observed in $\tilde{A}-\tilde{X}$ and $\tilde{B}-\tilde{X}$ systems of SO_2

	Gas phase			**MI Phase**		**Ice Phase (annealed)**	
S. no.	**Present work**	**Previous [216]**	**Previous [214]**	**Present work**	**Previous [215]**	**Present work**	**Previous [93]**
1	31,459	31,437	--	--	--	--	--
2	31,705	31,717	--	31,629	--	--	--
3	31,932	31,936	--	31,837	--	--	--
4	32,179	32,181	32,198	32,103	32,180	--	--
5	32,405	32,394	32,377	32,311	32,410	--	--
6	32,652	32,619	32,607	32,576	32,685	--	--
7	32,879	32,866	32,850	32,823	32,895	--	--
8	33,107	33,089	33,080	33,088	33,110	--	--
9	33,334	33,318	33,313	33,315	33,320	--	--
10	33,561	--	33,547	33,543	33,540	--	--
11	33,789	--	33,760	33,751	33,780	--	--
12	33,997	--	33,960	34,016	33,970	--	--
13	34,224	--	34,240	34,261	34,240	--	--
14	34,451	--	34,396	34,414	34,420	--	--
15	34,660	--	34,620	34,679	34,645	--	--
16	34,887	--	34,785	34,896	34,825	--	--
17	35,115	--	35,068	35,134	35,020	--	--
18	35,342	--	35,236	35,304	35,270	35,342	--
19	35,588	--	35,556	35,569	35,530	--	--
20	35,778	--	35,708	35,854	35,725	--	35,892
21	36,043	--	--	35,967	--	36,061	--
22	36,213	--	--	--	--	--	--
23	36,440	--	--	36,441	--	--	--
24	36,895	--	--	36,706	--	36,782	36,698
25	37,131	--	--	37,122	--	37,009	
26	--	--	--	37,369	--	--	37,505
27	--	--	--	37,786	--	37,843	--
28	--	--	--	38,144	--	--	--
29	--	--	--	38,373	--	--	38,392
30	--	--	--	38,885	--	38,846	--
31	--	--	--	--	--	39,482	39,279

All values are in cm^{-1}.

Table 6.2: Vibronic bands observed in $\tilde{C} - \tilde{X}$ and $\tilde{D} - \tilde{X}$ systems of SO_2

	Gas phase		MI Phase		Ice Phase	
S. no.	**Peak position**	**Successive difference**	**Peak position**	**Successive difference**	**Peak position**	**Successive difference**
1	43,298*					
2	43,653	355	43,753			
3	44,000	347	44,113	360	43,809	
4	44,378	378	44,492	379	44,227	418
5	44,757	379	44,871	379	44,587	360
6	45,136	379	45,250	379	44,928	341
7	45,533	397	45,647	397	45,231	303
8	45,913	380	46,007	360	45,590	359
9	46,291	378	46,386	379	45,951	361
10	46,670	379	46,746	360	46,310	359
11	47,030	360	47,125	379	46,670	360
12	47,409	379	47,523	398	47,011	341
13	47,807	398	47,902	379	47,371	360
14	48,186	379	48,281	379	47,731	360
15	48,565	379	48,660	379	48,110	379
16	48,944	379	49,019	359	48,451	341
17	49,322	378	49,398	379	48,811	360
18	49,701	379	49,777	379	49,152	341
19	50,080	379	50,155	378	49,531	379
20	50,478	398	50,554	399	49,910	379
21	50,876	398	50,933	379	50,289	379
22	51,255	379	51,330	397	50,649	360
23	51,652	397	51,709	379	51,008	359
24	52,050	398	52,107	398	51,400	392
25	52,448	398	52,486	379	51,747	347
26	52,846	398	52,903	417	52,107	360
27	53,282	436	53,263	360	52,467	360
28	53,604	322	53,660	397	52,826	359
29	54,039	435	54,039	379	53,225	399
30	54,361	322	54,418	379	53,604	379
31	54,797	436	54,816	398	54,001	397
32	55,138	341	55,213*	397	54,418*	417
33	55,536	398	55,612*	399	54,814*	396
34	55,933	397	55,972*	360		
35	56,332	399	56,369*	397		
36	56,699	367				
37	57,041	342				
38	57,487	446				
39	57,847*	360				
40	58,207*	360				
Average		382(28)		382(15)		367(24)

*features are weak and broad; all entries are in cm^{-1}. Entries in parenthesis are standard deviation.

In the energy region 7.4–9.0 eV (59,600–72600 cm^{-1}), the observed peaks in the MI phase are consistent with gas phase spectrum but are red shifted by ~10–100 cm^{-1} (*cf.* Table 6.3). In the ice phase, this band system appears as a broad structureless hump even after annealing, however, it resolves into two broad structures at ~7.2 eV (58,000 cm^{-1}), consistent with previous studies [93]. In the gas phase work (*cf.* Chapter-3), it is concluded that three valence states, i.e., $\tilde{X}\,^1A_1 \rightarrow 3\,^1A_1$, $2\,^1A_2, 2\,^1B_1$ along with excitation of the combination modes ($\nu_1' + \nu_2'$) and ($\nu_2' + \nu_3'$) are contributors to the $\tilde{E} - \tilde{X}$ system. The overall small shift of the band system in the MI phase confirms the predominant valence nature of the electronic states involved. Disappearance of the vibrational structure on condensation suggests quenching of the vibrational modes in the ice phase. The irregularities observed in the MI phase spectrum also indicate the presence of two or more electronic states in this region. PECs (*cf.* Fig. 3.7.) of the first few excited states show that this energy region is quite crowded. The possibility of a triplet state contributing to the additional broad peak at ~7.2 eV in the annealed ice spectrum cannot be ruled out, although a definite conclusion is difficult to draw.

Table 6.3: Vibronic bands observed in $\tilde{E} - \tilde{X}$ systems of SO_2

S. no.	Gas phase	MI phase	Shift (MI-gas)
1	61,844	61,787	-57
2	62,394	62,317	-77
3	63,018	62,924	-94
4	63,605	63,511	-94
5	64,231	64,136	-95
6	64,818	64,761	-57
7	65,424	65,387	-37
8	66,031	65,993	-38
9	66,656	66,618	-38
10	67,262	67,243	-19
11	67,660	67,622	-38
12	68,512	68,493	-19
13	--	68,891	--
14	69,118	69,110	-8
15	69,629	69,573	-56
16	70,293	70,263	-30

All entries are in cm^{-1}.

In Fig.6.2 the transitions above 9 eV (>72,500 cm^{-1}) appearing in the gas phase are completely disappeared in MI as well as in ice phase. These Rydberg states are either heavily blue shifted or completely obliterated from the spectrum.

6.3.2 VUV spectrum of acetone-h$_6$ and acetone-d$_6$ isolated in argon matrix

The electronic absorption spectrum of acetone lies largely in the VUV region. Rydberg series analysis and vibronic assignments of acetone-h$_6$ and acetone-d$_6$ in gas phase have been discussed in Chapter-4. In order to investigate behavior of *s*, *p* and *d*– Rydberg states in inert gas environment, the VUV photoabsorption spectra of acetone-h$_6$ and acetone-d$_6$ isolated in argon matrix are recorded in 5.5–10 eV region. Samples of acetone-h$_6$ and acetone-d$_6$ are purified by pump-freeze-thaw method and mixed with argon in different ratios from 0.2:1000–2:1000. Experiments are performed at different total depositions (2–50 mbar). VUV photoabsorption spectra of acetone-h$_6$ and acetone-d$_6$ in gas phase and MI phase at two different concentrations are shown in Figs. 6.4 and 6.5.

At higher concentrations, weaker features like the broad band at ~6.8 eV appear more clearly whereas the stronger features show saturation. A comparison of the MI phase VUV absorption spectra of acetone-h$_6$ and acetone-d$_6$ recorded at the same concentration (0.6:1000) is shown in Fig. 6.6. As seen from Figs. 6.4 and 6.5, The MI phase spectrum of acetone-h$_6$ (acetone-d$_6$) shows three prominent peaks at 7.259 (7.187), 7.398 (7.289) and 7.532 (7.398) eV. To higher energy side >8 eV, several relatively sharp peaks are seen. Additionally, at higher concentration ratio of acetone in argon, a broad hump is seen at ~6.2 eV. It has been noted by several workers [24, 217-220] that the lowest Rydberg excitation of a guest molecule in a rare gas matrix is blue shifted by ~2000–5000 cm^{-1} compared to free molecule spectrum with a typical width of ~200–500 cm^{-1}.

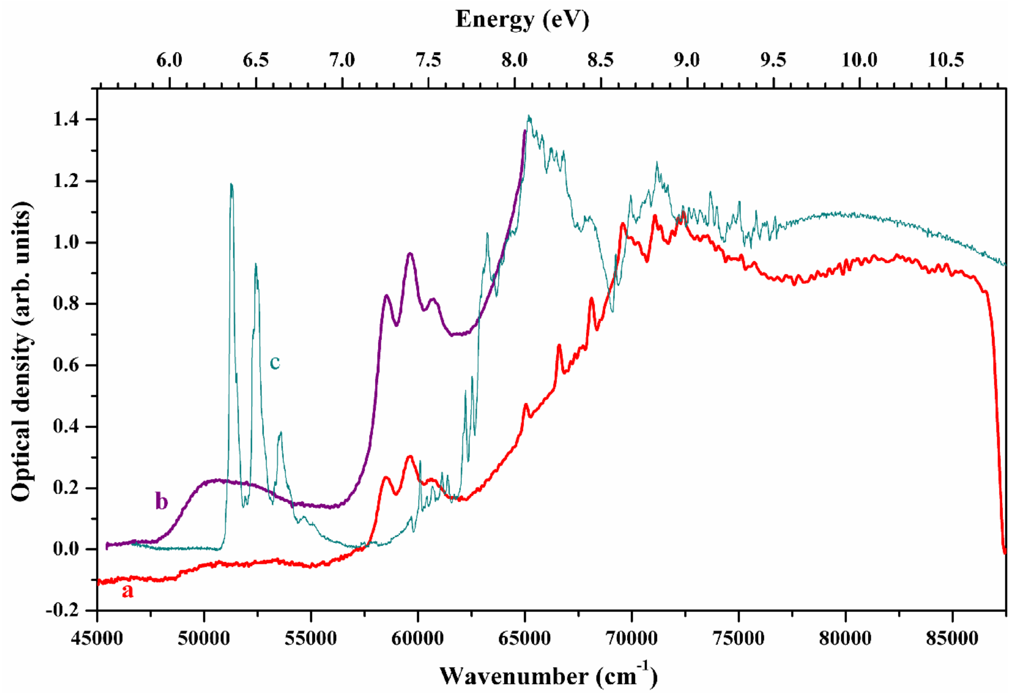

Figure 6.4: VUV absorption spectra of acetone-h_6 in argon matrices with acetone-h_6 : argon ratio a). 1:1000 b). 2.5:1000. Gas phase spectrum of acetone-h_6 (c) is also shown for reference. Spectra are displaced vertically for clarity.

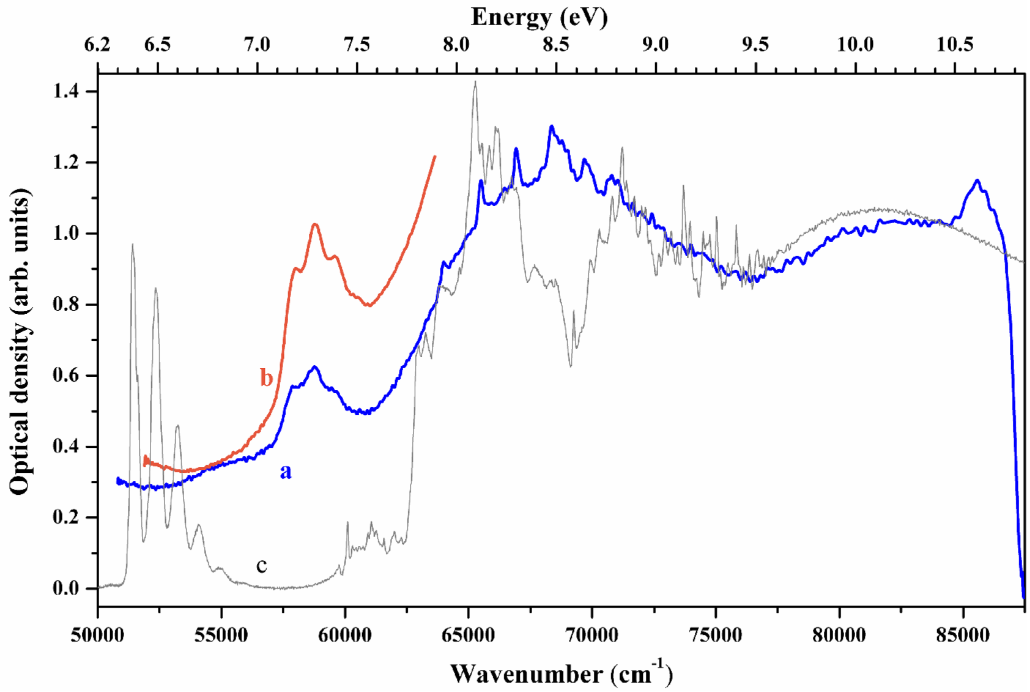

Figure 6.5: VUV absorption spectra of acetone-d_6 in argon gas matrices with acetone-d_6: argon ration a). 0.6:1000 b). 2.5:1000. Gas phase spectrum of acetone-h_6 (c) is also shown for reference. Spectra are displaced vertically for clarity.

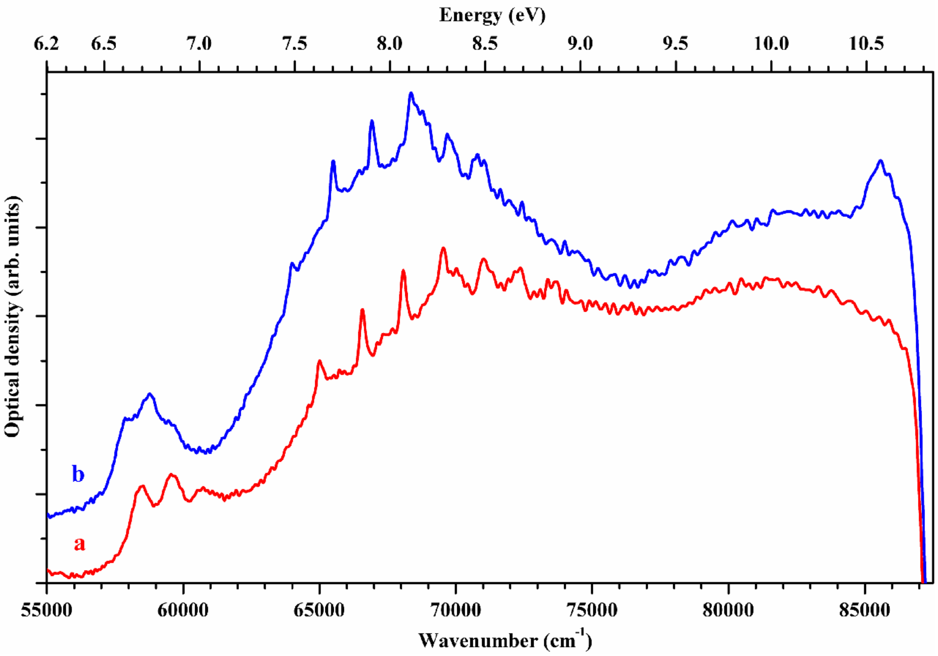

Figure 6.6: Absorption spectra of (a) acetone-h$_6$ and (b) acetone-d$_6$ in argon gas matrices with acetone : argon ratio 0.6:1000. Spectra are displaced vertically for clarity.

The structure of the three prominent peaks between 7–8 eV (56,000–64500 cm^{-1}) in MI phase look similar to the peaks corresponding to the 3s Rydberg transition and its accompanying vibronic structure in gas phase [221]. Here it should be mentioned that contribution from hot bands to the vibronic structure in gas phase (room temperature) is expected to be absent in the MI phase (10 K). If the energy shift from gas phase to MI phase and vibronic widths of these transitions in the MI phase are considered, the transition is blue shifted by ~7300 cm^{-1} in acetone-h$_6$ and ~ 6550 cm^{-1} in acetone-d$_6$, with vibronic widths of ~500 cm^{-1}. Thus three peaks at (58,548, 59,666, 60,753 cm^{-1}) in acetone-h$_6$ and (57,971, 58,789, 59,666 cm^{-1}) in acetone-d$_6$ can be assigned to the 3*s* transition and associated vibronic structure. The interval between successive peaks is ~1100 cm^{-1} in acetone-h$_6$ and ~860 cm^{-1} in acetone-d$_6$. From Table 4.1, it is seen the gas phase ground state and ionic frequencies of the totally symmetric ν_6' (CH$_3$ rock) mode for acetone-h$_6$ (acetone-d$_6$) are 1066 (887) cm^{-1} and 1045 (798) cm^{-1} respectively. The experimentally observed value of the ν_6' mode in the 3*s* state in gas phase is 1047 (1016) cm^{-1}. Alternatively, one may consider the b_2 symmetry ν_{22}' (CH_3 rock) mode whose frequencies in the ground state and ionic state for acetone-h$_6$ (acetone-d$_6$) are 1091 (960) cm^{-1} and 1032 (880) cm^{-1} respectively (cf. Table 4.1). However, since this vibronic transition is forbidden by symmetry selection rules, observed bands can be assigned to the ν_6' mode. Note that the isotopic shift of the first peak (acetone-d$_6$ compared to acetone-h$_6$) is red shifted by ~600 cm^{-1} in the MI spectrum. On the other hand, in the gas phase spectrum, isotopic shift in the origin of the 3*s* transition (ν_{00}) is blue shifted by by ~200 cm^{-1} (Table 4.3). On this basis it may be inferred that the ν_{00} band does not appear in the MI phase, and three observed peaks are due to higher members of the vibronic progression. This may be attributed to the Franck-Condon overlap between the ground and excited states, which is different in gas phase and MI phase due to differences in equilibrium geometry of electronic states in these phases.

To the higher energy side of the 3*s* peaks, five relatively sharp peaks are observed in the MI spectrum of acetone-h$_6$ (acetone-d$_6$) with fairly regular intervals of ~1500 (1420) cm^{-1}. The similarity of these vibrational intervals in acetone-h$_6$ and acetone-d$_6$ suggests that a vibrational mode that does not involve H (D) is excited. These transitions may be assigned to the a_1 symmetry ν_3' (CO stretch) mode whose calculated ionic frequency for acetone-h$_6$ (acetone-d$_6$) is 1570 (1534) cm^{-1}. It may be noted that although these vibrational intervals also match with the stretching frequency of the matrix isolated CO molecule [7, 72], the transitions observed in the present study are probably not due to absorption by CO produced by photodissociation of acetone as they appear at different energies in acetone-h$_6$ and acetone-d$_6$. Assignments of the observed transitions based on the present studies are summarized in Table 6.4. The electronic origin of the transitions between 8-9 eV could be either 3p$_y$ or 3p$_z$ correlating with the gas phase spectrum. However, it is difficult to conclusively assign the electronic state on the basis of current experimental data and available literature.

Therefore it is designated as X in the Table 6.4. A few weaker features are seen in this energy region which could be due to other vibrational modes or involving higher electronic states (valence/Rydberg) which are left unassigned in this work. A better understanding of the spectrum would require further experimental and theoretical investigations.

Table 6.4: Observed peak positions of acetone in MI phase

Acetone-h$_6$	**Acetone-d$_6$**	**Assignment**
58,548	57,971	--
59,666	58,789	--
60,753	59,666	--
65,062	64,020	X
66,616	65,531	$X + \nu_3$
68,120	66,934	$X + 2\nu_3$
69,559	68,353	$X + 3\nu_3$
71,073	69,686	$X + 4\nu_3$
72,359	70,822	--
73,475	--	--
74,074	--	--
75,930	--	--

All values are in cm^{-1}.

Interpretation of the broad hump (6.4 eV) appearing at higher concentration also needs some discussion. Energetically, the only transition that has the correct energy is the valence transition 1^3A_1 ($\pi \rightarrow \pi^*$). This is consistent with interpretation given by earlier workers in the study of condensed acetone [174]. It should be noted however that Lepage *et al*. [174] have studied acetone ice, whereas the current work is on acetone isolated in argon. As the concentration of acetone is increased the transitions which are normally forbidden in the isolated molecule may become allowed due to inter-molecular interactions. At this stage one can only make a tentative assignment which needs to be confirmed by further investigations.

6.4 Summary

The electronic absorption spectra of SO_2 and $(CH_3)_2CO/(CD_3)_2CO$ isolated in argon matrices at 10 K are investigated using SR. These studies have helped in further understanding the nature of electronic excitations in the UV-VUV regions and in assigning the vibrational modes in the excited electronic states.

In the case of SO_2, spectra of the ice phase at 10K are also recorded before and after annealing at 80 K. The observed band separations in the $\tilde{A} + \tilde{B}$ system (3.8–5.0 eV) suggest excitations of ν_1' and ν_2' modes in the MI phase which are consistent with the gas phase results. In the ice phase (annealed) the observed weak structures with a spacing of ~750–870 cm^{-1} are attributed to the ν_1' mode. In the $\tilde{C} + \tilde{D}$ system (5.2–7.2 eV), observed bands in MI phase and ice phase (annealed) are assigned to the ν_2' mode with almost constant separation of ~380 cm^{-1}. This is in contrast to the gas phase where the same system derives contribution from both ν_1' and ν_2', and is complicated by hot bands and Fermi resonances. In the $\tilde{E} - \tilde{X}$ system (7.4–9.0 eV), band separations observed in the MI phase suggest the presence of two or more electronic states consistent with the gas results. It may be noted that overall shifts in the transitions corresponding to $\tilde{A}$, $\tilde{B}$, $\tilde{C}$, $\tilde{D}$ and $\tilde{E}$ systems is very small as expected of valence transitions, whereas the higher excited states (>9 eV) are not observed in the present experiment in both MI and ice phase. This may be due to a very large blue shift as expected for Rydberg transitions, which effectively shifts the peaks beyond accessible region of present experiment (>11.8 eV).

In the case of acetone-h_6 and acetone-d_6, all VUV transitions are of Rydberg type and this is substantiated by the large blue shift of the 3*s* transition in going gas phase to MI phase. Isotopic shifts in the spectra of acetone-h_6 and acetone-d_6 has helped in assigning the associated vibronic structure appearing with the 3*s* transition as well as a higher Rydberg transition, whose origin could not be ascertained. Vibrational bands accompanying the 3*s* state are identified as ν_6' while the structure in the higher energy region is attributed to a progression in ν_3'. The possibility of the ν_3' progression arising from absorption by the CO molecule present as a residual impurity or produced by photodissociation of acetone is ruled out on the basis of the fact that the peak positions are same in acetone-h_6 and acetone-d_6.

Chapter-7

Conclusions and Future Direction

7.1 Conclusions

In this thesis, VUV spectroscopic studies of SO_2, $(CH_3)_2CO/(CD_3)_2CO$ and $CHCl_3/CDCl_3$ in the gas phase are carried out using SR. Also, the electronic absorption spectra of SO_2 and $(CH_3)_2CO/(CD_3)_2CO$ are investigated in the ice phase and MI phase using argon matrices. The experiments are carried out using two VUV beamlines *viz*. the HRVUV and PPS beamlines at the Indus-1 SR source at RRCAT, Indore. Spectral analysis is supported by quantum chemical calculations using the GAMESS (USA) suite of programs.

Development of the HRVUV beamline along with associated experimental station and development of a MIS setup at the PPS forms a major part of the experimental work reported in this thesis. The performance of the HRVUV beamline is evaluated by recording the VUV absorption spectra of Xe, O_2 and SO_2, demonstrating its utility for high resolution spectroscopy of atoms, molecules and clusters. In order to exploit the dual advantages of SR as a VUV source and the MIS technique, an experimental station for MIS is designed, developed and integrated with the Photophysics beamline. UV-visible spectra of O_2 ice are recorded to test the performance of the setup. MIS setup integrated with the PPS beamline is used to obtain VUV absorption spectra of pure argon and CO in argon matrix deposited at 10 K. Results are in very good agreement with literature thereby validating the performance of the MIS setup with SR. details of these development, optimization and testing are reported in Chapter-2.

Gas phase photoabsorption studies of the lesser understood $\tilde{E}-\tilde{X}$ system of SO_2 in the 1400– 1600 Å region are discussed in Chapter-3. All the observed series could be assigned to various vibronic transitions. Based on the quantum chemical calculations, it is concluded that at least three excited electronic states are involved in the $\tilde{E}-\tilde{X}$ system viz. $\tilde{X}\,^1A_1 \rightarrow 3\,^1A_1$, $\tilde{X}\,^1A_1 \rightarrow 2\,^1A_2$ and $\tilde{X}\,^1A_1 \rightarrow 2\,^1B_1$. Further, the observed vibrational features are mainly due to excitation of the combination modes ($\nu_1' + \nu_2'$) and ($\nu_2' + \nu_3'$) with some contributions from ν_1' and ν_3'. Here ν_1', ν_2' and ν_3' denote the frequencies of symmetric stretch, bending and asymmetric stretch modes respectively in the excited state. Potential energy curves corresponding to each of the normal modes of the SO_2 molecule have helped in gaining a qualitative understanding of the nature of the excited states in this region. The studies reported here are thus contribute to a better understanding of the excited state structure and dynamics of SO_2.

UV and VUV photoabsorption studies of acetone-h_6 and acetone-d_6 up to the first *IP* at 9.708 eV are carried out and issues like transitions with multiple assignments, unambiguous location of the ν_{00} origins in some of the Rydberg states and anomalous quantum defects observed in the nd_{xy} series are addressed. The valence transition in the UV region corresponds to the $n\rightarrow\pi^*$ ($^1A_2$) dipole forbidden transition which borrows intensity from the $n\rightarrow 3s$ ($^1B_2$) transition through vibronic coupling. In acetone-h_6, Rydberg series converging to the first *IP* are assigned to *ns*, *np* and *nd* type transitions and several discrepancies in earlier works are clarified. Quantum defect analysis and vibronic analysis of higher Rydberg series members of acetone-d_6 are reported for the first time. A major improvement compared to earlier work is that all symmetry based selection rules and hot band structure due to population of low lying torsional modes are taken into account carefully while making assignments. Several vibronic assignments are confirmed and consolidated on the basis of the expected isotopic shifts in the vibrational modes of the two species. This consolidated study of VUV spectroscopy of acetone-h_6 and acetone-d_6 is presented in Chapter-4.

A comprehensive photoabsorption study of the Rydberg states of $CHCl_3$ in the 6-11.5 eV region is reported in Chapter-5. The observed bands are classified into four Rydberg series converging to the first four *IP*s corresponding to electron excitation from non-bonding chlorine lone pair orbitals. TDDFT calculations of excited states are in good agreement with the experimentally observed energies. The only well defined vibrational progression observed in the 72,500–76,500 cm^{-1} region is assigned to the $1a_2 \rightarrow 4p$ Rydberg transition in contrast to the earlier assignment of this progression to the $3e \rightarrow 4p$. Discrepancies in earlier work are clarified and revised assignments are proposed. The vibronic spectrum of the $CDCl_3$, which is reported here for the first time, is found useful in verifying the assignments. A consolidated analysis of the VUV photoabsorption spectrum of $CHCl_3$ is given for the first time which may form useful inputs in future studies of photochemical processes involving $CHCl_3$.

In order to gain a better understanding of the nature of electronic excitations and assignments of vibrational modes in the excited electronic states, absorption spectra of SO_2 and $(CH_3)_2CO/(CD_3)_2CO$ isolated in argon matrices at 10 K are investigated using SR. In the case of SO_2, spectra of the ice phase at 10K are also recorded before and after annealing at 80 K. Overall energy shifts in the transitions between gas phase and MI phase corresponding to the $\tilde{A}$, $\tilde{B}$, $\tilde{C}$, $\tilde{D}$ and $\tilde{E}$ systems of SO_2 is very small as expected of valence transitions. On the other hand, higher excited states (>9 eV) which are Rydberg in nature are not observed, probably due to a very large blue shift which effectively displaces the peaks beyond the region accessible in the present experimental setup. Evidence for suppression of hot bands and Fermi resonances in the MI phase is observed in the $\tilde{C} + \tilde{D}$ system while in the $\tilde{E} - \tilde{X}$ system, band separations in the MI phase corroborate the gas phase results. In the case of acetone-h_6 and acetone-d_6, the large blue shift of the 3*s* transition and disappearance of the higher excited states in the MI phase suggest that all VUV transitions are of Rydberg type. Additionally, observed isotopic shifts between the spectra of acetone-h_6 and acetone-d_6 helped in assigning the associated vibronic structure appearing with the 3*s* transition (ν_6') as well as a higher Rydberg transition (ν_3'), whose origin could not be ascertained.

7.2 Future directions

This thesis provides a consolidated study of VUV spectroscopy of some select polyatomic molecules in the gas as well as matrix isolated phase. The total study has been accomplished through the development of HRVUV beamline, experimental workstations for gas phase absorption studies on HRVUV and PPS beamlines, matrix isolation set-up, and invoking quantum chemical calculations for analysis and interpretation of the observed spectra. For the chosen molecules, *viz*. sulfur dioxide, acetone (acetone-d_6) and chloroform (chloroform-d), a comprehensive study of the VUV spectroscopy in the energy range 6–11 eV is provided here. The work has resulted in clarifying several issues relating to the nature of the excited states, Rydberg and valence transitions, vibronic assignments etc. for the selected molecules. The methodologies developed here are general enough and they can be easily adopted for similar studies on other molecular systems.

The HRVUV beamline, developed during the course of the present work, has the potential to become a workhorse for high resolution work in VUV region. Note here that the new synchrotron sources all over the world are designed for higher electron energies and with critical wavelengths in the X-ray region. On this backdrop, the HRVUV beamline on Indus-1 synchrotron source provides a unique facility in the 6–25 eV region. The only drawback of the HRVUV beamline is the time taken for recording a spectrum; typically ~1 hr for 200 A at its full resolving power. This however can be improved dramatically by changing over from PMT scanning mechanism to the position sensitive detection system. This work has indeed been initiated on HRVUV and encouraging results have already been obtained. The matrix isolation set-up developed as a part of the work of this thesis holds high potential for studies in astrochemistry, thereby providing new avenues in cold and matrix isolated photochemistry.

The molecules studied in this thesis are of significant atmospheric interest. The gas phase VUV photoabsorption spectroscopy of these molecules therefore has close connection with the atmospheric chemistry involving these molecules. Some of these systems can well be studied using laser spectroscopic techniques such as REMPI to validate the assignments and the nature of the excited states proposed in the present work. While the current work focuses on the VUV spectra of gaseous samples at room temperature, there is a merit in conducting these studies in jet cooled molecular samples. For example, the VUV photoabsorption of acetone (deuterated acetone) in molecular jets is expected to simplify the spectral congestion by eliminating the contributions from higher vibrational levels including the hot band contributions.

Finally, the spectroscopy of highly excited states of molecules is inherently coupled to the processes such as dissociation, ionization and fragmentations. Combining the energetic of molecules with their VUV spectra is ultimately the way forward in molecular physics. This however calls for new spectroscopic techniques, viz. photoion-electron coincidence, mass analyzed threshold ionization, zero kinetic energy etc. Efforts are currently on to extend the present work in this direction.

References

[1] Connerade J, Baig M. *High resolution spectroscopy of atoms and molecules, including faraday rotation effects*, in Marr GV (ed.). *Handbook on synchrotron radiation*, Elsevier, Amsterdam (1987).

[2] Nenner I, Beswick J, Marr G. *Handbook on Synchrotron Radiation, Vol 2*, North-Holland, Amsterdam (1987).

[3] Dehmer JL, Dill D, Parr AC. *Photoionization Dynamics of Small Molecules*, in McGlynn SP, Findley GL, Huebner RH (eds.). *Photophysics and Photochemistry in the Vacuum Ultraviolet*, Springer, Netherlands (1985).

[4] Ashfold MNR. *Photodissociation Dynamics of Gas-Phase Small Molecules*, in McGlynn SP, Findley GL, Huebner RH (eds.). *Photophysics and Photochemistry in the Vacuum Ultraviolet*, Springer, Netherlands (1985).

[5] Hatano Y. *Spectroscopy and dynamics of molecular superexcited states. Aspects of primary processes of radiation chemistry*, Rad. Phys. Chem. **67**, 187 (2003).

[6] Limão-Vieira P, Duflot D, Giuliani A, Vasekova E, Lourenço JMC, Santos PM, et al. *Electronic State Spectroscopy of c-C_5F_8 Explored by Photoabsorption, Electron Impact, Photoelectron Spectroscopies and Ab Initio Calculations*, J. Phys. Chem. A. **112**, 2782 (2008).

[7] Mason NJ, Dawes A, Mukerji R, Drage EA, Vasekova E, Webb SM, et al. *Atmospheric chemistry with synchrotron radiation*, J. Phys. B, At. Mol. Opt. Phys. **38**, S893 (2005).

[8] da Silva FF, Almeida D, Martins G, Milosavljevic AR, Marinkovic BP, Hoffmann SV, et al. *The electronic states of pyrimidine studied by VUV photoabsorption and electron energy-loss spectroscopy*, Phys. Chem. Chem. Phys. **12**, 6717 (2010).

[9] Wu Y-J, Chen H-F, Camacho C, Witek HA, Hsu S-C, Lin M-Y, et al. *Formation and Identification of Interstellar Molecule Linear C_5H from Photolysis of Methane Dispersed in Solid Neon*, Astrophys. J. **701**, 8 (2009).

[10] Klaeboe P, Nielsen CJ. *Recent advances in infrared matrix isolation spectroscopy*, Analyst **117**, 335 (1992).

[11] Dunkin IR. *Matrix-Isolation Techniques A Practical Approach*, Oxford, New York (1998).

[12] Baskir EG, Misochko EY, Nefedov OM. *Spectroscopy and structure of free radicals stabilized in cryogenic matrices*, Rus. Chem. Rev. **78**, 683 (2009).

[13] Lu C, Song G, Lin J-M. *Reactive oxygen species and their chemiluminescence-detection methods*, Trends Anal. Chem. **25**, 985 (2006).

[14] Tasumi M, Nakata M. *Studies of rotational isomerism in low–temperature matrices*, J. Mol. Struct. **126**, 111 (1985).

[15] Barnes AJ. *Matrix isolation vibrational spectroscopy as a tool for studying conformational isomerism*, J. Mol. Struct. **113**, 161 (1984).

[16] Bondybey VE, Smith AM, Agreiter J. *New developments in matrix isolation spectroscopy*, Chem. Rev. **96**, 2113 (1996).

[17] Jacox ME. *The spectroscopy of molecular reaction intermediates trapped in the solid rare gases*. Chem. Soc. Rev. **31**, 108 (2002).

[18] Gerber R. Formation of novel rare-gas molecules in low-temperature matrices. Annu. Rev. Phys. Chem. **55**, 55 (2004).

[19] Viswanathan KS, Sankaran K, Sundararajan K. *Matrix Isolation Spectroscopy*, in *Atmospheric Chemistry. Encyclopedia of Analytical Chemistry*, Wiley (2006).

[20] Pfeilsticker K, Bösch H, Camy-Peyret C, Fitzenberger R, Harder H, Osterkamp H. *First*

atmospheric profile measurements of UV/visible O_4 absorption band intensities: Implications for the spectroscopy, and the formation enthalpy of the O_2-O_2 dimer, Geophys. Res. Lett. **28**, 4595 (2001).

[21] Perutz RN. *Photochemical reactions involving matrix-isolated atoms*, Chem. Rev. **85**, 77 (1985).

[22] Angal-Kalinin D, Banerji A, Hannurkar PR, Karmarkar MG, Kotaiah S, Mhaskar SP, et al. *Synchrotron radiation source Indus-1*, Curr. Sci. **82**, 283 (2002).

[23] Nandedkar RV. *Beamlines on Indian synchrotron radiation source Indus-1*, Curr. Sci. **82**, 291 (2002).

[24] Robin MB. *Higher Excited States of Polyatomic Molecules, Vol I*, Academic Press, New York (1974).

[25] Herzberg G. *Molecular spectra and molecular structure, Vol III*, van Nostrand Reinhold, New York (1966).

[26] Harris DC, Bertolucci MD. *Symmetry and Spectroscopy: An Introduction to Vibrational and Electronic Spectroscopy*, Courier Dover Publications (1978).

[27] Cotton FA. *Chemical applications of group theory*, John Wiley & Sons (2008).

[28] Hollas JM. *Modern spectroscopy*, John Wiley & Sons (2004).

[29] Atkins PW, Friedman RS. *Molecular quantum mechanics*, Oxford (2011).

[30] Hohenberg P, Kohn W. *Inhomogeneous electron gas*, Phys. Rev. **136**, B864 (1964).

[31] Kohn W, Sham LJ. *Self-consistent equations including exchange and correlation effects*, Phys. Rev. **140**, A1133 (1965).

[32] Jensen F. *Introduction to Computational Chemistry*, John Wiley & Sons (2007).

[33] Lee C, Yang W, Parr RG. *Development of the Colle-Salvetti correlation-energy formula into a functional of the electron density*, Phys. Rev. B **37**, 785 (1988).

[34] Becke AD. *Density-functional thermochemistry, Vol III. The role of exact exchange*, J. Chem. Phys. 98, 5648 (1993).

[35] Perdew JP, Burke K, Ernzerhof M. *Generalized Gradient Approximation Made Simple*, Phys. Rev. Lett. **77**, 3865 (1996).

[36] Hollas JM. High resolution spectroscopy, Wiley, New York (1998).

[37] Peach MJG, Benfield P, Helgaker T, Tozer DJ. *Excitation energies in density functional theory: An evaluation and a diagnostic test*, J. Chem. Phys. **128**, 044118 (2008).

[38] Schmidt MW, Baldridge KK, Boatz JA, Elbert ST, Gordon MS, Jensen JH, et al. *General atomic and molecular electronic structure system*, J. Comp. Chem. **14**, 1347 (1993).

[39] Baibich IM, Butler IS. *A brief introduction to molecular orbital theory of simple polyatomic molecules for undergraduate chemistry students*, Química Nova 35, 1474 (2012).

[40] Ito K, Maeda K, Morioka Y, Namioka T. *Performance of the 6VOPE high resolution VUV spectroscopic facility in the photoelectric detection mode*, Appl. Opt. **28**, 1813 (1989).

[41] Brown CM, Ginter ML. *Polarization enhancing optical system for a high-resolution vuv spectroscopic facility at a synchrotron light source*, Appl. Opt. **23**, 4034 (1984).

[42] Namioka T. *Theory of the Concave Grating. II. Application of the Theory to the Off-Plane Eagle Mounting in a Vacuum Spectrograph*, J. Opt. Soc. Am. **49**, 460 (1959).

[43] Ginter ML, Ginter DS, Brown CM. *High resolution VUV spectroscopic facility at the SURF II electron storage ring*, Appl. Opt. **27**, 4712 (1988).

[44] Das NC, Raja Sekhar BN, *Optical Design Procedure for the High Resolution VUV Beamline at Indus-1 Synchrotron Radiation Source*, Bhabha Atomic Research Centre (1996).

[45] Das NC, Shukla RP, Udupa DV, Sahoo NK, Bhattacharya D, Sunanda K, et al. *Development of a 6.65 m off-plane Eagle spectrometer for a high resolution vacuum ultraviolet beam-line at Indus-I synchrotron radiation source*, Curr. Sci. **87**, 1523 (2004).

[46] Samson JAR. *Techniques of Vacuum Ultraviolet Spectroscopy*, John Wiley and Sons, New York (1967).

[47] Matsui T, Cheung ASC, Leung KWS, Yoshino K, Parkinson WH, Thorne AP, et al. *High resolution absorption cross-section measurements of the Schumann-Runge bands of* O_2 *by VUV Fourier transform spectroscopy*, J. Mol. Spectrosc. **219**, 45 (2003).

[48] Hébert G, Innanen S, Nicholls R. *Identification Atlas of Molecular Spectra, no. 4. The* O_2 $B^3\Sigma_u^{-}X\Sigma_g^{-}$ *Schumann–Rungé System*. (1967).

[49] Hébert GR, Innanen SH, Nicholls RW. *Identification Atlas of Molecular Spectra*, 1-29 (1967).

[50] Palmer MH, Shaw DA, Guest MF. *The electronically excited and ionic states of sulphur dioxide: An ab initio molecular orbital CI study and comparison with spectral data*, Mol. Phys. **103**, 1183 (2005).

[51] Golomb D, Watanabe K, Marmo FF. *Absorption Coefficients of Sulfur Dioxide in the Vacuum Ultraviolet*, J. Chem. Phys. **36**, 958 (1962).

[52] Yamanouchi K, Okunishi M, Endo Y, Tsuchiya S. *Laser induced fluorescence spectroscopy of the* $\tilde{C}^1B_2$–$\tilde{X}^1A_1$ *band of jet-cooled SO2: rotational and vibrational analyses in the 235-210 nm region*. J. Mol. Struct. **352-353**, 541 (1995).

[53] Robert Wu CY, Yang BW, Chen FZ, Judge DL, Caldwell J, Trafton LM. *Measurements of High-, Room-, and Low-Temperature Photoabsorption Cross Sections of* SO_2 *in the 2080- to 2950-Å Region, with Application to Io*, Icarus, 145, 289 (2000).

[54] Giuliani A, Jamme F, Rouam V, Wien F, Giorgetta J-L, Lagarde B, et al. *DISCO: A low-energy multipurpose beamline at synchrotron SOLEIL*, J. Synchrotron Rad. **16**, 835 (2009).

[55] Song YF, Ma CI, Hsieh TF, Huang LR, Chung SC, Cheng NF, et al. *Performance of a novel VUV bending magnet beamline*, Nucl. Instr. Meth. Phys. Res. A **467-468**, 569 (2001).

[56] Rah SY, Kang TH, Chung Y, Kim B, Lee KB. *Bending magnet VUV beamline 2B at the Pohang Light Source.* Rev. Sci. Instr. **66**, 1751 (1995).

[57] Nahon L, Polack F, Lagarde B, Thissen R, Alcaraz C, Dutuit O, et al. *Complete characterization of SU5:: a VUV high resolution beamline with variable polarizations*, Nucl. Instr. Meth. Phys. Res. A **467-468**, 453 (2001).

[58] Nahon L, Oliveira Nd, Garcia GA, Gil JF, Joyeux D, Lagarde B, et al. *DESIRS : A state-of-the-art VUV beamline featuring high resolution and variable polarization for spectroscopy and dichroism at SOLEIL*, J. Phys., Conf. Ser. **425**, 122004 (2013).

[59] Koike M, Heimann PA, Kung AH, Namioka T, DiGennaro R, Gee B, et al. *VUV high resolution and high flux beamline for chemical dynamics studies at the advanced light source*. Nucl. Instr. Meth. Phys. Res. A **347**, 282 (1994).

[60] Kimura S-I, Ito T, Sakai M, Nakamura E, Kondo N, Horigome T, et al. *SAMRAI: A novel variably polarized angle-resolved photoemission beamline in the VUV region at UVSOR-II*, Rev. Sci. Instr. **81**, 053104 (2010).

[61] Matsui T, Sato H, Shimada K, Arita M, Senba S, Yoshida H, et al. *3 m off-plane Eagle monochromator at the helical undulator beamline of HiSOR*, Nucl. Instr. Meth. Phys. Res. A **467-468**, 537 (2001).

[62] Song YF, Yuh J-Y, Lee Y-Y, Chung SC, Huang LR, Tsuei K-D, et al. *Performance of an ultrahigh resolution cylindrical grating monochromator undulator beamline*, Rev. Sci. Instr. **77**, … (2006).

[63] Das NC, Raja Sekhar BN, Saraswathy P, Shastri A, Bhattacharya SS, Bhatt S, et al. *Development of Photophysics Beamline at Indus-1 Synchrotron Radiation Source*, J. Opt. (India) **32**, 169 (2003).

[64] Whittle E, Dows DA, Pimentel GC. *Matrix Isolation Method for the Experimental Study of Unstable Species*, J. Chem. Phys. 22, 1943 (1954).

[65] Norman I, Porter G. *Trapped Atoms and Radicals in a Glass 'Cage'*, Nature **174**, 508 (1954).

[66] Hoboken, NJ. *Reactive Intermediate Chemistry*, Wiley (2004).

[67] Gerber RB. Formation of novel rare-gas molecules in low-temperature matrices, Annual Rev. Phys. Chem. **55**, 55 (2004).

[68] Tiedje HF, DeMille S, MacArthur L, Brooks RL. *Cavity ring-down spectroscopy of transient O_2-O_2 dimers*, Can. J. Phys. **79**, 773 (2001).

[69] Sneep M, Ityaksov D, Aben I, Linnartz H, Ubachs W. *Temperature-dependent cross sections of – collision-induced absorption resonances at 477 and 577 nm*, J. Quant. Spectrosc. Radiative Trans. **98**, 405 (2006).

[70] Landau A, Allin EJ, Welsh HL. *The absorption spectrum of solid oxygen in the wavelength region from 12,000 Å to 3300 Å*. Spectrochimica Acta **18**, 1 (1962).

[71] Sneep M, Ityaksov D, Aben I, Linnartz H, Ubachs W. *Temperature-dependent cross sections of O2–O2 collision-induced absorption resonances at 477 and 577 nm*, J. Quant. Spectrosc. Radiative Trans. **98**, 405 (2006).

[72] Lu H-C, Chen H-K, Cheng B-M, Kuo Y-P, Ogilvie JF. *Spectra in the vacuum ultraviolet region of CO in gaseous and solid phases and dispersed in solid argon at 10 K*, J. Phys. B, At. Mol. Opt. Phys. **38**, 3693 (2005).

[73] Mason NJ, Dawes A, Holtom PD, Mukerji RJ, Davis MP, Sivaraman B, et al. *VUV spectroscopy and photo-processing of astrochemical ices: an experimental study*, Faraday Disc. **133**, 311 (2006).

[74] Belyaev D, Korablev O, Fedorova A, Bertaux J-L, Vandaele A-C, al. *First observations of SO_2 above Venus' clouds by means of solar occultation in the infrared*, J. Geophys. Res. **113**, 1 (2008).

[75] Jessup KL, Spencer JR, Yelle R. *Sulphur volcanism on Io*, Icarus **192**, 24 (2007).

[76] Manatt SL, Lane AL. *A compilation of the absorption cross-sections of SO_2 from 106 to 403 nm*, J. Quant. Spectrosc. Radiative Trans. **50**, 267 (1993).

[77] Loyola D, van Geffen J, Valks P, Erbertseder T, Van Roozendael M, Thomas W, et al. *Satellite-based detection of volcanic sulphur dioxide from recent eruptions in Central and South America*, Adv. Geosci. **14**, 35 (2008).

[78] Knappenberger JKL, Castleman JAW. *The infuence of cluster formation on the photodissociation of sulphur dioxide*, J. Chem. Phys. 121, 3540 (2004).

[79] Knappenberger JKL, Castleman JAW. *Photodissociation of Sulfur Dioxide: The Ẽ State Revisited*, J. Phys. Chem. A **108**, 9 (2003).

[80] Blackie D, Blackwell-Whitehead RJ, Stark G, Pickering JC, Smith PL, Rufus J. *High resolution photoabsorption measurements of SO_2 at 198K from 213-325 nm*, J. Geophys. Res. **116**, E03006 (2011).

[81] Rufus J, Stark G, Thorne AP, Pickering JC, Blackwell-Whitehead RJ, Blackie D, et al. *High-resolution photoabsorption cross-section measurements of SO2 at 160 K between 199 and 220 nm*. J. Geophys. Res., Planets **114**, E06003 (2009).

[82] Rufus J, Stark G, Smith PL, Pickering JC, Thorne AP. *High-resolution photoabsorption cross section measurements of SO_2, 2: 220 to 325 nm at 295 K*, J. Geophys. Res., Planets **108**, 5011 (2003).

[83] Hermans C, Vandaele AC, Fally S. *Fourier transform measurements of SO_2 absorption cross sections: I. Temperature dependence in the 24000–29000 cm^{-1} (345–420 nm) region*, J. Quant.

Spectrosc. Radiative Trans. **110**, 756 (2009).

[84] Ahmed SM, Kumar V. *Quantitative photoabsorption and flourescence spectroscopy of SO_2 at 188–231 and 278.7–320 nm*, J. Quant. Spectrosc. Radiative Transfer **47**, 359 (1992).

[85] Hamdy H, He ZX, Samson JAR. *Precision photoabsorption cross section measurements of SO 2 from 147 to 1017 Å*, J. Phys. B, At. Mol. Opt. Phys. 24, 4803 (1991).

[86] Freeman DE, Yoshino K, Esmond JR, Parkinson WH. *High resolution absorption cross section measurements of SO_2 at 213 K in the wavelength region 172–240 nm*. Planetary Space Sci. **32**, 1125 (1984).

[87] Danielache SO, Eskebjerg C, Johnson MS, Ueno Y, Yoshida N. *High-precision spectroscopy of ^{32}S, ^{33}S, and ^{34}S sulfur dioxide: Ultraviolet absorption cross sections and isotope effects*, J. Geophys. Res., Atmospheres **113**, D17314 (2008).

[88] Herzberg G. *Molecular Spectra and Molecular* Structure III, van Nostrand, New York (1966).

[89] Dixit AA, Lei Y, Lee KW, Quiñones E, Houston PL. *Dissociation of Sulfur Dioxide by Ultraviolet Multiphoton Absorption between 224 and 232 nm*, J. Phys. Chem. A **109**, 1770 (2005).

[90] Brand JCD, Chiu PH, Hoy AR, Bist HD. *Sulfur dioxide: Rotational constants and asymmetric structure of the $\tilde{C}^1B_2$ state*, J. Mol. Spectrosc. **60**, 43 (1976).

[91] Innes KK. *SO_2: Origins of unequal bond lengths in the $\tilde{C}^1B_2$ electronic state*, J. Mol. Spectrosc. **120**, 1 (1986).

[92] Suto M, Day RL, Lee LC. *Fluorescence yields from photodissociation of SO_2 at 1060-1330 Å*, J. Phys. B, At. Mol. Phys. **15**, 4165 (1982).

[93] Holtom PD, Dawes A, Mukerji RJ, Davis MP, Webb SM, Hoffman SV, et al. *VUV photoabsorption spectroscopy of sulfur dioxide ice*, Phys. Chem. Chem. Phys. **8**, 714 (2006).

[94] Vuskovic L, Trajmar S. *Electron impact spectra of SO_2: Differential integration and momentum transfer cross sections*, J. Chem. Phys. **77**, 5436 (1982).

[95] Vušković L, Trajmar S. *The electron impact spectra of SO_2*, J. Raman Spectrosc. **10**, 136 (1981).

[96] Avouris P, Demuth JE, Schmeisser D, Colson SD. *An electron energy loss study of the triplet states of SO_2*, J. Chem. Phys. **77**, 1062 (1982).

[97] Abulain BT. *Near-threshold electron-impact excitation of sulphur dioxide*, J. Chem. Soc. Faraday Trans. 2 **81**, 1061 (1985).

[98] Brand JCD, Chiu PH, Hoy AR, Bist HD. *Sulfur dioxide: Rotational constants and asymmetric structure of the $\tilde{C}^1B_2$ state*. J. Mol. Spectrosc. **60**, 43 (1976).

[99] Innes KK. *SO_2: Origins of unequal bond lengths in the $\tilde{C}^1B_2$ electronic state*, J. Mol. Spectrosc. **120**, 1 (1986).

[100] Bode BM, Gordon MS. *Macmolplt: A graphical user interface for GAMESS*, J. Mol. Graph. Modelling **16**, 133 (1998).

[101] Kamiya K, Matsui H. *Theoretical Studies on the Potential Energy Surfaces of SO_2: Electronic States for Photodissociation from the $\tilde{C}^1B_2$ State*, Bull. Chem. Soc. Jap. **64**, 2792 (1991).

[102] Francl MM, Pietro WJ, Hehre WJ, Binkley JS, Gordon MS, DeFrees DJ, et al. *Self-consistent molecular orbital methods. XXIII. A polarization-type basis set for second-row elements*, J. Chem. Phys. **77**, 3654 (1982).

[103] Dunning TH. *Gaussian basis sets for use in correlated molecular calculations. I. The atoms boron through neon and hydrogen*, J. Chem. Phys. **90**, 1007 (1989).

[104] Woon DE, Dunning TH. *Gaussian basis sets for use in correlated molecular calculations. III. The atoms aluminum through argon*, J. Chem. Phys. **98**, 1358 (1989).

[105] Jensen F, Helgaker T. *Polarization consistent basis sets. V. The elements Si-Cl*, J. Chem. Phys.

121, 3463 (2004).

[106] Jensen F. *Polarization consistent basis sets. II. Estimating the Kohn–Sham basis set limit*, J. Chem. Phys. **116**, 7372 (2002).

[107] Jensen F, Helgaker T. *Polarization consistent basis sets. V. The elements Si–Cl*, J. Chem. Phys. **121**, 3463 (2004).

[108] Belov SP, Tretyakov MY, Kozin IN, Klisch E, Winnewisser G, Lafferty WJ, et al. *High frequency transitions in the rotational spectrum of* SO_2, J. Mol. Spectrosc. **191**, 17 (1998).

[109] Flaud JM, Lafferty WJ. $^{32}S^{16}O_2$*: A Refined Analysis of the* $3\nu_3$ *Band and Determination of Equilibrium Rotational Constants*, J. Mol. Spectrosc. **161**, 396 (1993).

[110] Morino Y, Tanimoto M, Saito S. *Critical Survey of the Molecular Structure Determination by the Use of Spectroscopic Data for* SO_2, Acta Chem. Scand., Ser. A. **42**, 346 (1988).

[111] Kohl DA, Hilderbrandt RL. *A vibrational treatment of the effects of vibrational anharmonicity on gas-phase electron diffraction intensities: Part III. The shrinkage effect*, J. Mol. Struct., THEOCHEM **137**, 381 (1986).

[112] Mawhorter RJ, Fink M. *The vibrationally averaged, temperature-dependent structure of polyatomic molecules. II.* SO_2, J. Chem. Phys. **79**, 3292 (1983).

[113] Forney D, Kellogg CB, Thompson WE, Jacox ME. *The vibrational spectra of molecular ions isolated in solid neon. XVI.* SO_2^+*,*SO_2^-*, and* $(SO_2)_2^-$. J. Chem. Phys. **113**, 86 (2000).

[114] Li W-Z, Huang M-B, Chen B-Z. *The* 1^2A_1*,*1^2B_2*, and* 1^2A_2 *states of the* SO_2^+ *ion studied using multiconfiguration second-order perturbation theory*, J. Chem. Phys. **120**, 4677 (2004).

[115] Combes F, Gerin M, Wootten A, Wlodarczak G, Clausset F, Encrenaz PJ. *Acetone in interstellar space*. Astro. Astrophys. **180**, L13 (1987).

[116] Lewis ES, Lovas FJ, David MM, Nina Yanti M, Yi-Jehng K, Hollis JM, et al. *Confirmation of Interstellar Acetone*. Astrophys. J. **578**, 245 (2002).

[117] Haas Y. *Photochemical α-cleavage of ketones: revisiting acetone*, Photochem. Photobio. Sci. **3**, 6 (2004).

[118] Maeda S, Ohno K, Morokuma K. *A Theoretical Study on the Photodissociation of Acetone: Insight into the Slow Intersystem Crossing and Exploration of Nonadiabatic Pathways to the Ground State*, J. Phys. Chem. Lett. **1**, 1841 (2010).

[119] Szilágyi I, Kovács G, Farkas M, Zügner G, Gola A, Dóbé S, et al. *Photochemical and photophysical study on the kinetics of the atmospheric photodissociation of acetone*, React. Kinet. Catal. Lett. **96**, 437 (2009).

[120] Khamaganov VG, Karunanandan R, Horowitz A, Dillon TJ, Crowley JN. *Photolysis of CH3C(O)CH3 at 248 and 266 nm: pressure and temperature dependent overall quantum yields*, Phys. Chem. Chem. Phys. **11**, 6173 (2009).

[121] Rajakumar B, Gierczak T, Flad JE, Ravishankara AR, Burkholder JB. *The* CH_3CO *quantum yield in the 248 nm photolysis of acetone, methyl ethyl ketone and biacetyl*, J. Photochem. Photobio. A, Chem. **199**, 336 (2008).

[122] Mark Parnis J, King KA, Thompson MGK. *The chemistry of ionized Acetone/Ar mixtures under varying gas flow and mole ratio conditions: A matrix-isolation study*, J. Mass Spectrometry **44**, 652 (2009).

[123] Nobre M, Fernandes A, Ferreira da Silva F, Antunes R, Almeida D, Kokhan V, et al. *The VUV electronic spectroscopy of acetone studied by synchrotron radiation*, Phys. Chem. Chem. Phys. **10**, 550 (2008).

[124] Nádasdi R, Kovács G, Szilágyi I, Demeter A, Dóbé S, Bérces T, et al. *Exciplex laser photolysis study of acetone with relevance to tropospheric chemistry*, Chem. Phys. Lett. **440**, 31 (2007).

[125] Badr Y, Mahmoud MA. *On interaction of 193*

nm excimer laser with acetone (3s Rydberg state), J. Mol. Struct. **748**, 189 (2005).

[126] Chen W-K, Ho J-W, Cheng P-Y. *Ultrafast Photodissociation Dynamics of Acetone at 195 nm: I. Initial-state, Intermediate, and Product Temporal Evolutions by Femtosecond Mass-Selected Multiphoton Ionization Spectroscopy*, J. Phys. Chem. A. **109**, 6805 (2005).

[127] ter Steege DHA, Wirtz AC, Buma WJ. *Vibronic coupling in excited states of acetone*, J. Chem. Phys. **116**, 547 (2002).

[128] Hachey MJ, Grein F. *The Rydberg Spectrum Of Aldehydes And Ketones: A comparison using formaldehyde as a benchmark*, in Sándorfy C (ed). *The Role of Rydberg States in Spectroscopy and Photochemistry*, Springer, Netherlands (1999).

[129] Merchán M, Roos BO, McDiarmid R, Xing X. *A combined theoretical and experimental determination of the electronic spectrum of acetone*, J. Chem. Phys. **104**, 1791 (1996).

[130] Xing X, McDiarmid R, Philis JG, Goodman L. *Vibrational assignments in the 3p Rydberg states of acetone*, J. Chem. Phys. **99**, 7565 (1993).

[131] Kundu T, Thakur SN, Goodman L. *Methyl rotor effects on acetone Rydberg spectra. I. The 1A2(3p←n)←1A1 transition*, J. Chem. Phys. **97**, 5410 (1992).

[132] Wiedmann RT, Goodman L, White MG. *Two-color zero kinetic energy-pulsed field ionization spectroscopy of the acetone n-radical cation: The* a_2 *torsional vibration*, Chem. Phys. Lett. **293**, 391 (1998).

[133] Philis JG, Goodman L. *Methyl rotor effects on acetone Rydberg spectra. II. The* $^1B_2(3s \leftarrow n) \leftarrow {}^1A_1$ *transition*, J. Chem. Phys. **98**, 3795 (1993).

[134] Brint P, O'Toole L, Couris S, Jardine D. *Multiphoton ionisation spectroscopy of the 3s(2 + 2, 1) and 4s(3 + 1) Rydberg states of acetone: evidence for a molecular valence state at 153 nm*, J. Chem. Soc., Faraday Trans. **87**, 2891 (1991).

[135] Zhu YF, Allman SL, Phillips RC, Garrett WR, Chen CH. *Photophysics of the acetone 3p Rydberg states utilizing two-photon resonant ionization spectroscopy*, Chem. Phys. **202**, 175 (1996).

[136] Gaines GA, Donaldson DJ, Strickler SJ, Vaida V. *The (n0-3s) Rydberg state of acetone: absorption spectroscopy of jet-cooled acetone and acetone-d6*, J. Phys. Chem. **92**, 2762 (1988).

[137] Lawson M, Duncan ABF. *The Spectrum of Deuteroacetone in the Vacuum Ultraviolet A Comparison with the Spectrum of Acetone*, J. Chem. Phys. **12**, 329 (1944).

[138] Wiberg KB, de Oliveira AE, Trucks G. *A Comparison of the Electronic Transition Energies for Ethene, Isobutene, Formaldehyde, and Acetone Calculated Using RPA, TDDFT, and EOM-CCSD. Effect of Basis Sets*, J. Phys. Chem. A. **106**, 4192 (2002).

[139] Angeli C, Borini S, Ferrighi L, Cimiraglia R. *Ab inition-electron valence state perturbation theory study of the adiabatic transitions in carbonyl molecules: Formaldehyde, acetaldehyde, and acetone*, J. Chem. Phys. **122**, 114304 (2005).

[140] Cosofret BR, Dylewski SM, Houston PL. *Changes in the Vibrational Population of* $SO(^3\Sigma^-)$ *from the Photodissociation of* SO_2 *between 202 and 207 nm*, J. Phys. Chem. A. **104**, 10240 (2000).

[141] Pophristic V, Goodman L, Gorb L, Leszczynski J. *Acetone n-radical cation conformational preference and torsional barrier*, J. Chem. Phys. **116**, 7049 (2002).

[142] Baba M, Hanazaki I, Nagashima U. *The* $S_1(n,\pi^*)$ *states of acetaldehyde and acetone in supersonic nozzle beam: Methyl internal rotation and C=O out-of-plane wagging*, J. Chem. Phys. **82**, 3938 (1985).

[143] Just GMP, McCoy AB, Miller TA. *Effect of methyl rotation on the electronic spectrum of the methyl peroxy radical*, J. Chem. Phys. **127**, 044310 (2007).

[144] Perry DS. *Torsion-vibration coupling in methanol: Diabatic behavior in the CH overtone region*, J. Phys. Chem. A **112**, 215 (2008).

[145] Barbatti M, Paier J, Lischka H. *Photochemistry of ethylene: A multireference configuration interaction investigation of the excited-state energy surfaces*, J. Chem. Phys. **121**, 11614 (2004).

[146] Pophristic V, Goodman L, Gorb L, Leszczynski J. *Acetone n-radical cation conformational preference and torsional barrier*, J. Chem. Phys. **116**, 7049 (2002).

[147] Shea DA, Goodman L, White MG. *Acetone n-radical cation internal rotation spectrum: The torsional potential surface*, J. Chem. Phys. **112**, 2762 (2000).

[148] Ozkabak AG, Philis JG, Goodman L. *Methyl torsional interactions in acetone*, J. Am. Chem. Soc. **112**, 7854 (1990).

[149] Philis JG, Berman JM, Goodman L. *The acetone a2 torsional vibration*, Chem. Phys. Lett. **167**, 16 (1990).

[150] Shimanouchi T. *Tables of Molecular Vibrational Frequencies Consolidated. Volume I*, Nat. Stand. Ref. Data Ser., Nat. Bur. Stand **39** (1972).

[151] McDiarmid R. *On the absorption spectrum of the 3s Rydberg state of acetone*, J. Chem. Phys. **95**, 1530 (1991).

[152] Duncan ABF. *The Absorption Spectrum of Acetone Vapor in the Far Ultraviolet*, J. Chem. Phys. **3**, 131 (1935).

[153] Lake JS, Harrison AJ. *Absorption of Acyclic Oxygen Compounds in the Vacuum Ultraviolet. III. Acetone and Acetaldehyde*, J. Chem. Phys. **30**, 361 (1959).

[154] Zuckermann H, Haas Y, Drabbels M, Heinze J, Meerts WL, Reuss J, et al. *Acetone, a laser-induced fluorescence study with rotational resolution at 320 nm*, Chem. Phys. **163**, 193 (1992).

[155] Donaldson DJ, Gaines GA, Vaida V. *Cluster-induced potential shifts as a probe for dissociation dynamics in the (n0-3s) Rydberg state of acetone*, J. Phys. Chem. **92**, 2766 (1988).

[156] Cornish TJ, Baer T. *An experimental link between the carbon-13 NMR chemical shift of carbonyl carbons and the energy shifts observed in the n .fwdarw. 3s optical transition of cyclic ketones*. J. Am. Chem. Soc. **110**, 6287 (1988).

[157] Mejía-Ospino E, García G, Guerrero A, Álvarez I, Cisneros C. *High resolution multiphoton ionization and dissociation of acetone 3s←n Rydberg transitions*, Eur. Phys. J. D **30** 149 (2004).

[158] McDiarmid R, Sabljić A. *Experimental assignments of the 3p Rydberg states of acetone*, J. Chem. Phys. **89**, 6086 (1988).

[159] McDiarmid R, Xing X. *Nonadiabatic coupling of the 3p Rydberg and ππ* valence states of acetone*, J. Chem. Phys. **107**, 675 (1997).

[160] Thakur SN, Guo D, Kundu T, Goodman L. *Two-photon photoacoustic spectroscopy of acetone 3p Rydberg states*, Chem. Phys. Lett. **199**, 335 (1992).

[161] Zheng X, Wu H, Song Y, Wu J, Zhang J, Cui Z. *A multiphoton ionization study of acetone using time-of-flight mass spectrometry*, Chin. Sci. Bull. **55**, 3123 (2010).

[162] Gedanken A. *A magnetic circular dichroism study of the 3p Rydberg states of acetone*, J. Phys. Chem. **89**, 3781 (1985).

[163] Farmanara P, Stert V, Radloff W. *Ultrafast photodissociation dynamics of acetone excited by femtosecond 155 nm laser pulses*, Chem. Phys. Lett. **320**, 697 (2000).

[164] Chen W-K, Ho J-W, Cheng P-Y. *Ultrafast photodissociation dynamics of the acetone 3s Rydberg state at 195 nm: a new mechanism*, Chem. Phys. Lett. **380**, 411 (2003).

[165] Khamaganov V, Karunanandan R, Rodriguez A, Crowley JN. *Photolysis of $CH_3C(O)CH_3$ (248 nm,*

266 nm), $CH_3C(O)C_2H_5$ (248 nm) and $CH_3C(O)Br$ (248 nm): Pressure dependent quantum yields of CH_3 formation, Phys. Chem. Chem. Phys. **9**, 4098 (2007).

[166] Somnitz H, Ufer T, Zellner R. *Acetone photolysis at 248 nm revisited: Pressure dependence of the CO and CO_2 quantum yields*, Phys. Chem. Chem. Phys. **11**, 8522 (2009).

[167] Emrich M, Warneck P. *Photodissociation of Acetone in Air: Dependence on Pressure and Wavelength. Behavior of the Excited Singlet State*, J. Phys. Chem. A. **104**, 9436 (2000).

[168] Blitz MA, Heard DE, Pilling MJ. *Study of Acetone Photodissociation over the Wavelength Range 248−330 nm: Evidence of a Mechanism Involving Both the Singlet and Triplet Excited States*, J. Phys. Chem. A. **110**, 6742 (2006).

[169] Gierczak T, Burkholder JB, Bauerle S, Ravishankara AR. *Photochemistry of acetone under tropospheric conditions*, Chem. Phys. **231**, 229 (1998).

[170] Trott WM, Blais NC, Walters EA. *Molecular beam photoionization study of acetone and acetone-d6*, J. Chem. Phys. **69**, 3150 (1978).

[171] Furuya K, Katsumata S, Kimura K. *Photoelectron spectra of acetone and acetone dimer*, J. Elec. Spectrosc. Rel. Phenom. **62**, 237 (1993).

[172] Huebner RH, Celotta RJ, Mielczarek SR, Kuyatt CE. *Electron energy loss spectroscopy of acetone vapor*, J. Chem. Phys. **59**, 5434 (1973).

[173] St. John WM, Estler RC, Doering JP. *Low-energy electron impact study of acetone*, J. Chem. Phys. **61**, 763 (1974).

[174] Lepage M, Michaud M, Sanche L. *Low-energy electron-energy-loss spectroscopy of condensed acetone: Electronic transitions and resonance-enhanced vibrational excitations*, J. Chem. Phys. **112**, 6707 (2000).

[175] Hess B, Bruna PJ, Buenker RJ, Peyerimhoff SD. *Ab initio CI study of the electronic spectrum of acetone*, Chem. Phys. **18**, 267 (1976).

[176] Klessinger M, Pötter T, Wüllen C. *Semiempirical valence-electron calculations of excited state geometries and vibrational frequencies*, Theo. Chim. Acta. **80**, 1 (1991).

[177] Gwaltney SR, Bartlett RJ. *An application of the equation-of-motion coupled cluster method to the excited states of formaldehyde, acetaldehyde, and acetone*, Chem. Phys. Lett. **241**, 26 (1995).

[178] Wiberg KB, Stratmann RE, Frisch MJ. *A time-dependent density functional theory study of the electronically excited states of formaldehyde, acetaldehyde and acetone*, Chem. Phys. Lett. **297**, 60 (1998).

[179] Liao DW, Mebel AM, Hayashi M, Shiu YJ, Chen YT, Lin SH. *Ab initio study of the n-π^* electronic transition in acetone: Symmetry-forbidden vibronic spectra*, J. Chem. Phys. **111**, 205 (1999).

[180] Shiu YJ, Hayashi M, Mebel AM, Chen Y-T, Lin SH. *Computational formulas for symmetry-forbidden vibronic spectra and their application to n–π^* transition in neat acetone*, J. Chem. Phys. **115**, 4080 (2001).

[181] Martínez-Núñez E, Fernández-Ramos A, Cordeiro MNDS, Vázquez SA, Aoiz FJ, Bañares L. *A direct classical trajectory study of the acetone photodissociation on the triplet surface*, J. Chem. Phys. **119**, 10618 (2003).

[182] Aquilante F, Cossi M, Crescenzi O, Scalmani G, Barone V. *Computation of the acetone ultraviolet spectrum in gas phase and in aqueous solution by a mixed discrete/continuum model*, Mol. Phys. **101**, 1945 (2003).

[183] Antol I, Eckert-Maksić M, Ončák M, Slavíček P, Lischka H. *Photodissociation Pathways of Acetone Upon Excitation Into the 3s Rydberg State: Adiabatic Versus Diabatic Mechanism*, Collect. Czech Chem. Comm. **73**, 1475 (2008).

[184] Gilbert ATB, Besley NA, Gill PMW. *Self-Consistent Field Calculations of Excited States*

Using the Maximum Overlap Method (MOM), J. Phys. Chem. A **112**, 13164 (2008).

[185] Lavín C, Velasco AM. *Theoretical study on intensities in the discrete and continuum electronic spectrum of acetone*, J. Quant. Spectrosc. Rad. Transfer **127**, 96 (2013).

[186] Donaldson DJ, Gaines GA, Vaida V. *Cluster-induced potential shifts as a probe for dissociation dynamics in the n0-3s Rydberg state of acetone*, J. Phys. Chem. **92**, 2766 (1988).

[187] Herzberg G. *Molecular spectra and molecular structure*. II, van Nostrand, New York (1945).

[188] Ridley T, Lawley KP, Donovan RJ. *A study of the Rydberg states of furan (C_4H_4O) and deuterated furan (C_4D_4O) using mass-resolved (2+1) and (3+1) resonance enhanced multiphoton ionization*, Phys. Chem. Chem. Phys. **6**, 5304 (2004).

[189] Wang S, Shi Y, Dénommée S, Simard B, Lee Y-P. *Investigation of some Rydberg states of ketene by two-photon resonance-enhanced multiphoton ionization spectroscopy*, J. Chem. Phys. **119**, 7772 (2003).

[190] Cheng B-M, Bahou M, Chen W-C, Yui C-h, Lee Y-P, Lee LC. *Experimental and theoretical studies on vacuum ultraviolet absorption cross sections and photodissociation of CH_3OH,CH_3OD,CD_3OH, and CD_3OD*, J. Chem. Phys. **117**, 1633 (2002).

[191] Philis JG. *Resonance-enhanced multiphoton ionization spectra of jet-cooled methanol and ethanol*, Chem. Phys. Lett. **449**, 291 (2007).

[192] Philis JG. *Torsional features in the (3s)$S_1 \leftarrow S_0$ transition of N-methylpyrrole and $C_4D_4NCH_3$*, J. Mol. Struct. **651–653**, 567 (2003).

[193] Romanzin C, Gans B, Douin S, Boyé-Péronne S, Gauyacq D. *193nm photolysis of $CHCl_3$: Probe of the CH product by CRDS*, Chem. Phys. **351**, 77 (2008).

[194] Zobel CR, Duncan ABF. *Vacuum Ultraviolet Absorption Spectra of Some Halogen Derivatives of Methane. Correlation of the Spectra*, J. Am. Chem. Soc. **77**, 2611 (1955).

[195] Russell BR, Edwards LO, Raymonda JW. *Vacuum ultraviolet absorption spectra of the chloromethanes*, J. Am. Chem. Soc. **95**, 2129 (1973).

[196] Lee LC, Suto M. *Fluorescence yields from photodissociative excitation of chloromethanes by vacuum ultraviolet radiation*, Chem. Phys. **114**, 423 (1987).

[197] P. Seccombe D, P. Tuckett R, Baumgartel H, W. Jochims H. *Vacuum-UV fluorescence spectroscopy of CCl_3F, CCl_3H and CCl_3Br in the range 8-30 eV*, Phys. Chem. Chem. Phys. **1**, 773 (1999).

[198] Taketani F, Takahashi K, Matsumi Y. *Quantum Yields for Cl(^2P_j) Atom Formation from the Photolysis of Chlorofluorocarbons and Chlorinated Hydrocarbons at 193.3 nm*, J. Phys. Chem. A. **109**, 2855 (2005).

[199] Lago AF, Baer T. *Dissociation dynamics and thermochemistry of chloroform and tetrachloroethane molecules studied by threshold photoelectron photoion coincidence*, Inter. J. Mass Spectrometry **252**, 20 (2006).

[200] Harvey J, Tuckett RP, Bodi A. *A Halomethane Thermochemical Network from iPEPICO Experiments and Quantum Chemical Calculations*, J. Phys. Chem. A. **116**, 9696 (2012).

[201] Chen L-L, Xu Y-F, Feng Q, Tian SX, Liu F-Y, Shan X-B, et al. *Vacuum Ultraviolet Negative Photoion Spectroscopy of Chloroform*, J. Phys. Chem. A. 115, 4248 (2011).

[202] Iwakura I, Yabushita A, Kobayashi T. *Transition States and Nonlinear Excitations in Chloroform Observed with a Sub-5 fs Pulse Laser*, J. Am. Chem. Soc. **131**, 688 (2008).

[203] Ying JF, Leung KT. *Electron-impact excitation of low-lying preionization-edge electronic and Rydberg transitions of fluoroform and*

chloroform: Bethe surfaces and absolute generalized oscillator strengths, Phys. Rev A **53**, 1476 (1996).

[204] Dixon RN, Murrell JN, Narayan B. *The photoelectron spectra of the halomethanes*, Mol. Phys. **20**, 611 (1971).

[205] Demaison J. *Equilibrium structure of chloroform*, J. Mol. Spectrosc. **251**, 217 (2008).

[206] von Niessen W, Åsbrink L, Bieri G. *30.4 nm He (II) photoelectron spectra of organic molecules Part VI. Halogeno-compounds (C, H, X; X = Cl, Br, I)*, J. Elec. Spectrosc. Rel. Phenom. **26**, 173 (1982).

[207] Jalili S, Akhavan M. *The study of isotope effects of chloroform and chloromethane using vibrational frequencies*, J. Mol. Struct., THEOCHEM **765**, 105 (2006).

[208] Frisch MJ, Pople JA, Binkley JS. *Self-consistent molecular orbital methods 25. Supplementary functions for Gaussian basis sets*, J. Chem. Phys. **80**, 3265 (1984).

[209] Shimanouchi T. *Tables of Molecular Vibrational Frequencies Consolidated. Volume I*, Nat. Stand. Ref. data Sys. **168**, 123 (1972).

[210] Theodosiou CE, Inokuti M, Manson ST. *Quantum defect values for positive atomic ions*, At. Data Nucl. Data Tables **35**, 473 (1986).

[211] Vegard L. *Luminescence of Solid Nitrogen and the Auroral Spectrum*, Nature **114**, 715 (1924).

[212] Kreutz J, Medvedev SA, Jodl HJ. *Low-temperature phases of solid oxygen at pressures up to 8GPa determined by Raman and infrared spectroscopy*, Phys. Rev. B **72**, 214115 (2005).

[213] Katz B, Brith M, Sharf B, Jortner J. *Experimental Study of the Higher π→ π* Transitions of Benzene in Low-Temperature Matrices*, J. Chem. Phys. **52**, 88 (1970).

[214] Metropolis N. *Vibrational Analysis of the Absorption System of Sulphur Dioxide at λ 3400−2600 Å*, Phys. Rev. **60**, 295 (1941).

[215] Phillips LF, Smith JJ, Meyer B. *The ultraviolet spectra of matrix isolated disulfur monoxide and sulfur dioxide*, J. Mol. Spectrosc. **29**, 230 (1969).

[216] Brand JCD, Nanes R. *The 3000–3400 Å absorption of sulfur dioxide*, J. Mol. Spectrosc. **46**, 194 (1973).

[217] Roncin JY, Damany N, Vodar B. *Electronic transitions of CS_2 and OCS trapped in solid matrices and Rydberg series in dense media*, Chem. Phys. Lett. **3**, 197 (1969).

[218] Dressler K. *Ultraviolet Absorption Spectrum of Ammonia in Solid Argon at 4.2°K*, J. Chem. Phys. **35**, 165 (1961).

[219] Pysh ES, Rice SA, Jortner J. *Molecular Rydberg Transitions in Rare-Gas Matrices—Evidence for Interaction Between Impurity States and Crystal States*, J. Chem. Phys. **43**, 2997 (1965).

[220] Katz B, Brith M, Sharf B, Jortner J. *Rydberg States of Benzene in Rare-Gas Matrices*, J. Chem. Phys. **50**, 5195 (1969).

[221] Singh PJ, Shastri A, Raja Sekhar BN, D'Souza R, Jagatap BN. *Effect of isotopic substitution in the electronic absorption spectrum of acetone: VUV photoabsorption studies of acetone-d6*, J. Quant Spectrosc. Rad. Transfer **114**, 20 (2013).